

Southern Methodist University

SMU Scholar

Mechanical Engineering Research Theses and
Dissertations

Mechanical Engineering

Summer 2019

Impedance-Based Microfluidic Platform for Quantitative Biology

Amin Mansoorifar

Southern Methodist University, amansoorifar@smu.edu

Follow this and additional works at: https://scholar.smu.edu/engineering_mechanical_etds



Part of the [Bioelectrical and Neuroengineering Commons](#), and the [Biomedical Devices and Instrumentation Commons](#)

Recommended Citation

Mansoorifar, Amin, "Impedance-Based Microfluidic Platform for Quantitative Biology" (2019). *Mechanical Engineering Research Theses and Dissertations*. 19.

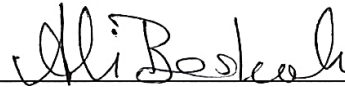
https://scholar.smu.edu/engineering_mechanical_etds/19

This Dissertation is brought to you for free and open access by the Mechanical Engineering at SMU Scholar. It has been accepted for inclusion in Mechanical Engineering Research Theses and Dissertations by an authorized administrator of SMU Scholar. For more information, please visit <http://digitalrepository.smu.edu>.

IMPEDANCE-BASED MICROFLUIDIC PLATFORM

FOR QUANTITATIVE BIOLOGY

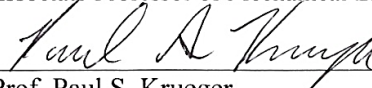
Approved by:



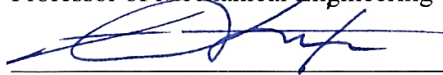
Prof. Ali Beskok
Professor of Mechanical Engineering



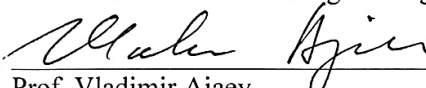
Prof. David Willis
Associate Professor of Mechanical Engineering



Prof. Paul S. Krueger
Professor of Mechanical Engineering



Prof. MinJun Kim
Professor of Mechanical Engineering



Prof. Vladimir Ajaev
Professor of Mathematics

IMPEDANCE-BASED MICROFLUIDIC PLATFORM
FOR QUANTITATIVE BIOLOGY

A Dissertation Presented to the Graduate Faculty of
Lyle School of Engineering
Southern Methodist University

in

Partial Fulfillment of the Requirements

for the degree of

Doctor of Philosophy

with a

Major in Mechanical Engineering

by

Amin Mansoorifar

(B.Sc., Mechanical Engineering, Shiraz University, Iran, 2012)
(M.Sc., Mechanical Engineering, Shiraz University, Iran, 2014)

August 6, 2019

Copyright (2019)

Amin Mansoorifar

All Rights Reserved

ACKNOWLEDGMENTS

I would like to express my utmost gratitude and give sincere thanks to my dissertation advisor Prof. Ali Beskok, for his continuous support in guiding me through my research as well as his mentoring, encouragements and his friendship during the past 5 years. I also would like to thank my advisory committee members, Professors David Willis, Paul S. Krueger, MinJun Kim, and Vladimir Ajaev for their contributions in this dissertation. I am also grateful for many invaluable help and support of my beloved friends namely Anil Koklu, Alper Tunga Celebi, Chinh Nguyen, Yigit Akkus, Ali Vafamehr, Martha Penturf, Vahid Sadri, Zara Tayebi, Arefeh Safaie Moghadam, Soheil Sohrabi, Nahid Mirzaie, Rita Enami, Marjan Miri, Hedieh Ashrafi, Hamed Nikfarjam, Mahdi Heidarizad, Nadere Mansouri, Lael Badakhshanian, Mohammad Mahdavi, Arian Emaminejad, and Javad Jomepoor. Finally, A special thanks to my family that without their love and support this dissertation would not exist.

Mansoorifar, Amin

B.Sc., Shiraz University, Iran, 2012

M.Sc., Shiraz University, Iran, 2014

Impedance-Based Microfluidic Platform for Quantitative Biology

Advisor: Professor Ali Beskok

Doctor of Philosophy conferred August 6, 2019

Dissertation completed June 5, 2019

Dielectric properties of biological cells are functions of cellular structure, content, state, and phenotype. Dielectric spectroscopy (DS) is a nondestructive method to characterize dielectric properties by measuring impedance data over a frequency range. This method has been widely used for various applications such as counting, sizing, and monitoring biological cells and particles. Recently, this method has been suggested to be utilized in various stages of the drug discovery process due to its low sample consumption and fast analysis time.

In this thesis, we have developed a lab-on-a-chip device that uses an electro-activated microwells array for capturing, making DS measurements on, and unloading of biological cells. To the best of our knowledge, this is the first microfluidic chip that combines electro-activated microwells and DS to analyze biological cells. We demonstrated that our device enabled real-time measurements of dielectric properties of live cancer cells and allowed the assessment of the cellular response to variations in buffer conductivity and pH. Moreover, we proved that this device is capable of quantitatively measuring drug effects on biological cells, and the results show that the proposed microfluidic system has the potential to be used in early stages of the drug discovery process.

TABLE OF CONTENTS

ACKNOWLEDGMENTS	iv
Chapter 1: INTRODUCTION.....	1
Chapter 2: THEORY.....	7
2.1. Dipoles	7
2.2. Dielectrics	8
2.2.1. Dielectric Relaxations.....	11
2.3. Interfacial Polarization.....	13
2.3.1. The effective dipole moment of a spherical particle.....	15
2.3.2. The effective dipole moment of an ellipsoidal particle	17
2.4. Complex permittivity of suspensions.....	19
2.4.1. Complex permittivity of the diluted suspension	19
2.4.2. Complex permittivity of concentrated suspension.....	20
2.4.3. Shell models.....	21
2.5. Electrical forces on particles	24
2.5.1. Electrophoresis.....	24
2.5.2. Dielectrophoresis (DEP).....	25
Chapter 3: DIELECTROPHORETIC ASSISTED LOADING AND UNLOADING OF MICRO-WELLS FOR IMPEDANCE SPECTROSCOPY	28
3.1. Materials and Methods.....	28
3.1.1 Photolithography.....	29

3.1.2. Device assembly	31
3.1.3. Experimental setup.....	33
3.1.4. Numerical modeling.....	34
3.1.5. DEP Theory and Dielectric Spectroscopy	36
3.2 Results and Discussion	37
3.3. Conclusion	47
3.4. Appendix.....	48
3.4.1. Procedure for extracting electrode polarization effect in parallel plate electrodes:	48
3.4.2. Procedure for extracting sub-cellular properties using Maxwell- Wagner and single shell model.....	49
3.4.3. Grid Refinement Study	50
Chapter 4: ON-CHIP ELECTRICAL IMPEDANCE MEASUREMENTS OF BIOLOGICAL CELLS IN RESPONSE TO EXTERNAL STIMULI.....	53
4.1. Materials and Methods.....	54
4.1.1. Chip Fabrication.....	54
4.1.2. Experimental setup.....	55
4.1.3. Cell Preparation and Viability Test.....	56
4.1.4. Equivalent Circuit Modeling.....	58
4.2. Results and Discussion	61
4.2.1. DEP Response Prediction.....	61
4.2.2. DS Measurements	63
4.2.3. PC-3 Cells Response to LCB Suspension	66
4.2.4. PC-3 Cells Response to pH change.....	67

4.2.5. Viability Tests	69
4.3. Conclusion	71
Chapter 5: QUANTIFICATION OF CELL DEATH USING AN IMPEDANCE BASED MICROFLUIDIC PLATFORM	72
5.1. Materials and Methods.....	73
5.1.1. Device Fabrication	73
5.1.3. Cell Preparation	74
5.1.4. Principal Component Analysis	76
5.2. Results and Discussion	77
5.2.1. Viability Test	78
5.2.2. DS Measurements	78
5.2.3. Equivalent Circuit Analysis	81
5.2.4. Single Frequency Measurements	83
5.2.5. Principal Component Analysis	84
5.2.6. Opacity Ratio Measurement	89
5.3. Available Technologies	91
5.4. Conclusion	99
Chapter 6: SUMMARY AND FUTURE RESEARCH	105
6.1 Summary of the current work	105
6.2 Future Research	106

LIST OF FIGURES

Figure 2.1 A parallel plate electrode with a layer of dielectric material.....	10
Figure 2.2 A parallel plate electrode with two layers of dielectric material.....	14
Figure 2.3 Variation of real (solid line) and imaginary parts (dotted line) of K with frequency. Figure adapted from [71]	17
Figure 2.4 Schematic for the Single-Shell and Double shell models.	23
Figure 2.5 Electrical forces on a dipole moment in a non-uniform electric field.....	26
Figure 3.1 Microfabrication process of a DEP chip using two-step photolithography process. a) Electrode fabrication, b) micro-wells and micro-channel fabrication, and c) electrode alignment and device assembly.....	31
Figure 3.2 a) Assembled microfluidic chip, b) a microscopy picture of the gold electrode and micro-wells, c) SEM image of one micro-well, d) the working principle of the microfluidic device, and e) The computational domain consisting of a medium solution, SU-8, and spherical yeast cells. The yeast cells are modeled consisting of an inner cytoplasm covered by a membrane modeled as an interface.....	33
Figure 3.3 Simulated electric field distribution in a cross-sectional plane located in the middle of a micro-well.....	38
Figure 3.4 a) The real part of Clausius-Mossotti factor ($\text{Re}(K)$) for yeast cells suspended at 0.05 S/m LCB solution as a function of frequency for 0-10, 10-20, and 20-30 minutes time periods after being placed in the LCB solution from growth media. The procedure for extracting Clausius-Mossotti factor is the same as in [77]. The response of yeast cells to $2V_{pp}$ AC electric field at b) $f = 5$ MHz, and c) $f = 10$ kHz, d) clean array after the yeast cells are washed away.....	40
Figure 3.5 Comparison between impedance data for yeast cells captured inside micro-wells and not captured.....	41
Figure 3.6 Impedance magnitude value spectrum for applying pDEP for 5 seconds at different initial yeast concentration in 0.05 S/m LCB solution.....	42
Figure 3.7 a) Experimentally measured impedance spectrum of microchip device for pure LCB and yeast suspended in 0.05 S/m LCB. Lines show the results for pure LCB while	

symbols show yeast suspended LCB. b) Experimentally measured impedance value and c) phase angle for yeast cells suspended in 0.01, 0.05, and 0.2 S/m LCB.....44

Figure 3.8 Comparison between numerical and experimental Impedance data (magnitude and phase angle) for a) pure LCB solution (0.05 S/m), and b) yeast cells suspended in LCB. Solid and dashed lines represent experimental impedance magnitude and phase angle results, while circles and triangles show numerical impedance magnitude and phase angle values.46

Figure 3.A1 Variation of impedance value with the number of computational elements .51

Figure 3.A2 The normalized standard deviation (standard deviation divided by mean) of a) impedance magnitude, and b) phase angle for yeast cells suspended in 0.01, 0.05, and 0.20 S/m LCB solution.52

Figure 4.1 a) Top view of the microfluidic device layers and side view of the assembled device; b) Schematics of the experimental setup.....55

Figure 4.2 Proposed equivalent circuit model for a) filled and b) empty micro-wells. c) The equivalent circuit model for the microfluidic device.....59

Figure 4.3 a) The real part of CM factor for PC-3 cells suspended in LCB at various times b) captured PC-3 cells after 20s of pDEP application at 2 Vpp and 5 MHz frequency. The inset shows a sample of individual empty and filled micro-wells.....63

Figure 4.4 Experimental and fitted a) impedance value and b) phase angle of the PC-3 cell suspension in LCB with pH=7.3 in the 10 kHz - 40 MHz frequency range obtained five minutes after the suspension of PC3 cells within LCB.....65

Figure 4.5 Impedance sensitivity to the equivalent circuit model elements66

Figure 4.6 Time-dependent variations in the membrane capacitance and cytoplasmic resistance after suspension of PC-3 cells in LCB.67

Figure 4.7 Extracted cell membrane and cytoplasmic resistance with changing external pH values. The white region shows pH=7.3 and gray regions indicate pH=5.8.69

Figure 4.8 Viable and dead PC-3 cells in LCB with a) pH=7.3 and b) pH=5.8 after 1 hour. Percentile viability of PC-3 cells in LCB with c) pH=7.3 and d) pH=5.8.....70

Figure 5.1 a) Side view of the microfluidic device, b) experimental setup, c) SEM image of the micro-wells array, and d) SEM image of an individual micro-well.	74
Figure 5.2 Snapshots of PC-3 cell culture after a) 24 hours, b) 48 hours, and c) 72 hours.	75
Figure 5.3 Microscopy images of a) empty and b) filled micro-wells.....	75
Figure 5.4 Re(K) of PC-3 cells suspended in LCB.....	77
Figure 5.5 Percentile viability of PC-3 cells exposed to 100 μ M Enzalutamide.....	78
Figure 5.6 Normalized standard deviation of impedance value and phase angle of healthy cells.	79
Figure 5.7 a) Impedance spectra and b) phase angle of PC-3 cells treated with 100 μ M Enzalutamide for two hours before and after EP extraction. c) Impedance spectra and d) phase angle spectra of PC-3 cells treated with 100 μ M Enzalutamide at 0, 2, and 8 hours.	81
Figure 5.8 Extracted a) membrane capacitance and b) cytoplasmic resistance of PC-3 cells over 8 hours.....	83
Figure 5.8 Changes over time in a) Impedance value and b) phase angle of PC-3 cells treated with 100 μ M Enzalutamide.....	84
Figure 5.9 a) Scree plot of first 20 components, and b) first two principal component coefficients.....	85
Figure 5.10 a) First principal component and b) second principal component coefficient of raw impedance data, after EP elimination, and after EP & stray capacitance elimination.	86
Figure 5.11 a) Score plot of the first two principal components and b) PC score variations with respect to time.	87
Figure 5.12 a) PC1 and b) PC2 score changes as a function of time for different starting frequencies.	88
Figure 5.13 a) Phase angle spectra score plot of the first two principal components and b) PC score variations with respect to time.	89

Figure 5.13 Normalized OR of PC-3 cells treated with 100 μ M Enzalutamide. Initial OR was 0.812.	90
Figure 5.14 A view of the experimental setup, the array holder, and 8W10E+ electrodes with 40 active electrode sites in each well.....	92
Figure 5.15 Impedance change of MCF-7 cell layer at different drug concentrations and frequencies	95
Figure 5.16 Impedance change of DU-145 cell layer at different drug concentrations and frequencies	96
Figure 5.17 Final impedance change values for MCF-7 and DU-145 at different drug concentrations and frequencies.....	98
Figure 6.1 a) Microscopy and b) SEM images of the coated electrodes. c) Impedance spectrum of PBS (1.5 S/m) measured with planar and coated electrodes.	107
Figure 6.2 Side view of a) bottom and b) top substrate. c) Electrode configuration and d) alignment of top and bottom substrates.	108

Chapter 1

INTRODUCTION

Dielectric spectroscopy (DS) is a non-invasive, label-free, and fast technique for measuring type, size, and dielectric properties of biological cells in real time [1-6]. This technique involves the application of a small AC test voltage and measurement of AC current in a wide range of frequencies and provides an impedance spectrum [7, 8]. It has been shown that membrane capacitance and cytoplasm conductivity becomes dominant on impedance at frequencies around 1 MHz and 10 MHz, respectively [9]. The dielectric properties of cells are significant indicators of health, function, and life stage of the cells [10-13]. Dielectric spectroscopy can be used to examine and discriminate between tumor cells and healthy cells. Using impedance measurement techniques, drug-resistant breast cancer cells (doxorubicin resistant MCF-7 DOX) may be distinguished from their parental cells (MCF-7 WT, wild-type) [14]. Simultaneous measurements of impedance with DS and fluorescence may sort between T-lymphocytes, monocytes, and neutrophils [15]. Since DS is non-invasive, label-free and amenable to real-time monitoring [16, 17], quantitative assessments of the growth rate, state of bio-reactions, and early indications of catastrophic events such as contamination or cessation of growth, may be obtained [18]. DS can investigate the real-time effects of external stimuli and drug uptake on membrane and cytoplasm without the need for complicated and expensive biochemical and microscopy techniques [19].

To have a reliable set of cell dielectric parameters from an impedance measurement of cell suspension, the volume fraction of cells should be around 10%. Considering this volume

fraction range, the number of 5 μm radius cells in 1 ml of cell suspension should be around 200 million. Culturing these many cells is impractical, especially for primary cells. Therefore, there is a need for miniaturizing dielectric spectroscopy device dimensions to reduce the required number of cells [20]. Microfluidic platforms operating with nano and microliters of samples are ideal candidates for miniaturized dielectric spectroscopy [21, 22]. Miniaturizing the chamber allows readings to be taken with tiny sample sizes. Early studies investigating the dielectric nature of cells did not consider the heterogeneous nature of the cell population and no efforts were made to control the size of the dielectric chamber [23-25]. Recently, advances in micro-technology have led to microfluidics and Lab-on-a-Chip (LOC) systems that can manipulate minimal fluid volumes. As an example, Grenier *et al.* [26] proposed a microfluidic coplanar-waveguide (CPW) sensor that accommodates microliters of samples. The ability to manipulate small volumes of fluid has not only reduced the volume of the measurement chamber but has also made possible biochemical and electrophysiological processes such as single cell manipulation [27], and dynamic control of the extracellular environment [28].

To collect cells and particles in a confined geometry, several cell-handling methods, including optical tweezers [29-32], chemical patterning [33, 34], nano-electrode array [35-37], micro-well arrays [38-44], and combinations of the methods above [45], have been developed. In particular, micro-well arrays enable large scale arraying and high throughput measurements [46, 47]. Lee and colleagues developed a miniaturized cell-culture array for toxicity screening of drug candidates and their cytochrome P450-generated metabolites, and they showed that 2,000-fold miniaturization does not change the cytotoxicity response compared with a conventional 96-well microtiter plate [48]. In another study, Wada and

colleagues used a microfluidic cell culture system in combination with sensor cells to quantitatively detect cytotoxic reagents [49]. Moreover, personalized treatment can be performed using micro-well arrays [50, 51]. For example, Xu et al. developed an effective drug sensitivity platform, where they successfully assayed the sensitivities of different single and combined-drug chemotherapy schemes for eight patients [52].

Many researchers used gravity to load cells inside the micro-wells [53, 54]. As an illustration, Yuan *et al.* collected a mixture of human glioma and murine fibroblast cells in 150,000 cylindrical micro-wells and reported that more than 50% of the micro-wells were filled with the cells [55]. The main problem in gravity-based micro-well array loading is its low efficiency of cell trapping and long trapping time. To overcome this problem, additional cell capture mechanisms are required.

A large number of methods have been developed to capture cells more effectively, including magnetic [56], optical, hydrodynamic [57], acoustic [58], and electrical forces [59]. Using electrical forces to capture cells have been utilized frequently due to its simplicity, high selectivity, contact-free approach, and its potential to be integrated into microfluidic systems. Combination of micro-well arrays with dielectrophoretic forcing, which is the motion of polarizable particles in a non-uniform electric field, enabled researchers to capture biological cells in confined well geometries more effectively in shorter periods. Electro-activated micro-wells have been used for several applications such as cell sorting and cell manipulation. Kim *et al.* proposed a microfluidic device made up of electro-active micro-wells to capture cells using positive Dielectrophoresis (DEP) and then lyse them using electroporation [60]. In another study, Cordovez *et al.* showed that electro-active micro-wells could serve to capture, store, and even repel different diameter

(6 to 20 μm) polystyrene particles [61]. Yoshimura *et al.* reported a microfluidic device consisting of 10,000 micro-wells to produce “cell couplets” [62].

After capturing, cells could be analyzed to determine their properties. Morimoto *et al.* used immunofluorescent labeling on cells and isolated them in micro-wells, where molecular analyses of cells were performed [63]. Kobayashi *et al.* used three different kinds of biochemical assays (immunostaining, viability/apoptosis, and fluorescence in situ hybridization (FISH)) for cancer cell discrimination after capturing cells by electro-activated micro-wells [64]. Most of the published articles relied on injection of expensive biochemical reagents, microscopy, and molecular analysis methods to find out cell types and their properties. As a non-invasive, inexpensive, and label-free technique, DS could be used to analyze the cells after capturing them in the micro-wells.

DEP trapping mostly requires biological cells to be suspended in a low conductivity medium [65]. Lower extracellular ionic concentration causes stronger polarization at the cell interior than the extracellular medium, which results in the collection of cells at high electric field regions. However, low conductivity buffers (LCB) induce changes in biological cells. Cells mainly respond to LCB by pumping out ions, followed by shape regulation [66, 67]. This results in a time-dependent dielectric property response [68]. Therefore, there is a critical need to consider the time-dependent dielectric response of cells in LCB. Moreover, extracellular pH plays an essential role in cell functions. The rate of cellular growth and metabolism of protein synthesis are strong functions of medium pH [69]. Direct measurements of cell response also have the advantages of continuous recording of metabolic changes in drug discovery processes [70].

In this dissertation, the efficiency of a new microfluidic device for capturing and then measuring the dielectric response of biological cells is demonstrated. We first tested our microfluidic device with yeast cells. The yeast cells are introduced with a low volume fraction (1%), and cell enrichment and unloading inside the micro-wells are established using positive DEP (pDEP) and negative DEP (nDEP), respectively, facilitating high throughput cell processing. Captured cells are analyzed using the DS method, which enables real-time measurements of sub-cellular dielectric properties of the biological cells. Furthermore, we focused on real-time measurements of PC-3, a highly metastatic prostate cancer cell line, and its response to changes in the external conductivity and pH. Since limited information about the bioelectric characteristics of PC-3 cells was available, we first determined the impedance of the PC-3 cell suspension using a parallel-plate electrode configuration and found the optimum frequencies for DEP assisted cell loading and unloading. Dimensions of PC-3 cells are suitable for single cell capture in the micro-wells allowing simultaneous DS measurement for up to 400-500 cells. An equivalent circuit model was developed for the current bio-chip geometry to extract cell membrane capacitance and cytoplasmic resistance. After diluting the cell suspension with LCB and capturing the cells inside micro-wells, the impedance spectrum was recorded for two hours with six seconds increments, which enabled a time-dependent evaluation of the PC-3 cell membrane capacitance and its cytoplasmic resistance change in LCB. This is followed by studies on cell response to external pH alterations between pH of 7.3 and 5.8. Moreover, we tested the effects of the Enzalutamide anti-cancer drug on PC-3 cells using different quantification methods. Enzalutamide at a concentration of 100 μ M was introduced to the cell medium, and impedance spectra were recorded for 8 hours till all the cells were dead

as determined by viability tests. Using the equivalent circuit model, cell data was extracted. Moreover, the impedance magnitude and phase angle at single frequencies were measured. The principal component analysis (PCA) was used to quantify the changes in PC3 cells. Additionally, opacity ratio was calculated as another method to quantify cells changes. Finally, an available technology for cells drug response was tested. The results obtained in this dissertation suggest that this impedance-based microfluidic device can be used to monitor cell state quantitatively and has potential applications in the early stages of the drug discovery process.

Chapter 2

THEORY

In this section, the basic theory behind dielectrics, polarization, and electrical forces, especially dielectrophoresis, is explained.

2.1. Dipoles

The electrical dipole consists of two charges with the same magnitude (Q), but opposite sign located at a distance d from each other. The dipole moment is the vector \mathbf{p} directed from the negative to positive charge and is defined as $\mathbf{p} = Q\mathbf{d}$ which has a unit of Cm, where \mathbf{d} is the vector connecting negative to the positive charge. The potential and electric field of a dipole at large distances ($r \gg d$) is given as

$$\varphi = \frac{|\mathbf{p}| \cos \theta}{4\pi\epsilon_0 r^2}; \quad \mathbf{E} = \frac{|\mathbf{p}|}{4\pi\epsilon_0 r^3} (2 \cos \theta \hat{r} + \sin \theta \hat{\theta}) \quad (2.1)$$

The potential energy of a dipole in electric field \mathbf{E} is defined as

$$U = -\mathbf{E} \cdot \mathbf{p} = -|\mathbf{E}|Qd \cos \theta \quad (2.2)$$

Based on Equation 2.2, when the electric field is perpendicular to the dipole moment, the energy is zero, and it reaches the minimum ($-Ep$) value when \mathbf{E} and \mathbf{p} are in the same

direction. If θ is non-zero, the dipole will orient itself such that the angle between the electric field and dipole moment becomes zero.

2.2. Dielectrics

A dielectric material is an electrical insulator that can be polarized by the application of an external electric field. The bound charges within the dielectric materials will move in different directions based on the charge sign and form induced dipoles. The strength of the induced dipole is proportional to the electric field.

$$\mathbf{P} = n\alpha\mathbf{E}' \quad (2.3)$$

where \mathbf{E}' is the local electric field, n is the number of molecules per cubic meter, and α is the polarizability of the material which has a unit of F/m^2 . Material polarization causes a net charge in the dielectric which is referred to as bound charges. Bound charge density is given as

$$\rho_b = -\nabla \cdot \mathbf{P} \quad (2.4)$$

Dielectric materials are categorized as polar and non-polar. Polar dielectrics have a permanent dipole while non-polar dielectrics do not have any permanent dipole and applied electric field will induce a dipole within the material.

When a dielectric is subjected to an external electric field, different polarization phenomena could happen. These phenomena could be due to molecular processes (electronic, atomic, orientational) or long-range processes (interfacial polarization). In electronic polarization, the electron cloud and positive nucleus move to different directions in an external electric field inducing a dipole moment. For atomic polarization, the ions of different signs move in different directions, which causes atomic polarizability. Orientational polarization is because of the alignment of permanent dipoles in polar dielectrics. Finally, charges can be accumulated at inhomogeneous boundaries or the surface, resulting in interfacial polarization.

Combining Gauss' law and the bound charge density equation, and considering charge density is a summation of free (ρ_f) and bound (ρ_b) charges, we will have

$$\nabla \cdot (\epsilon_0 \mathbf{E} + \mathbf{P}) = \rho_f \quad (2.5)$$

$\mathbf{D} = \epsilon_0 \mathbf{E} + \mathbf{P}$ is called displacement field. For a linear and isotropic dielectric, \mathbf{P} is proportional to \mathbf{E} .

$$\mathbf{P} = \epsilon_0 \chi \mathbf{E} \quad (2.6)$$

where χ is the susceptibility. Displacement field can be rewritten as

$$\mathbf{D} = \epsilon_0 (1 + \chi) \mathbf{E} = \epsilon_0 \epsilon_r \mathbf{E} \quad (2.7)$$

$\epsilon_r = 1 + \chi$ is a dimensionless number referred as relative permittivity and is the proportionality constant between \mathbf{D} and \mathbf{E} .

In order to examine the polarization of a dielectric in an AC electric field, the concept of complex permittivity must be introduced at first. Consider a parallel plate capacitor which contains a homogenous dielectric material with permittivity $\varepsilon = \varepsilon_0\varepsilon_r$ (Figure 2.1).

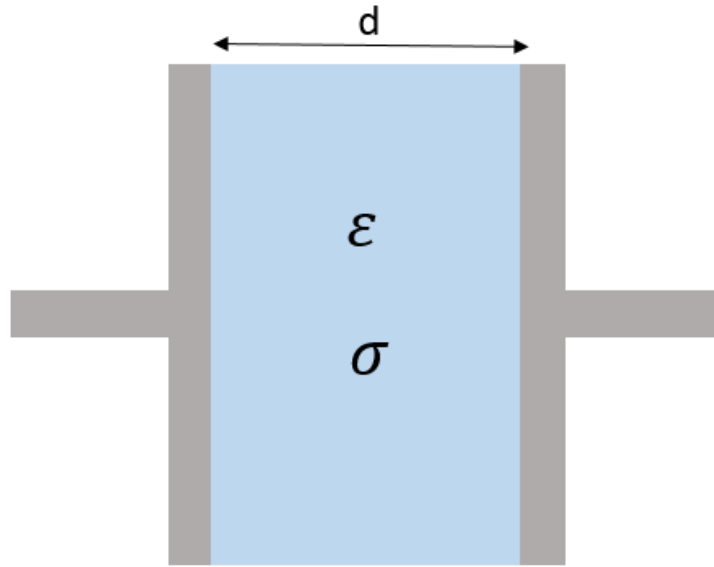


Figure 2.1 A parallel plate electrode with a layer of dielectric material

Each plate has a surface area of A , and the separation distance between two plates is d . If an AC voltage of angular frequency ω is applied to the plates, in case of a loss-free dielectric, the impedance is

$$Z = \frac{1}{j\omega C}; \quad C = \varepsilon \frac{A}{d} \quad (2.8)$$

However, for lossy dielectrics with permittivity ϵ and conductivity σ , the equivalent circuit model can be considered as a loss-free capacitor in parallel with a resistor ($R = \frac{d}{A\sigma}$). As a result, the impedance can be calculated as

$$Z = \frac{R}{1 + j\omega RC} = \frac{1}{j\omega C'}; \quad C' = \epsilon^* \frac{A}{d} \quad (2.9)$$

ϵ^* is called the complex permittivity and is given by

$$\epsilon^* = \epsilon_0 \epsilon_r - j \frac{\sigma}{\omega} \quad (2.10)$$

Another method to introduce complex permittivity is combining the charge conservation equation ($\nabla \cdot \mathbf{J} = -\frac{\partial \rho}{\partial t}$, where \mathbf{J} is the current density) with Gauss's law which yields

$$\nabla \cdot \left(\epsilon_0 \epsilon_r - j \frac{\sigma}{\omega} \right) \mathbf{E} = 0 \quad (2.11)$$

2.2.1. Dielectric Relaxations

As mentioned earlier, local relaxations include atomic, electronic, and orientational. Atomic and orientational polarization will align with electric fields up to $\sim 10^{14}$ Hz, and these mechanisms can be explained by this equation

$$\mathbf{P}_{a,e} = \epsilon_0 \chi_{a,e} \mathbf{E} \quad (2.12)$$

However, for orientational polarization a relaxation time τ_{or} is introduced to account for the time needed for permanent dipoles to orient with the external electric field. This polarization is given by:

$$\mathbf{P}_{or} = \frac{\varepsilon_0 \chi_{or}}{1 + j\omega\tau_{or}} \mathbf{E} \quad (2.13)$$

The total polarization is the summation of atomic, electronic, and orientational polarizations.

$$\mathbf{P}_{tot} = \mathbf{P}_{a,e} + \mathbf{P}_{or} = \varepsilon_0 \left(\chi_{a,e} + \frac{\chi_{or}}{1 + j\omega\tau_{or}} \right) \mathbf{E} \quad (2.14)$$

In the low-frequency limit, $\chi = \chi_{a,e} + \chi_{or} = \varepsilon_s - 1$ and at the high-frequency limit, $\chi = \chi_{a,e} = \varepsilon_\infty - 1$, where ε_s and ε_∞ are the relative permittivity values at low and high-frequency limits. Combining these results, $\chi_{or} = \varepsilon_s - \varepsilon_\infty$ and Equation 2.14 can be written as

$$\mathbf{P}_{tot} = \varepsilon_0 \left(\varepsilon_\infty + \frac{\varepsilon_s - \varepsilon_\infty}{1 + j\omega\tau_{or}} - 1 \right) \mathbf{E} \quad (2.15)$$

As a result, the complex permittivity of the dielectric is

$$\varepsilon^* = \varepsilon_0 \left(\varepsilon_\infty + \frac{\varepsilon_s - \varepsilon_\infty}{1 + j\omega\tau_{or}} \right) - j \frac{\sigma}{\omega} \quad (2.16)$$

Equation 2.16 can be written in the form of $\varepsilon^* = \varepsilon' - j\varepsilon''$, yielding the Debye relationships,

$$\varepsilon' = \varepsilon_0 \left(\varepsilon_\infty + \frac{\varepsilon_s - \varepsilon_\infty}{1 + \omega^2\tau_{or}^2} \right); \quad \varepsilon'' = \varepsilon_0 \left(\frac{(\varepsilon_s - \varepsilon_\infty)\omega\tau_{or}}{1 + \omega^2\tau_{or}^2} \right) + \frac{\sigma}{\omega} \quad (2.17)$$

At low frequencies, the dipole follows electric field changes, and the real part is high. At relaxation frequency ($\frac{1}{2\pi\tau_{rel}}$), dipoles fail to follow the electric field, and the real part starts

to decrease. The imaginary part will have a peak at relaxation frequency. The peak in the imaginary part is due to the heat that is generated during the alignment of the dipole, which is acting against the randomizing effects of the Brownian motion. In other words, the real part of the permittivity is the storage part, while the imaginary part is the dissipative part of electric energy. The static conductivity of the medium also contributes to the dissipation part of the complex permittivity.

The phenomenon described above is usually referred as dielectric relaxation, with $\frac{1}{2\pi\tau_{rel}}$ being the relaxation frequency. Cole and Cole [71] modified Equation 2.16 to account for the distribution of relaxation times seen in experimental results. This equation is as follows

$$\varepsilon^* = \varepsilon_0 \left(\varepsilon_\infty + \frac{\varepsilon_s - \varepsilon_\infty}{1 + j(\omega\tau_{or})^{1-\beta}} \right) - j \frac{\sigma}{\omega} \quad (2.18)$$

where $\beta = 0$ and $\beta = 1$ represent single and infinite relaxation times, respectively.

2.3. Interfacial Polarization

In AC electrokinetics, the system usually consists of dielectric particles suspended in a dielectric fluid. The external electric field will cause accumulation of surface charges at interfaces. This surface charge is frequency-dependent and shows a dispersion behavior, which is known as Maxwell-Wagner interfacial polarization.

The interfacial polarization can be explained using a parallel plate capacitor containing two lossy dielectrics with different electrical properties. A schematic of the mentioned system is shown in Figure 2.2.

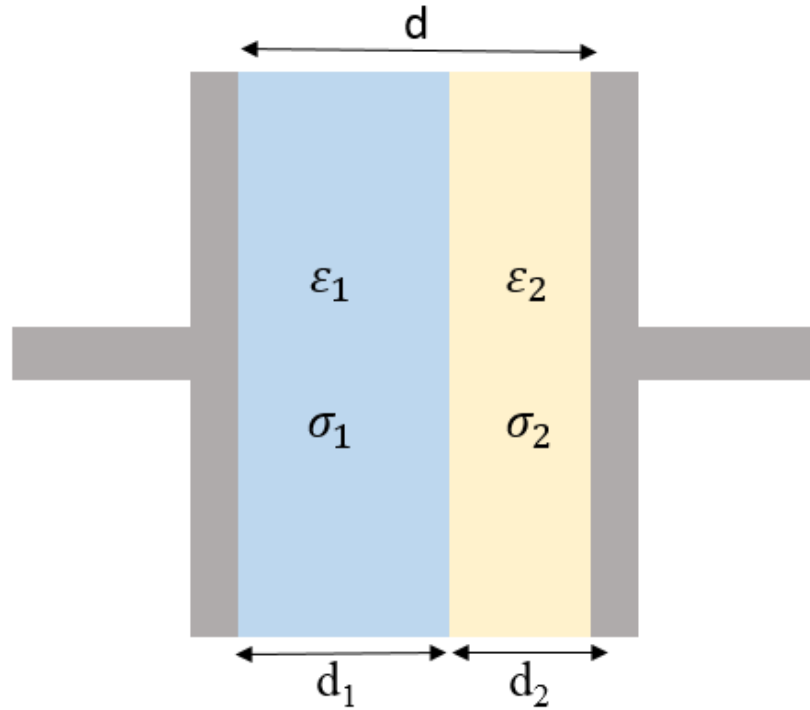


Figure 2.2 A parallel plate electrode with two layers of dielectric material

This system can be considered as elements in series, and the impedance of the system is written as

$$Z = \frac{R_1}{1 + j\omega R_1 C_1} + \frac{R_2}{1 + j\omega R_2 C_2} = \frac{1}{j\omega C}; \quad C = \varepsilon^* \frac{A}{d_1 + d_2} \quad (2.19)$$

Using the Debye formulations, ε^* can be written as

$$\varepsilon^* = \varepsilon' - i\varepsilon'' = \varepsilon_0 \left[\varepsilon_{hf} + \frac{\varepsilon_{lf} - \varepsilon_{hf}}{1 + \omega^2 \tau^2} \right] - i\varepsilon_0 \left[\frac{(\varepsilon_{lf} - \varepsilon_{hf})\omega\tau_{or}}{1 + \omega^2 \tau^2} + \frac{\sigma}{\varepsilon_0 \omega} \right] \quad (2.20)$$

where ε_{hf} , ε_{lf} , τ , and σ are high-frequency permittivity, low-frequency permittivity, relaxation time, and total conductivity, respectively, and are given as

$$\begin{aligned} \varepsilon_{hf} &= \frac{d\varepsilon_1\varepsilon_2}{d_1\varepsilon_2 + d_2\varepsilon_1} & \varepsilon_{lf} &= \frac{d(d_1\varepsilon_1\sigma_2^2 + d_2\varepsilon_2\sigma_1^2)}{(d_1\sigma_2 + d_2\sigma_1)^2} \\ \tau &= \frac{d_1\varepsilon_2 + d_2\varepsilon_1}{d_1\sigma_2 + d_2\sigma_1} & \sigma &= \frac{d\sigma_1\sigma_2}{d_1\sigma_2 + d_2\sigma_1} \end{aligned} \quad (2.21)$$

2.3.1. The effective dipole moment of a spherical particle

Consider a dielectric sphere with radius a and permittivity of ε_p inside a fluid medium with complex permittivity of ε_m and exposed to applied electric field $\mathbf{E} = -E\mathbf{z}$. We want to find the form of particle polarization with a field superposed on E creating a potential φ which satisfies the following conditions:

1. φ is continuous across sphere boundary.
2. Net surface charge on the sphere boundary is zero $\varepsilon_m \frac{\partial \varphi_m}{\partial r} \Big|_{r=a} = \varepsilon_p \frac{\partial \varphi_p}{\partial r} \Big|_{r=a}$.
3. φ satisfies Laplace equation ($\nabla^2 \varphi = 0$).
4. At distances far beyond the sphere $\varphi = -Ez$

If the permittivities are complex and the applied field is harmonic, Equation 2.11 along with the same boundary conditions but with complex permittivity values can be used. As a result, the potential outside (φ_m) and inside (φ_p) of the sphere is derived as [72]

$$\begin{aligned}
\varphi_m &= \left[\left(\frac{\varepsilon_p^* - \varepsilon_m^*}{\varepsilon_p^* + 2\varepsilon_m^*} \right) \frac{a^3}{r^3} - 1 \right] Er \cos \theta \\
&= Ea^3 \left(\frac{\varepsilon_p^* - \varepsilon_m^*}{\varepsilon_p^* + 2\varepsilon_m^*} \right) \frac{\cos \theta}{r^2} - Er \cos \theta \\
\varphi_p &= - \left(\frac{3\varepsilon_m^*}{\varepsilon_p^* + 2\varepsilon_m^*} \right) Er \cos \theta
\end{aligned} \tag{2.22}$$

Based on Equation 2.22, it is clear that the electrical potential in the medium is a superposition of the potential due to the applied external field and the potential due to a dipole moment. Comparing this equation with the dipole moment potential field, the dipole moment is

$$\mathbf{p} = 4\pi\varepsilon_m \left(\frac{\varepsilon_p^* - \varepsilon_m^*}{\varepsilon_p^* + 2\varepsilon_m^*} \right) a^3 \mathbf{E} \tag{2.23}$$

Equation 2.23 shows that polarizability is frequency dependent and can be explained by a factor called the Clausius-Mossotti factor, defined as

$$K = \left(\frac{\varepsilon_p^* - \varepsilon_m^*}{\varepsilon_p^* + 2\varepsilon_m^*} \right) \tag{2.24}$$

Figure 2.3 shows the variations of the real and imaginary part of K with respect to frequency. The real part of K has high and low-frequency limits of $\frac{\sigma_p - \sigma_m}{\sigma_p + 2\sigma_m}$ and $\frac{\varepsilon_p - \varepsilon_m}{\varepsilon_p + 2\varepsilon_m}$, respectively. The imaginary part approaches zero at both frequency limits and has a peak value at relaxation frequency $\left(\frac{1}{2\pi} \left(\frac{\sigma_p + 2\sigma_m}{\varepsilon_p + 2\varepsilon_m} \right) \right)$.

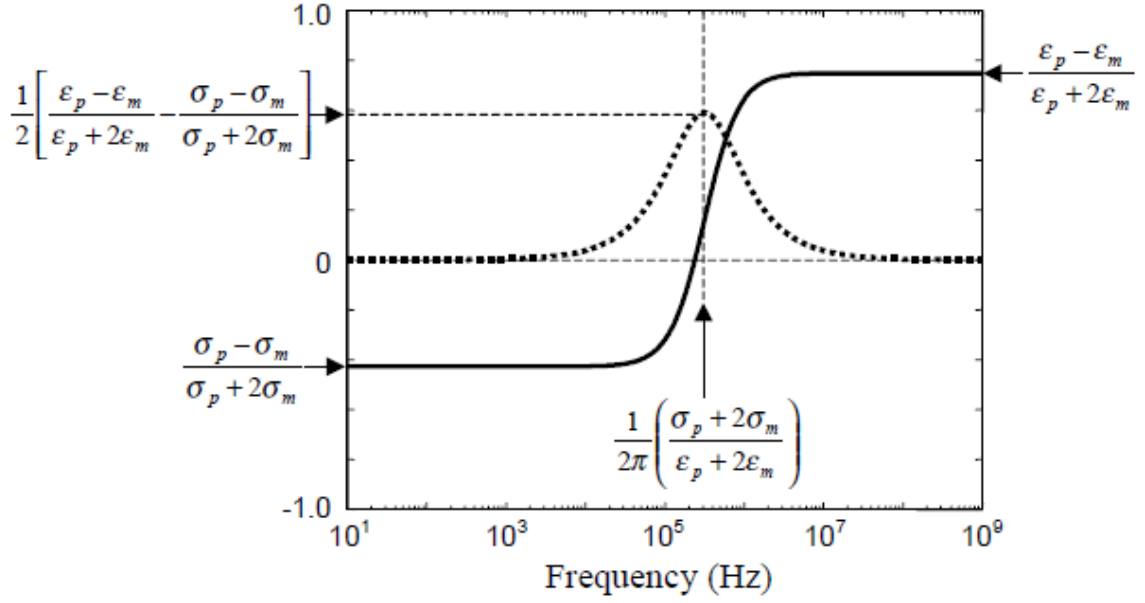


Figure 2.3 Variation of real (solid line) and imaginary parts (dotted line) of K with frequency. Figure adapted from [73]

2.3.2. The effective dipole moment of an ellipsoidal particle

Consider an ellipsoidal particle with semi-axes R_x , R_y , and R_z along the x , y , and z -axes.

When an AC electric field $\mathbf{E} = (E_x, E_y, E_z)$ is applied, the potentials outside and inside of ellipsoid are calculated as [72]

$$\varphi_m = - \sum_{k=x,y,z} E_k k \left\{ 1 - \frac{\epsilon_p^* - \epsilon_m^*}{\epsilon_m^* + (\epsilon_p^* - \epsilon_m^*) L_k} L'_k \right\} \quad (2.25)$$

$$\varphi_p = - \sum_{k=x,y,z} E_k k \frac{\varepsilon_m^*}{\varepsilon_m^* + (\varepsilon_p^* - \varepsilon_m^*)L_k} \quad (2.26)$$

where L_k and L'_k are depolarization factors along the k-axis and defined as

$$L_k = \frac{R_x R_y R_z}{2} \int_0^\infty \frac{ds}{(R_k^2 + s)R_s}; \quad (2.27)$$

$$L'_k = \frac{R_x R_y R_z}{2} \int_s^\infty \frac{ds}{(R_k^2 + s)R_s}; \quad R_s = \sqrt{(R_x^2 + s)(R_y^2 + s)(R_z^2 + s)} \quad (2.28)$$

At a point a distance r from the ellipsoid, where r is large, L'_k is approximated as

$$L'_k \approx \frac{R_x R_y R_z}{3} \frac{1}{r^3} \quad (2.29)$$

Using the above approximation and the method explained in section 2.3.1, the dipole moment in each direction is equal to

$$p_k = 4\pi\varepsilon_m^*\varepsilon_0 \frac{\varepsilon_p^* - \varepsilon_m^*}{\varepsilon_m^* + (\varepsilon_p^* - \varepsilon_m^*)L_k} \frac{R_x R_y R_z}{3} E_k \quad (2.30)$$

The total dipole moment \mathbf{p} is the summation of x , y , and z components.

$$\mathbf{p} = p_x \mathbf{i}_x + p_y \mathbf{i}_y + p_z \mathbf{i}_z \quad (2.31)$$

where i_x , i_y , and i_z are the basis vectors in x , y , and z directions, respectively. The component of the dipole moment in the E -direction is given by

$$\begin{aligned} p' &= p_x \cos \varphi_x + p_y \cos \varphi_y + p_z \cos \varphi_z \\ &= \frac{4\pi R_x R_y R_z}{3} \varepsilon_m^* \varepsilon_0 E \sum_{k=x,y,z} \frac{\varepsilon_p^* - \varepsilon_m^*}{\varepsilon_m^* + (\varepsilon_p^* - \varepsilon_m^*) L_k} \cos^2 \varphi_k \end{aligned} \quad (2.32)$$

where φ_k is the angle between k -axis and E -direction.

2.4. Complex permittivity of suspensions

2.4.1. Complex permittivity of the diluted suspension

If we consider that the suspension consists of N particles per unit volume and each one has a dipole moment of p' in the E -direction, the polarization of the system is $p = Np'$ and displacement field is calculated as

$$\mathbf{D} = \varepsilon_m^* \varepsilon_0 \mathbf{E} + Np' = \varepsilon^* \varepsilon_0 \mathbf{E} \quad (2.33)$$

As a result, the complex permittivity of oriented ellipsoids in the medium is obtained as

$$\varepsilon^* = \varepsilon_m^* \left[1 + \Phi \sum_{k=x,y,z} \frac{\varepsilon_p^* - \varepsilon_m^*}{\varepsilon_m^* + (\varepsilon_p^* - \varepsilon_m^*) L_k} \cos^2 \varphi_k \right] \quad (2.34)$$

where Φ is the volume fraction of particles ($\Phi = \frac{4\pi R_x R_y R_z N}{3}$). For the case of randomly oriented ellipsoid particles, $\cos^2 \varphi_k = 1/3$ and the above equation becomes

$$\varepsilon^* = \varepsilon_m^* \left[1 + \frac{1}{3} \Phi \sum_{k=x,y,z} \frac{\varepsilon_p^* - \varepsilon_m^*}{\varepsilon_m^* + (\varepsilon_p^* - \varepsilon_m^*) L_k} \right] \quad (2.35)$$

In the case of spherical particles, $L_k = 1/3$ and the above equation reduces to so-called Maxwell-Wagner relation.

$$\frac{\varepsilon^* - \varepsilon_m^*}{\varepsilon^* + 2\varepsilon_m^*} = \Phi \frac{\varepsilon_p^* - \varepsilon_m^*}{\varepsilon_p^* + 2\varepsilon_m^*} \quad (2.35)$$

2.4.2. Complex permittivity of concentrated suspension

For concentrated particle suspensions, the interaction between induced dipoles must be considered. However, effective medium theory can be applied here, which assumes that each particle is dispersed in the effective medium, including particles. The change in complex permittivity $d\varepsilon^*$ due to the addition of particles can be calculated by substituting $\varepsilon^* + d\varepsilon^*$ for ε^* , ε_m^* for ε_m^* , and Φ with $\frac{d\Phi'}{1-\Phi'}$ in Equation 2.35 (Φ is the volume fraction of particles in suspension) and integrating the equation till we reach the final volume fraction.

$$\int_0^\Phi -\frac{d\Phi'}{1-\Phi'} = \int_{\varepsilon_m^*}^{\varepsilon^*} \frac{3}{\varepsilon^* (\varepsilon^* - \varepsilon_p^*)} \left[\sum_{k=x,y,z} \frac{1}{\varepsilon^* + (\varepsilon_p^* - \varepsilon_m^*) L_k} \right]^{-1} d\varepsilon^* \quad (2.36)$$

For spherical particles, the above equation reduces to so-called Bruggemann-Hanai mixture relation.

$$1 - \Phi = \left(\frac{\varepsilon^* - \varepsilon_p^*}{\varepsilon_m^* + 2\varepsilon_p^*} \right) \left(\frac{\varepsilon_m^*}{\varepsilon^*} \right)^{\frac{1}{2}} \quad (2.37)$$

2.4.3. Shell models

The simplest model of a biological cell is a single shell model that takes into account the cell membrane and the cytoplasm. Consider an ellipsoid with outer and inner semiaxes of R_k and R_{ik} along the k -axis, and inner and shell complex permittivities of ε_1^* and ε_2^* . By solving the Laplace equation and calculating dipole moment, the complex permittivity of the shell ellipsoid particle along k -axis (ε_{pk}^*) is calculated as [72]

$$\varepsilon_{pk}^* = \varepsilon_2^* \left[1 + \frac{v(\varepsilon_1^* - \varepsilon_2^*)}{\varepsilon_2^* + (\varepsilon_1^* - \varepsilon_2^*)(L_{ik} - vL_k)} \right] \quad (2.38)$$

With

$$L_{ik} = \frac{R_{ix}R_{iy}R_{iz}}{2} \int_0^\infty \frac{ds}{(R_{ik}^2 + s)R_{is}}; \quad R_{is} = \sqrt{(R_{ix}^2 + s)(R_{iy}^2 + s)(R_{iz}^2 + s)}; \quad v = \frac{R_{ix}R_{iy}R_{iz}}{R_xR_yR_z} \quad (2.39)$$

For spherical biological cells, the cytoplasm is covered with a thin membrane. As a result, the complex permittivity of the cell as given by the single shell model (Figure 2.4a) is

$$\varepsilon_c^* = \varepsilon_{mem}^* \frac{\gamma^3 + 2 \left(\frac{\varepsilon_{cyt}^* - \varepsilon_{mem}^*}{\varepsilon_{cyt}^* + 2\varepsilon_{mem}^*} \right)}{\gamma^3 - \left(\frac{\varepsilon_{cyt}^* - \varepsilon_{mem}^*}{\varepsilon_{cyt}^* + 2\varepsilon_{mem}^*} \right)} \quad (2.40)$$

Here, *mem* and *cyt* subscripts indicate the membrane and the cytoplasm, respectively. The factor γ is a function of the cell radius, a , and the membrane thickness, d_{mem} , and can be expressed as $\gamma = a/(a - d_{mem})$.

A more complex model is often used to model eukaryotic cells is the double shell model (Figure 2.4b). Eukaryotic cells have a nucleus enclosed within membranes. The double shell model approximates the cell as two concentric shells: The outer representing the cell membrane and the inner representing the nuclear envelope. Between the two shells lies the conductive cytoplasm. At the center of the cell lies the nucleoplasm. The complex permittivity of the double shell model can be formulated by successive application of Equation 2.38 that shows the complex permittivity of a single shell ellipsoid. For spherical biological cells, the double-shell model can be expressed as [74]

$$\gamma_1 = R_{ne}/(R_{ne} - d_{ne}) \quad (2.41)$$

$$\gamma_2 = (R_{cell} - d_{mem})/R_{ne} \quad (2.42)$$

$$\gamma_3 = R_{cell}/(R_{cell} - d_{mem}) \quad (2.43)$$

$$\varepsilon_1^* = \varepsilon_{ne}^* \frac{\gamma_1^3 + 2 \left(\frac{\varepsilon_{np}^* - \varepsilon_{ne}^*}{\varepsilon_{np}^* + 2\varepsilon_{ne}^*} \right)}{\gamma_1^3 - \left(\frac{\varepsilon_{np}^* - \varepsilon_{ne}^*}{\varepsilon_{np}^* + 2\varepsilon_{ne}^*} \right)} \quad (2.44)$$

$$\varepsilon_2^* = \varepsilon_{cyt}^* \frac{\gamma_2^3 + 2 \left(\frac{\varepsilon_1^* - \varepsilon_{cyt}^*}{\varepsilon_1^* + 2\varepsilon_{cyt}^*} \right)}{\gamma_2^3 - \left(\frac{\varepsilon_1^* - \varepsilon_{cyt}^*}{\varepsilon_1^* + 2\varepsilon_{cyt}^*} \right)} \quad (2.45)$$

$$\varepsilon_c^* = \varepsilon_{mem}^* \frac{\gamma_3^3 + 2 \left(\frac{\varepsilon_2^* - \varepsilon_{mem}^*}{\varepsilon_2^* + 2\varepsilon_{mem}^*} \right)}{\gamma_3^3 - \left(\frac{\varepsilon_2^* - \varepsilon_{mem}^*}{\varepsilon_2^* + 2\varepsilon_{mem}^*} \right)} \quad (2.46)$$

Here, *mem*, *cyt*, *ne* and *np* subscripts denote the cell membrane, cytoplasm, nuclear envelope and nucleoplasm properties respectively. The cell and nuclear radii are denoted by R_{cell} and R_{ne} , respectively. The cell membrane thickness and the nuclear membrane thickness are denoted by d_{mem} and d_{ne} , respectively.

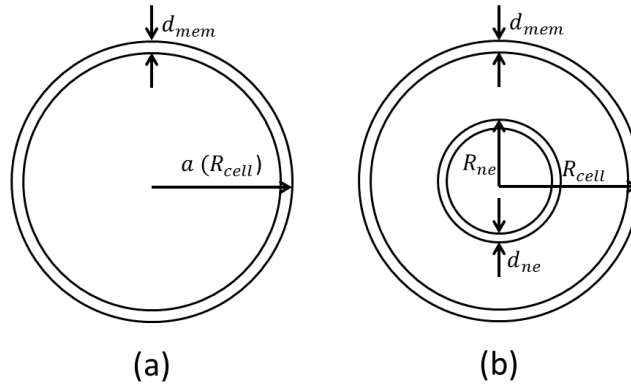


Figure 2.4 Schematic for the Single-Shell and Double shell models.

2.5. Electrical forces on particles

2.5.1. Electrophoresis

Electrophoresis is the motion of charged particles in a fluid subjected to the uniform electric field. Electrophoresis of positively and negatively charged particles are called cataphoresis and anaphoresis, respectively. Electrophoresis is rooted in Coulomb force on a particle which is given by a surface integral as

$$F_{EP} = QE = \int_s \sigma_q dSE \quad (2.47)$$

where Q and σ_p denote total charge and charge density, respectively. In an AC electric field, this force causes oscillatory motion with time-average equal to zero.

When a charged particle is placed in an aqueous medium, a double layer forms. The double layer consists of two distinct regions: 1. Stern layer which is immobile and comprised of ions with opposite charge to the surface charge, 2. The diffuse layer which mostly consists of counterions. Because of the presence of the double layer, the charged particle appears to have zero net charges. However, when it is placed in an electric field, it moves. The diffuse layer has ions with opposite sign of surface charge, and they would move into the direction opposite to particle movement in a vacuum. As a result, the moving ions push the particle in the opposite direction, which is the same direction that the particle would move in a vacuum.

2.5.2. Dielectrophoresis (DEP)

Consider a dipole in a non-uniform electric field, as shown in Figure 2.5. The two charges will have different exerted forces, and the net force is equal to

$$\mathbf{F} = Q\mathbf{E}(r + d) - Q\mathbf{E}(r) \quad (2.48)$$

Using the Taylor series expansion, the above equation can be rewritten as

$$\mathbf{F} = Q\mathbf{E}(r) + Q(\mathbf{d} \cdot \nabla)\mathbf{E} + H.O.T - Q\mathbf{E}(r) \approx (\mathbf{p} \cdot \nabla)\mathbf{E} \quad (2.49)$$

Based on this equation, a non-uniform electric field is necessary to have a non-zero force.

Dielectrophoresis is the motion of polarizable particle suspended in an electrolyte solution and subjected to a spatially non-uniform electric field. Assume an applied potential of frequency ω , the instantaneous applied field at location r and time t is given by

$$E(r, t) = \text{Re}[E(r)e^{j\omega t}] \quad (2.50)$$

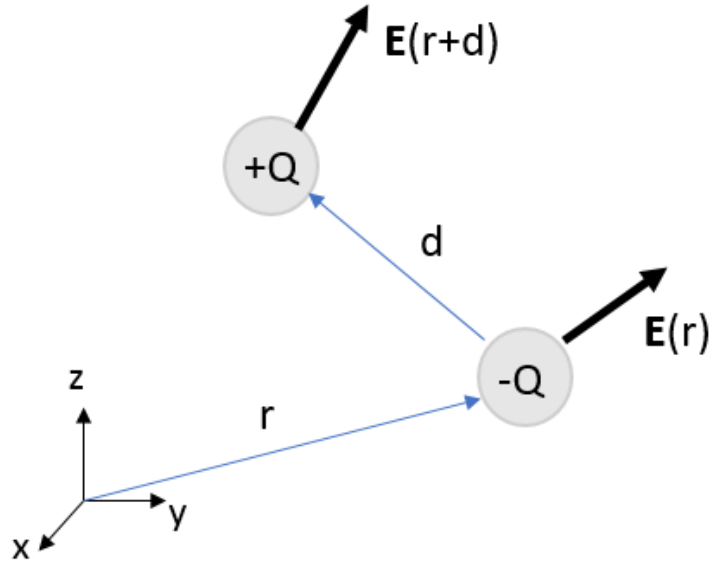


Figure 2.5 Electrical forces on a dipole moment in a non-uniform electric field

Based on Equations 2.23 and 2.50, the instantaneous dipole moment value for a spherical particle of radius a at time t is

$$p(t) = \text{Re}[4\pi\epsilon_m a^3 K E(r) e^{j\omega t}] \quad (2.51)$$

From Equation 2.49, the DEP force is

$$F_{DEP}(t) = \text{Re}[p e^{j\omega t}] \cdot \nabla \text{Re}[E e^{j\omega t}] \quad (2.52)$$

Substituting for the effective dipole moment from Equation 2.51, the time-averaged DEP force on a homogenous spherical particle of radius R is

$$\langle F_{DEP} \rangle = 2\pi\epsilon_0\epsilon_m R^3 \text{Re}[K] \nabla |E|^2 \quad (2.53)$$

Based on Equation 2.53, the sign of $\text{Re}[K]$ shows the DEP force direction. If the particle is more polarizable than the medium, $\text{Re}[K]$ is positive and the DEP force will move the particle to higher electric field region. This phenomenon is called positive dielectrophoresis (pDEP). However, if the medium is more polarizable than the particle, $\text{Re}[K]$ will be negative, and the DEP force will push the particle to lower electric field regions. Similarly, this phenomenon is called negative dielectrophoresis (nDEP). The frequency at which $\text{Re}[K]$ changes sign is called the cross-over frequency.

Chapter 3

DIELECTROPHORETIC ASSISTED LOADING AND UNLOADING OF MICRO-WELLS FOR IMPEDANCE SPECTROSCOPY

Dielectric spectroscopy (DS) is a non-invasive, label-free, and fast technique for measuring dielectric properties of biological cells in real time. We demonstrate a microchip that consists of electro-activated micro-well arrays for positive dielectrophoresis (pDEP) assisted cell capture, DS measurements, and negative dielectrophoresis (nDEP) driven cell unloading; thus, providing a high throughput cell analysis platform. To the best of our knowledge, this is the first microfluidic chip that combines electro-activated micro-wells and DS to analyze biological cells. Device performance is tested using *Saccharomyces Cerevisiae* (yeast) cells. DEP response of yeast cells is determined by measuring their Clausius-Mossotti (K) factor using biophysical models in a parallel plate micro-electrode geometry. This information is used to determine the excitation frequency to load and unload wells. The effect of yeast cells on the measured impedance spectrum was examined both experimentally and numerically. A good match between the numerical and experimental results establishes the potential use of the microchip device for extracting sub-cellular properties of biological cells in a rapid and non-expensive manner.

3.1. Materials and Methods

Photolithography supplies (photoresists, developers, and remover) were purchased from Microchem Corp. (Westborough, MA, USA). All other chemicals used were of analytical

grade and obtained from Sigma-Aldrich (St Louis, MO, USA). All solutions were prepared with 18 M Ω ·cm ultrapure water obtained from Millipore Alpha-Q water system (Bedford, MA, USA). A Leo-Zeiss 1450VPSE variable pressure electron microscope equipped with an EDAX Genesis 4000 XMS System was used for SEM characterization. SEM images were taken at 3000X magnification factor and 5 kV resolution. Yeast cells (*Saccharomyces cerevisiae*) were grown in a shaking incubator at 30°C and under constant shaking speed at 250 rpm. The growth medium (YEPD Broth) consisted of 20 g/l peptone, 10 g/l yeast extract, 20 g/l dextrose dissolved in deionized water. The cells were collected at the stationary growth phase after one day of culture in the shaking incubator, and they were harvested by centrifugation for 2 min at 3000 rpm and suspended in low conductivity buffers (LCB). The harvested cells were spheroidal and 6 μ m in diameter. LCB is an isotonic buffer consisting of 229 mM sucrose, 16 mM glucose, 1 μ M CaCl₂, and 5 mM Na₂HPO₄ in double distilled water (pH 7.4).

3.1.1 Photolithography

The microfluidic chips used for experiments were fabricated using standard photolithography techniques. Figure 3.1 shows the fabrication procedure. First, the glass substrates were cleaned for 10 minutes using ultrasonic cleaning in 1 M KOH solution, acetone, and isopropyl alcohol (IPA), respectively, followed by rinsing with type-1 deionized (DI) water, and drying with Nitrogen. The slides were then placed on a hot plate that was kept at 140°C for 15 minutes to be completely dried. The positive photoresist (S1813) was spin coated on the slides using a two-step process with the following rotation speeds: 1,000 rpm for 10 s and 4,000 rpm for 30 s with 300 rpm/s acceleration/deceleration.

Coated slides were soft baked on a hot plate at 115°C for 1 minute, and then, they were exposed to 110 mJ/cm² UV light through a transparency mask using Karl SUSS MJB3 mask aligner. The UV exposed area was dissolved in MF-26A developer solution by immersing the slides inside the solution for 10 s. The developed slides were cleaned using DI water and dried by the gentle flow of Nitrogen. Afterward, the slides were placed inside sputter coater (EMS300TD, Emitech). The sputter coater was adjusted to coat slides with 3 nm Chromium layer and 22 nm gold layer. The slides were then immersed in PG remover solution at 80°C to remove the unexposed photoresist and metal layers on top of it. In the next step, negative photoresist (SU8-3025) was spin coated under the same conditions as those used for the positive photoresist. The photoresist was then soft baked on a hot plate at 95°C for 12 minutes and was exposed to 400 mJ/cm² UV light. Immediately after exposure, the slides were post-exposure baked on a hot plate at 95°C for 3 minutes and 40 seconds. Finally, the slides were immersed in SU8 developer to remove the unexposed areas.

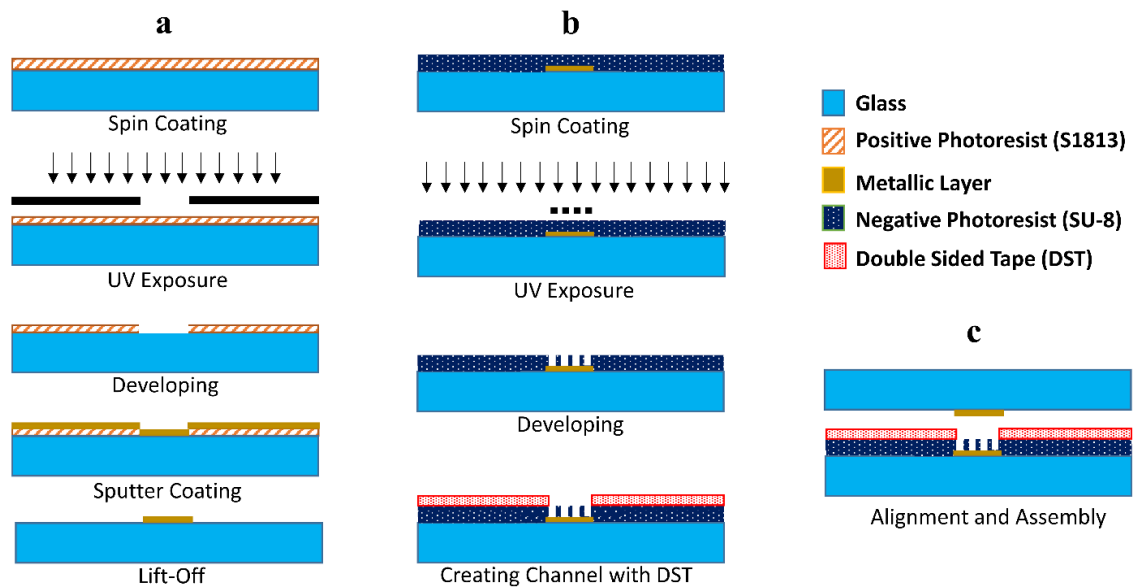


Figure 3.1 Microfabrication process of a DEP chip using two-step photolithography process. a) Electrode fabrication, b) micro-wells and micro-channel fabrication, and c) electrode alignment and device assembly.

3.1.2. Device assembly

The channels for fluid flow were fabricated using 70 μm thickness double-sided tapes (DST) that were cut by a craft cutter (Silver Bullet). Finally, the slide containing the micro-wells and the electrode was aligned with the top electrode using the mask aligner. The assembled device was placed in a convection oven at 75°C to enhance adherence of the double-sided tape to glass slides. Figure 3.2a shows the assembled microfluidic device composed of micro-wells and the microchannel sandwiched between an electrode pair.

Figure 3.2b illustrates the orientation of micro-wells on the gold electrode. There are 441 micro-wells in a 21×21 array, where each column is placed with an offset relative to the neighboring column to increase the chance of trapping the cells in a flow-through system. This configuration also maximizes the volume fraction of cells in the device. Figure 3.2c is the SEM image of one of the micro-wells. It can be seen that the wells are fully developed in the SU-8 developing process. Smooth well-corners reduce extremely high electric fields at the edges and decrease the probability of cell attachment on well-corners due to pDEP. The inlet and outlet ports of the microchannel were drilled using a diamond drill bit before joining the two parts. Two pieces of PDMS were used to ensure leak-free fluidic port connections. Strong irreversible binding between PDMS and glass was obtained using an oxygen plasma cleaner. Copper tape was used for electrical connections, and the connection between the copper tape and gold electrode was achieved using silver epoxy (MG chemicals). Figure 3.2d illustrates the working principle of the microfluidic device. Firstly, biological cells are captured inside the micro-wells using the pDEP force, and then the microfluidic device is connected to a high precision impedance analyzer (HP Agilent 4194A), and the impedance spectra are measured. Finally, cells are extracted from the wells using nDEP forces, and they are directed towards the outlet using fluid flow generated by a syringe pump.

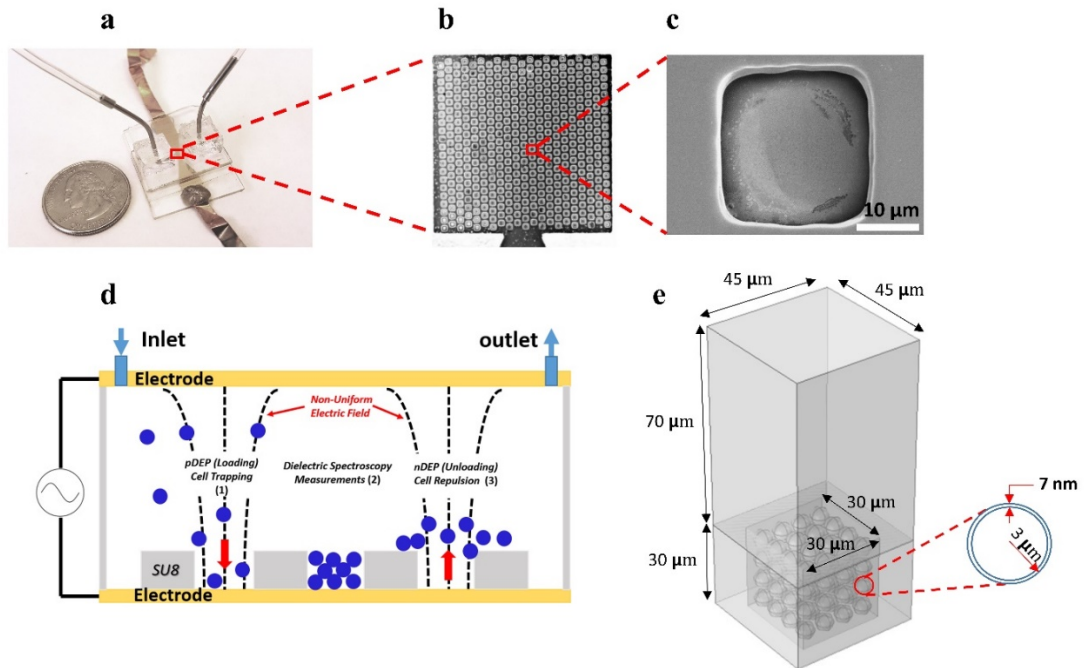


Figure 3.2 a) Assembled microfluidic chip, b) a microscopy picture of the gold electrode and micro-wells, c) SEM image of one micro-well, d) the working principle of the microfluidic device, and e) The computational domain consisting of a medium solution, SU-8, and spherical yeast cells. The yeast cells are modeled consisting of an inner cytoplasm covered by a membrane modeled as an interface.

3.1.3. Experimental setup

The thickness of the electrodes is about 25 nm, which maintains its transparent nature and allows observation of biological cells between the electrode pairs under a microscope. Most of the previous studies used ITO (Indium Tin Oxide) as transparent electrodes. However, the resistivity of ITO ($3.0\text{-}160 \times 10^{-4} \Omega \cdot \text{cm}$ [75]) is higher than gold ($2.04 \times 10^{-5} \Omega \cdot \text{cm}$ [76]).

The transparency of thin gold electrodes, its low resistivity, bio-compatibility [77], and chemical inertness led us to select gold as the electrode material. To image the biological cells, the microfluidic device was placed on an inverted microscope stage (Olympus IX81). The inlet port was connected to a syringe pump (NE-4000) to feed the microfluidic device with a 1% yeast cell suspension, and the outlet port was connected to a drain. Electrical ports were connected to a function generator (Tektronix AFG3102) which was programmed to apply AC signals with a desired amplitude and frequency for DEP assisted loading and unloading of the micro-wells. After capturing the cells, the electrical ports were connected to high and low terminals of a high precision impedance analyzer (HP Agilent 4194A) through a test fixture (HP 16047A). Impedance measurements were performed in 1 kHz-40 MHz frequency range, and the measured data were recorded using MATLAB R2014b software.

3.1.4. Numerical modeling

The computational domain consists of spherical cells located at the bottom of a $30 \times 30 \times 30$ μm well. The well itself is placed in a microchannel with 70 μm depth. A schematic of the simulation domain is shown in Figure 3.2e. The bottom part of the domain (the well-surroundings) is made up of negative photoresist SU-8. Top and inside of the well (except cells) is filled with a solution. The cells were modeled as spherical membranes encapsulating the cytoplasm. The material electrical properties used in the numerical simulations are as follows. The SU-8 photoresist has a relative permittivity of 3.2 and negligible electrical conductivity [78]. The medium is a low conductivity buffer (LCB)

which has a relative permittivity of 80 and electrical conductivity of 0.05 S/m. Dielectric properties of *Saccharomyces Cerevisiae* (yeast) cells were measured in a microfluidic device consisting of parallel plate electrodes in a microchannel, and the subcellular electrical properties were calculated using the methodology given in [79]. Yeast cells' inner cytoplasm and outer layer are found to have relative permittivities of 60 and 12.6 and electrical conductivities of 0.3376 and 6.27×10^{-5} S/m, respectively. These results are in good agreement with previously published results [80].

The electric field was modeled using a combination of Gauss' and charge conservation equations in the frequency domain, as shown in Equation 2.11:

$$\nabla \cdot \left(\varepsilon_0 \varepsilon_r - j \frac{\sigma}{\omega} \right) \mathbf{E} = 0 \quad (2.11)$$

where σ is the electrical conductivity, \mathbf{E} is the electric field and is equal to negative gradients of electric potential $\mathbf{E} = -\nabla\phi$. Also, ε_r and ε_0 represent relative permittivity and vacuum permittivity, respectively.

Electrodes are located at the bottom and top surfaces of the domain. Boundary conditions on the electrodes were 1 V and 0 V for the bottom and top surfaces, respectively. All side surfaces were considered periodic due to a large number of wells, separated 15 μm from each other. The contact impedance boundary condition was used to represent the cell membrane, which approximates a thin layer of material that obstructs the flow of current normal to the boundary, but does not introduce any additional conduction path tangential to the boundary. COMSOL Multiphysics software was used for discretization of the geometry and numerical solution of the equations above in the frequency domain. Grid

refinement studies were done to ensure the convergence of the numerical solution. More information on grid refinement study is presented in the Appendix (Figure 3.A1).

3.1.5. DEP Theory and Dielectric Spectroscopy

DEP is the motion of polarizable particles suspended in an ionic solution and subjected to a spatially non-uniform external electric field. The time-averaged dielectrophoretic force generated by the constant phase electric field is given by Equation 2.53:

$$\langle F_{DEP} \rangle = 2\pi\epsilon_0\epsilon_m R^3 \text{Re}[K] \nabla |E|^2 \quad (2.53)$$

where R is the radius of the particle, ϵ_0 is permittivity of vacuum, ϵ_r is relative permittivity of the medium, ∇E^2 is the gradient of the square of the electric field, and $\text{Re}[K(\omega)]$ is the real part of the Clausius-Mossotti factor, which is written as $K(\omega) = \frac{\epsilon_p^* - \epsilon_m^*}{\epsilon_p^* + 2\epsilon_m^*}$, where $*$, p , and m denotes complex value, particle, and medium, respectively. The complex permittivity is calculated as $\epsilon^* = \epsilon - \frac{j\sigma}{\omega}$, where ϵ is the permittivity, σ is the conductivity, $j = \sqrt{-1}$ and ω is the angular frequency. The sign of $\text{Re}[K(\omega)]$ distinguishes positive and negative DEP responses. Particles more polarizable than the medium are pulled towards higher electric fields and exhibit pDEP response, while particles less polarizable than the medium are repelled towards lower electric fields and exhibit nDEP.

Dielectric spectroscopy is a well-known non-invasive technique to measure the electrical properties of cell suspensions. In this method, a small AC voltage is applied to a cell suspension, and the response current is measured. The impedance is then calculated by

dividing the voltage by current. This process is repeated in the desired frequency range, and analyzing impedance spectrum enables determination of the dielectric properties of individual components of the suspension. Since the applied voltage for dielectric spectroscopy is very small (200 mV) and the process is very fast (<5 s), the spectroscopy signal will not have a considerable effect on the cell packing. Sabuncu *et al.* [79] developed a microfluidic device to analyze the impedance spectrum of cell suspensions. In this method, the effect of electrode polarization is extracted by fitting the impedance spectrum into a combination of the constant phase element and Cole-Cole model [72]. Fitting the corrected dielectric spectrum using the Maxwell-Wagner mixture model [72] allows determination of the Clausius-Mossotti factor. Moreover, modeling biological cells using single-shell and double-shell models allows the extraction of the dielectric properties of sub-cellular components [79].

3.2 Results and Discussion

The electric field lines will be concentrated within the micro-wells, exhibiting high electric fields inside the micro-wells and lower electric fields outside of the micro-wells due to the electrodes' orientation. The numerically calculated electric fields are given in Figure 3.3. These electric field gradients enable DEP-based cell manipulation. For example, cells can be loaded into the micro-wells using pDEP frequency, where $\text{Re}(K)$ is positive, and they can be unloaded changing frequency to nDEP one, where $\text{Re}(K)$ becomes negative.

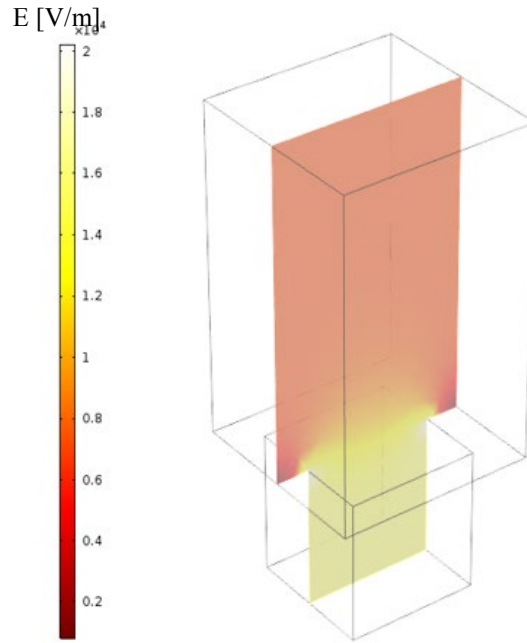


Figure 3.3 Simulated electric field distribution in a cross-sectional plane located in the middle of a micro-well

To determine the frequencies for loading and unloading the micro-wells, the real part of the K factor is calculated using a device with parallel plate electrodes, and the procedure is explained by Sabuncu *et al.* [79]. The details of the K factor measurement is presented in the Appendix. Figure 3.4a shows the time-averaged real part of the K factor for yeast cells suspended in LCB (0.05 S/m) in 1 kHz-40 MHz frequency range at different periods. The time-averaged data was obtained using repeated measurements at every two minutes in 10-minute periods. This figure illustrates the time-dependent behavior of yeast cells that could result from the ion exchange between the cell cytoplasm and LCB medium. Results show negligible changes in the crossover frequency within 10 minutes, while the DEP

experiments are conducted within a couple of minutes following the introduction of cells to the device.

Using K spectrum of cells at 0-10 minutes, pDEP and nDEP responses are expected at $f = 5$ MHz and $f = 10$ kHz frequencies, respectively. These frequencies were tested experimentally using the micro-well setup. In the experiments, the flow was initiated at 1 ml/hr flow rate, and simultaneously, the electrodes were energized at 2 V_{pp} AC voltage to manipulate the cells. Figures 3.4b and 3.4c verify DEP response of yeast cells suspended in 0.05 S/m LCB, at 5 MHz and 10 kHz, respectively. These figures clearly show that at 5 MHz, cells are captured inside the micro-wells by gravitational and pDEP forces, while at 10 kHz, nDEP pushes the yeast cells outside the wells, against gravity. Finally, the cells are washed away, and the microchip is free of the cells, as shown in Figure 3.4d. Strong nDEP forces overwhelming the gravitational force are crucial for unloading the device. Simple force equilibrium relations for a single yeast cell estimates that it takes more than 1 minute for cells to occupy the wells under gravitational and buoyancy forces. Furthermore, not all the cells will settle down inside the micro-wells by these forces.

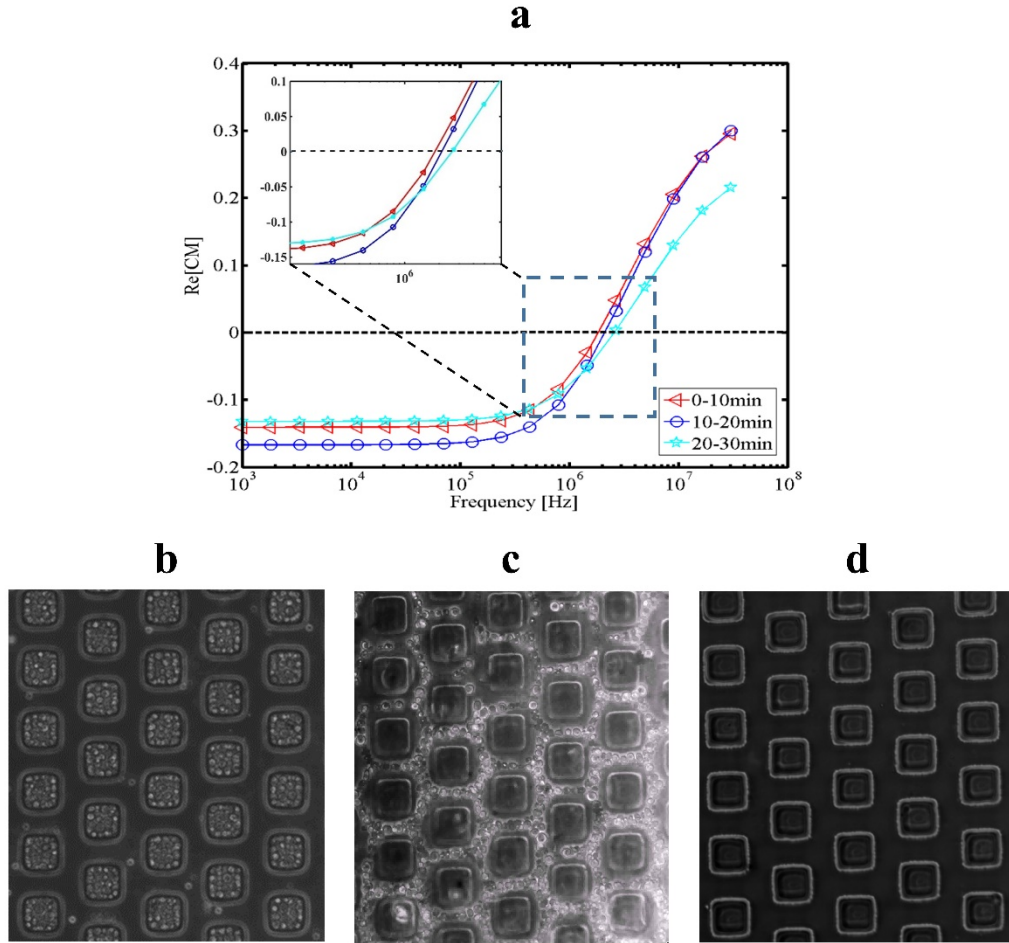


Figure 3.4 a) The real part of Clausius-Mossotti factor ($\text{Re}(K)$) for yeast cells suspended at 0.05 S/m LCB solution as a function of frequency for 0-10, 10-20, and 20-30 minutes time periods after being placed in the LCB solution from growth media. The procedure for extracting Clausius-Mossotti factor is the same as in [79]. The response of yeast cells to $2V_{pp}$ AC electric field at b) $f = 5$ MHz, and c) $f = 10$ kHz, d) clean array after the yeast cells are washed away.

Experimental impedance results (Figure 3.5) show that on the impedance spectra, there is a considerable effect of cells being concentrated inside the micro-wells than just having randomly dispersed cells between the electrodes.

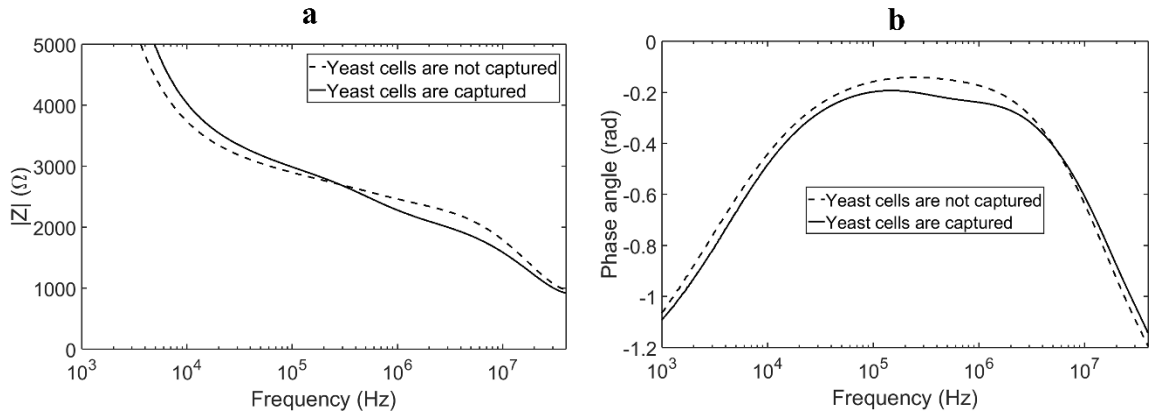


Figure 3.5 Comparison between impedance data for yeast cells captured inside micro-wells and not captured.

Moreover, the pDEP force was applied for 5 seconds at four different initial yeast concentrations (0.5, 1.5, 2.5, and 3.5%) in a 0.05 S/m LCB solution to show the effect of degree of loading in the micro-wells. The impedance magnitude data is shown in Figure 3.6. Experimental results show that the results for 0.5, 1.5, and 2.5% are different, but after 2.5%, the impedance magnitude data reaches a steady state, which suggests that micro-wells are fully loaded. Furthermore, the electrodes are energized for different periods, and the analysis shows that after 10 s, the impedance spectrum does not change, which means that the micro-wells are full. As a result, it is concluded that the loading efficiency of the

DEP device is 60-70 cells per well in 10 s using a 1% volume fraction yeast cell suspension at 2 V_{pp} and 5 MHz excitation.

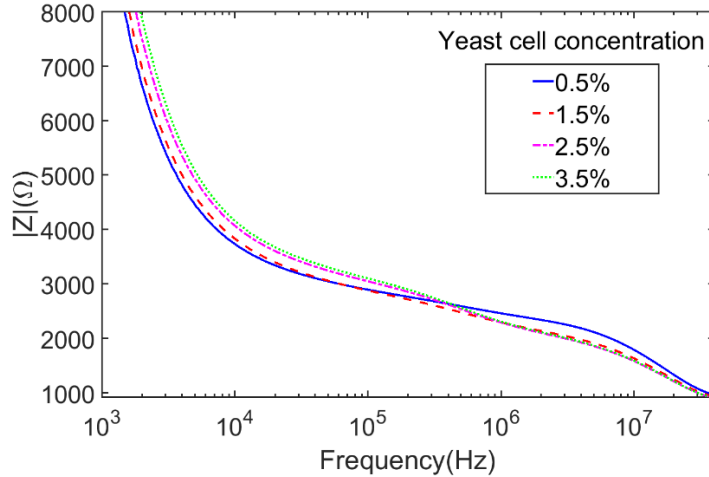


Figure 3.6 Impedance magnitude value spectrum for applying pDEP for 5 seconds at different initial yeast concentration in 0.05 S/m LCB solution.

Yeast growth medium has a conductivity of around 0.20 S/m, whereas mammalian cells cultures have a conductivity on the order of 1 S/m. At high conductivities (~ 1 S/m), pDEP is non-existent for mammalian cells [81]. Moreover, for high conductivity buffers, the electrode polarization effect dominates the system, and the DS is not accurate. However, for yeast cells, pDEP still is strong enough to capture cells in their growth medium, and the experiments conducted at 0.20 S/m medium conductivity, which is close to the yeast growth medium, demonstrates that the device is capable of manipulating yeast cells in their growth medium. To find out how the presence of yeast cells will change the impedance spectrum of the device, yeast cells are suspended in 0.01, 0.05, and 0.20 S/m LCB solutions, and the suspension is fed to the microfluidic device using a syringe pump. The

yeast cells are captured inside the wells by applying AC signal with $2 V_{pp}$ amplitude and 5 MHz frequency for 10 seconds, and the impedance spectrum of cells is measured in 1 kHz – 40 MHz frequency range. Each experiment is repeated three times, and the averaged values are shown in Figure 3.7. Figures 3.A2a and 3.A2b show the normalized standard deviation of the impedance magnitude and the phase angle.

The normalized standard deviation in all cases is less than 1% in a significant range of the frequency spectrum. Figure 3.7a shows the impedance magnitude and phase angle variation as a function of frequency for both 0.05 S/m LCB and yeast cells suspended in 0.05 S/m LCB. The figure illustrates that introducing the cells will increase the impedance value at low frequencies, where the cell membrane effectively insulates the cytoplasm, and the current can only flow around the cells. As a result, the presence of cells adds extra resistance to the current flow and increases impedance. As the frequency increases, the cell membrane becomes more permeable to AC electric field, and current flow through the cell starts to depend on the ratio of the complex conductivity of the cytoplasm to that of the bulk solution. Finally, the interfacial polarization happens, and the AC current across the cell membranes increases. Since the cytoplasm conductivity is higher than the medium conductivity, the presence of cells decreases the impedance at higher frequencies. Based on phase angle graphs, the presence of cells increases the absolute value of phase angle at lower frequencies because cell membrane acts as an insulator, and the system is more capacitive. However, at higher frequencies, the cell membrane becomes permeable to electric currents, and the system is more resistive, which means a decrease in the absolute value of the phase angle. Figures 3.7b and 3.7c illustrate the impedance magnitude and phase angle variation as a function of frequency for yeast cells suspended in 0.01, 0.05,

and 0.20 S/m LCB solution. Figures 3.7b and 3.7c show that increasing conductivity decreases impedance and phase angle value, and the system becomes less resistive.

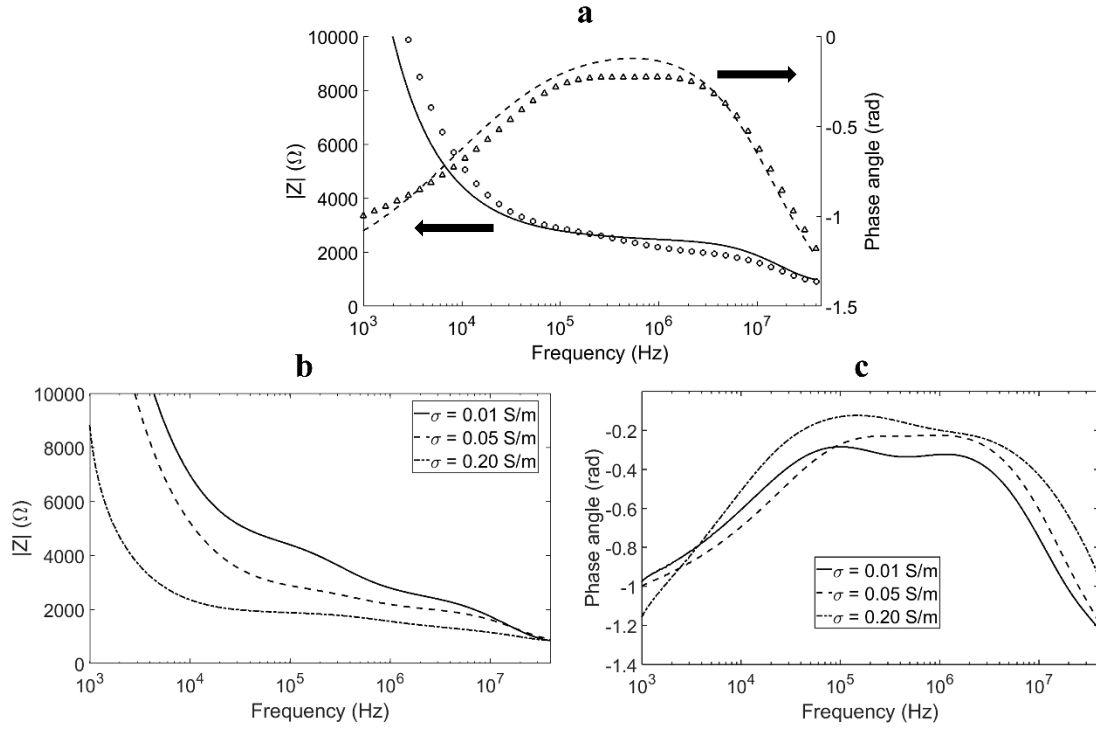


Figure 3.7 a) Experimentally measured impedance spectrum of microchip device for pure LCB and yeast suspended in 0.05 S/m LCB. Lines show the results for pure LCB while symbols show yeast suspended LCB. b) Experimentally measured impedance value and c) phase angle for yeast cells suspended in 0.01, 0.05, and 0.2 S/m LCB.

Simulations are performed in the 1 kHz-40 MHz frequency range, and the impedance spectra are calculated. It should be noted that the real device consists of 441 identical wells that can be considered as parallel elements. As a result, the computational impedance is

divided by 441 to be compared with experimental results. Figures 3.8a and 3.8b depict the experimental and numerical impedance spectra for both LCB and yeast suspended in LCB at 0.05 S/m conductivity. Comparisons between numerical and experimental results show good qualitative agreements with less than 10% error in the 100 kHz – 20 MHz range, where the interfacial dispersion occurs. The discrepancy in the lower frequency region is mainly due to the electrode polarization (EP) effects in the experiments, which dominates the system and is not considered in the simulations. EP happens due to charge accumulation at the electrode/electrolyte interface, causing significant potential drop and the formation of a high impedance at the interface [77]. The discrepancy in the higher frequency region mainly arises from the experimental inductance effects at frequencies above 20 MHz. Another critical point here is the presence of two distinct impedance changes observed in Figure 8b. The first impedance change ($\sim 10^5 - 10^6$ Hz) is due to the cell membrane polarization at moderate frequencies and the second one ($\sim 4 \times 10^6 - 4 \times 10^7$ Hz) is related to medium-SU8 interfacial dispersion.

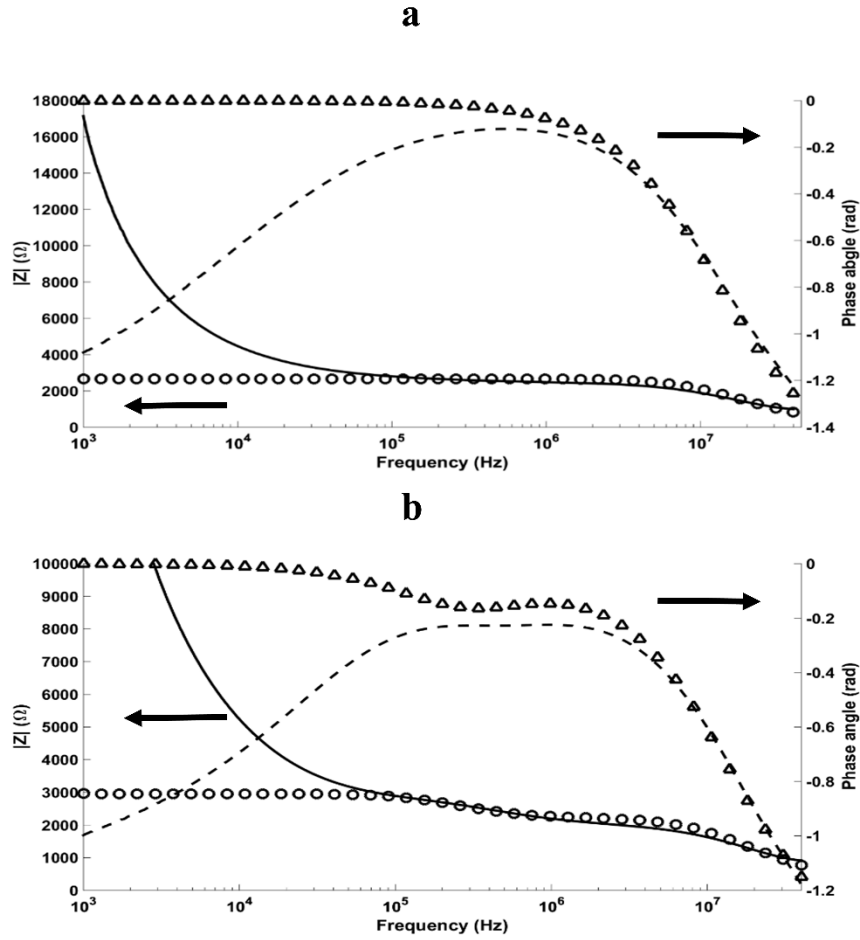


Figure 3.8 Comparison between numerical and experimental Impedance data (magnitude and phase angle) for a) pure LCB solution (0.05 S/m), and b) yeast cells suspended in LCB. Solid and dashed lines represent experimental impedance magnitude and phase angle results, while circles and triangles show numerical impedance magnitude and phase angle values.

3.3. Conclusion

In this chapter, we fabricated and tested a fully integrated microfluidic device consisting of electroactive micro-well arrays for capturing biological cells and measuring the impedance spectrum of trapped cell suspension. Transparent nature of 25 nm thick gold electrodes enables monitoring biological cells using an optical microscope. DEP response of yeast cells was predicted by calculating the real part of the Clausius-Mossotti factor using a previously established method. Fast loading and unloading of yeast cells were observed using positive and negative DEP. The effect of cells on the impedance spectrum was experimentally studied. Moreover, numerical impedance results have shown good agreement with the experimental data, for the high frequency range.

Experimental data show the capability of the microfluidic device in measuring the dielectric spectrum of biological cells. This device could potentially be used to extract sub-cellular properties of biological cells. Since the cells are stably trapped inside the micro-wells, external stimuli could be altered at will, and the cell responses can be measured in real time. Furthermore, cell unloading capability of the device enables measurements of different batches of cells. Future work will focus on developing analytical and numerical methods to relate the sub-cellular dielectric properties with impedance spectrum, and how the changes in external stimuli affect sub-cellular properties. This requires the development of a reliable equivalent circuit model for the device.

3.4. Appendix

3.4.1. Procedure for extracting electrode polarization effect in parallel plate electrodes:

Unit capacitance (C_0) and stray capacitance (C_f) are measured using the impedance of the microfluidic chamber filled with air and DI water. The details of the microfluidic chamber are given in a previous study [10]. The unit and stray capacitances are, respectively:

$$C_0 = \left(\frac{1}{Z_{DI}} - \frac{1}{Z_{air}} \right) / 79\omega \quad (3.A1)$$

$$C_f = \left(\frac{1}{Z_{DI}} - j\omega C_0(1 \text{ MHz}) \right) / \omega \quad (3.A2)$$

where Z_{DI} and Z_{air} correspond to the impedance of the chamber filled with DI and air, respectively.

The chamber was filled with a yeast cell suspension of known volume fraction, and the impedance is measured in between 1 kHz to 40 MHz to obtain the CM factor. The measured impedance consists of the cell suspension impedance and the electrode polarization effect. The electrode polarization effect was modeled using a constant phase element (CPE) model.

$$Z_{tot} = Z_{sus} + \frac{K^{-1}}{(j\omega)^\alpha} \quad (3.A3)$$

where K and α are the CPE model constants. The complex permittivity of the suspension is calculated as:

$$\varepsilon_{sus}^* = \frac{\left(\frac{1}{Z_{sus}} - j\omega C_f\right)}{j\omega C_o} = \frac{\left(\left(Z_{tot} - \frac{K^{-1}}{(j\omega)^\alpha}\right)^{-1} - j\omega C_f\right)}{j\omega C_o} \quad (3.A4)$$

Based on the Cole-Cole model, the suspension complex permittivity is written as:

$$\varepsilon_{sus}^* = \varepsilon'_\infty + \frac{\varepsilon'_s - \varepsilon'_\infty}{1 + (i\omega\tau_{rel})^\beta} - i\sigma/\omega\varepsilon_o \quad (3.A5)$$

where ε'_s and ε'_∞ are the low and high frequency limit of the suspension permittivity, σ and τ_{rel} are the effective suspension conductivity and dielectric relaxation time constant, and β is the exponent parameter of the Cole-Cole equation that varies between 0 and 1. The fitting procedure varied the values of the parameters (K , α , ε'_s , ε'_∞ , τ_{rel} , σ , and β) until the difference between the measured suspension complex permittivity and Cole-Cole model is minimized. The values of K and α are used to extract the electrode polarization effect and find out Z_{sus} and ε_{sus}^* .

3.4.2. Procedure for extracting sub-cellular properties using Maxwell-Wagner and single shell model

In this study, we used a single shell model for yeast cells, which is a reasonable assumption, since the cell wall has nearly the same conductivity and dielectric constant as those of the suspending medium for our conductivity range. Based on Asami [49], for KCl suspensions

with KCl concentrations ranging 1mM-80mM, which corresponds to ~0.01-1.3 S/m, a single shell model is appropriate. Based on the single shell model, the complex permittivity of a yeast cell is a function of cytoplasmic and membrane electrical properties, and the cell geometry. The complex permittivity of the cell is given by Equation 2.40:

$$\varepsilon_c^* = \varepsilon_{mem}^* \frac{\gamma^3 + 2 \left(\frac{\varepsilon_{cyt}^* - \varepsilon_{mem}^*}{\varepsilon_{cyt}^* + 2\varepsilon_{mem}^*} \right)}{\gamma^3 - \left(\frac{\varepsilon_{cyt}^* - \varepsilon_{mem}^*}{\varepsilon_{cyt}^* + 2\varepsilon_{mem}^*} \right)} \quad (2.40)$$

Based on the Maxwell-Wagner model, the cell suspension complex permittivity is given by Equation 2.35:

$$\frac{\varepsilon^* - \varepsilon_m^*}{\varepsilon^* + 2\varepsilon_m^*} = \Phi \frac{\varepsilon^* - \varepsilon_p^*}{\varepsilon^* + 2\varepsilon_p^*} \quad (2.35)$$

The fitting procedure varied the values of the parameters (σ_{med} , σ_{mem} , ε_{mem} , σ_{cyt}) until the difference between measured and fitted suspension complex permittivity is minimized. It should be noted here that the values for medium and cytoplasm permittivity were fixed at 80 and 60, respectively [82].

3.4.3. Grid Refinement Study

To ensure convergence of the numerical solution, five different grid resolutions were considered, and the variation of impedance magnitude at $f = 1$ MHz with the number of grid elements is shown in Figure 3.A1. This figure shows that by increasing the number of

elements, impedance value decreases and finally becomes constant when the number of the elements reaches 100,000. As a result, around 100,000 elements were used for simulations.

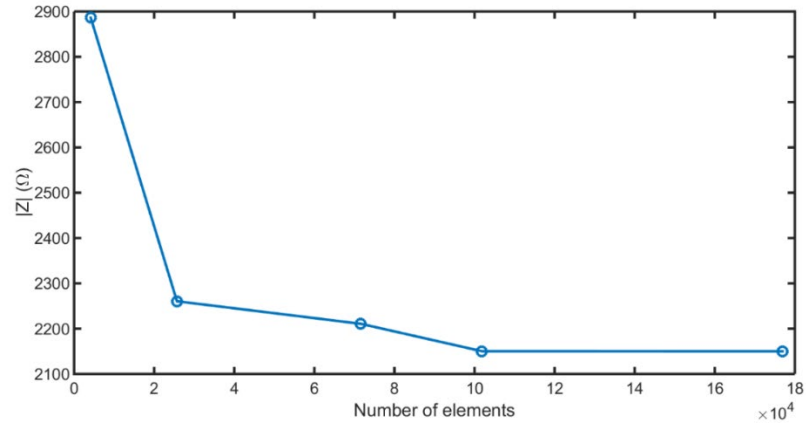


Figure 3.A1 Variation of impedance value with the number of computational elements

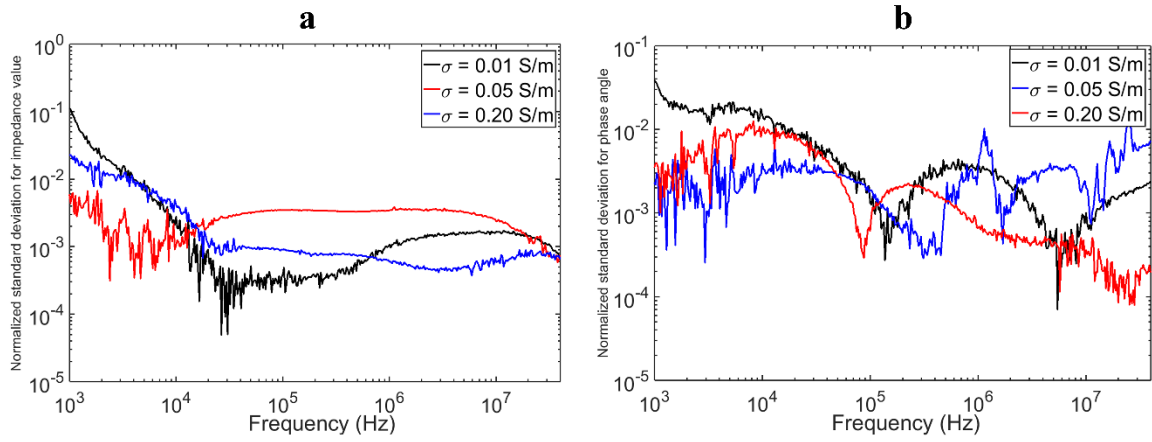


Figure 3.A2 The normalized standard deviation (standard deviation divided by mean) of a) impedance magnitude, and b) phase angle for yeast cells suspended in 0.01, 0.05, and 0.20 S/m LCB solution.

Chapter 4

ON-CHIP ELECTRICAL IMPEDANCE MEASUREMENTS OF BIOLOGICAL CELLS IN RESPONSE TO EXTERNAL STIMULI

Dielectric spectroscopy (DS) is a non-invasive technique for real-time measurements of the impedance spectra of biological cells. DS enables characterization of cellular dielectric properties such as membrane capacitance and cytoplasmic conductivity. We have developed a lab-on-a-chip device that uses an electro-activated micro-wells array for capturing, making DS measurements of, and unloading of biological cells. In chapter 3, it was shown that the device could load, unload, and measure yeast cells. However, each well may contain up to 60-70 cells, but the exact well loading and volume fractions are unknown. In this chapter, we targeted characterization of mammalian cells, which has a bigger size than yeast cells and can individually fill up single wells. Impedance measurements were conducted at 0.2 V in 10 kHz - 40 MHz range with six-seconds time resolution. An equivalent circuit model was developed to extract the cell membrane capacitance and cell cytoplasmic conductivity from the impedance spectra. A human prostate cancer cell line, PC-3, was used to evaluate the device performance. Suspension of PC-3 cells in low conductivity buffers (LCB) enhanced their dielectrophoretic trapping and impedance response. We report the time course of the variations in dielectric properties of PC-3 cells suspended in LCB and their response to sudden pH change from a pH of 7.3 to a pH of 5.8. Importantly, we demonstrate that our device enabled real-time measurements of dielectric properties of live cancer cells, and allowed the assessment of

the cellular response to variations in buffer conductivity and pH. These data support further development of this device towards single-cell measurements.

4.1. Materials and Methods

4.1.1. Chip Fabrication

Photolithography supplies (photoresists, developers, and remover) were purchased from Microchem Corp. (Westborough, MA, USA). All other chemicals used were of analytical grade and obtained from Sigma-Aldrich (St Louis, MO, USA). All solutions were prepared with 18 M Ω ·cm ultrapure water obtained from Millipore Alpha-Q water system (Bedford, MA, USA). Glass slides were cleaned using the same protocol as in Chapter 3. The electrode structures were fabricated using lift-off photolithography method, and micro-wells were created using negative photoresist SU8. The microfluidic channel was made up of double-sided tape. The fluidic ports were drilled by a diamond drill bit, and the copper tape was used for electrical connections. To assemble the device, the electrode pair was aligned using Karl SUSS MJB3 mask aligner. Finally, they were clamped and put in a convection oven at 75°C to enhance adhesion between the slides.

A top view of three main layers of the microfluidic device is shown in Figure 4.1a. The bottom layer is a 1×1 mm square shape gold electrode on a glass slide and covered with negative SU8 photoresist except for 30×30×30 μ m features as the micro-wells and the electrical connection port. The geometry is the same as used in previous chapters. Figure 1a shows the top view of different layers and side view of the assembled microfluidic device along with relevant device dimensions.

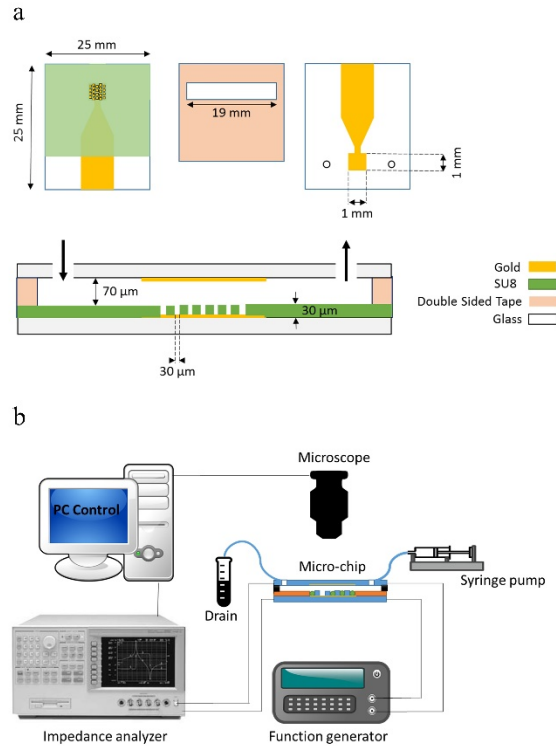


Figure 4.1 a) Top view of the microfluidic device layers and side view of the assembled device; b) Schematics of the experimental setup.

4.1.2. Experimental setup

The experimental setup is shown in Figure 4.1b. A syringe pump (New Era Pump System Inc., NE4000) delivers the cell suspension to the inlet of the microfluidic device, and the outlet was collected in a drain. The suspension contains PC-3 cells at a concentration of 10^5 cells/mL, and the flow rate was fixed at 1 mL/hr. The electrodes were excited using a function generator (Tektronix AFG3102) to provide sinusoidal AC electric fields at desired amplitudes and frequencies for cell capture and release purposes. The cells were captured

inside the micro-wells by applying $2 V_{pp}$ at a predetermined frequency to induce DEP response that pulls them into the micro-wells. After the cells were captured, the rest of the cell suspension inside microchannel is washed with LCB towards the drain via a polyvinyl chloride (PVC) tube. Then, the microfluidic device was connected to the impedance analyzer to record the impedance spectrum. A high precision impedance analyzer (HP Agilent 4194A) was used for impedance measurement in the 10 kHz - 40 MHz frequency range. Using a medium integration time setting (i.e., the period over which the analyzer measures the input signal), each impedance measurement sweep takes six seconds for 401 discrete, logarithmically spaced frequencies. The output data of impedance analyzer was transferred to a PC using a General-Purpose Interface Bus (GPIB) cable, and then the data were processed using Matlab (R2014b) software. A CCD camera (Hamamatsu Orca, C11440) connected to an inverted microscope (Olympus IX81) was used for cell visualization, and images were recorded through an imaging software (CellSens). Once the DS measurements were over (~ 6 s), the device was reconnected to the function generator, and the cells were released from the micro-wells by applying $2 V_{pp}$ at a predetermined frequency to induce DEP response that pushes them out of the micro-wells (~ 10 s). The released cells were washed to the drain by simultaneously applying pressure driven flow using the syringe pump.

4.1.3. Cell Preparation and Viability Test

PC-3 cells were attained from the American Type Culture Collection (ATCC). The PC-3 cells were cultured in RPMI (Roswell Park Memorial Institute) 1640 growth medium

(Sigma Aldrich). RPMI growth medium was supplemented with 10% fetal bovine serum, with penicillin (100 IU/ml) and streptomycin (100 µg/ml) [83]. Cells were grown in an incubator (Thermo Scientific) at 37°C with 5% CO₂ atmosphere. For subculture, the cells were washed with PBS and incubated with 0.05% trypsin-EDTA solution (Sigma Aldrich) for 10 min with the same conditions to detach the cells from a petri dish. The growth medium was then added to inhibit the effect of trypsin and cells were centrifuged for 5 minutes at 1000 rpm and re-suspended in a LCB solution for DS measurements or DEP experiments. The harvested cells were spheroidal and 22.0 ± 4 µm in diameter. LCB is the most commonly used medium for DEP-based particle trapping, manipulation, or separation. It is a mixture of isotonic sucrose/dextrose solution and a small amount of salts. Cells were suspended in an LCB solution containing 229 mM sucrose, 16 mM glucose, 1µM CaCl₂, and 5 mM Na₂HPO₄ in type 1 DI water (pH 7.3) for experiments after washing with isotonic buffer. The conductivity of LCB was adjusted by adding PBS and measured using a conductivity meter (Con11, Oakton). The pH value of the LCB solution was adjusted by adding sodium phosphate mono/dibasic solution, and pH was measured using a pH meter (Orion Versastar, Thermo Scientific).

The Trypan Blue exclusion test was used to determine the viability of cells in LCB. After adding PC-3 cells to LCB, the resulting cell sample was diluted in Trypan Blue dye of an acid azo exclusion medium by preparing a 1:1 dilution with a 0.4% Trypan Blue solution (Sigma Aldrich). After that, a hemocytometer was filled with the suspension and incubated for 1 minute. Because of cell membrane selectivity, Trypan Blue was not absorbed through a viable cell membrane, while it passes through the dead cells membranes and makes them have a distinctive blue color under the microscope. After loading with cells, the

hemocytometer was placed under the inverted microscope stage, and images were recorded using the CCD camera. Finally, the images were analyzed with ImageJ [84] software and cell viability was determined.

4.1.4. Equivalent Circuit Modeling

Electrodes in contact with an electrolyte experience Electrode Polarization (EP) effects due to the shielding of the applied electrode potential by the mobile counterions in the electrolyte [85]. This undesirable effect becomes dominant in high conductivity media and affects impedance measurements typically at 0-100 kHz range. It is common to theoretically model the EP effect with double layer capacitance in series with the whole system [86]. For practical applications, the constant phase element (CPE) model predicts the non-ideal behavior of the EP more precisely and effectively [85]. CPE impedance model is defined as [87]:

$$Z_{CPE} = \frac{1}{K(j\omega)^\alpha} \quad (4.1)$$

where K and α are the CPE coefficient and exponent, respectively. The parameter α changes from zero to one corresponding to purely resistive and capacitive interfacial impedance, respectively. For our microfluidic device, the equivalent circuit model depicted in Figure 4.2a-b is proposed for filled and empty wells.

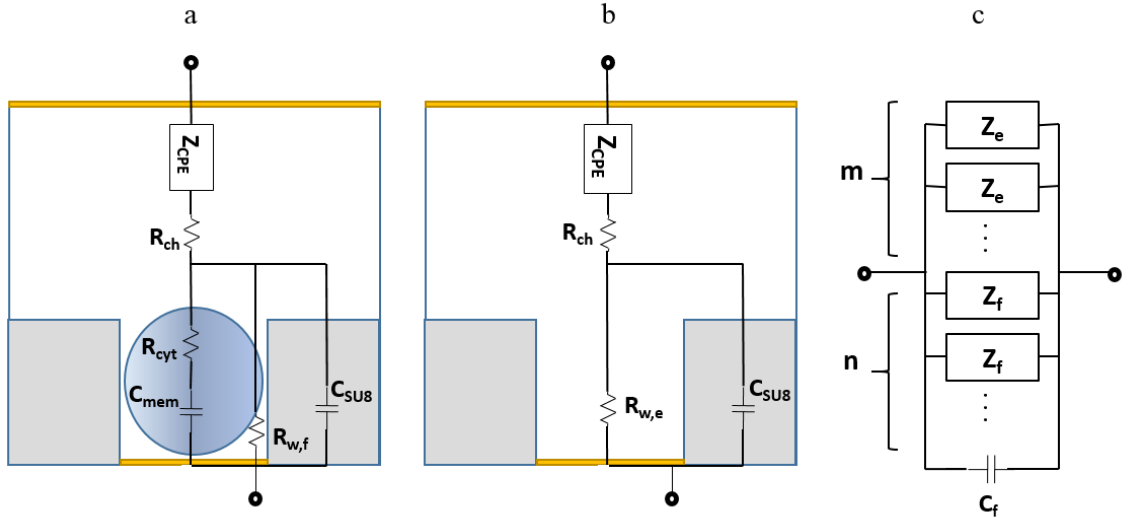


Figure 4.2 Proposed equivalent circuit model for a) filled and b) empty micro-wells. c) The equivalent circuit model for the microfluidic device.

The current between two electrodes has at most three different paths. It can flow through the SU8 part, the solution inside the micro-well, and through the trapped cell for the case of filled wells. These three paths are modeled as SU8 capacitance (C_{SU8}), the micro-well solution resistance for empty and filled cases ($R_{w,e}$ and $R_{w,f}$), and cytoplasmic resistance (R_{cyt}) in series with membrane capacitance (C_{mem}) as the cell model, respectively. Outside the micro-well, the electric current flows through the solution inside the microchannel which can be represented as a resistor (R_{ch}). In both filled and empty micro-wells, the EP effect is modelled as a CPE element (Z_{CPE}) in series with the circuit. The impedance of empty (Z_e) and filled (Z_f) micro-wells are calculated as:

$$Z_e = Z_{CPE} + R_{ch} + \frac{1}{\frac{1}{R_{w,e}} + j\omega C_{SU8}} \quad (4.2)$$

$$Z_f = Z_{CPE} + R_{ch} + \frac{1}{\frac{1}{R_{w,f}} + j\omega C_{SU8} + \frac{1}{\left(R_{cyt} + \frac{1}{j\omega C_{mem}}\right)}} \quad (4.3)$$

Electric current inside the SU8 is assumed uniform, and the following analytical formulation is used to calculate the SU8 capacitance:

$$C_{SU8} = \varepsilon_{r,SU8} \varepsilon_0 \frac{A_{SU8}}{t} \quad (4.4)$$

where $\varepsilon_{r,SU8}$ is relative permittivity of SU8 material ($\varepsilon_r = 3.2$), A_{SU8} is the SU8 surface area, and t is the SU8 thickness. After application of pDEP for cell capture, n_f number of micro-wells will be filled with cells and n_e wells will be empty. Each micro-well is considered as a parallel element with the rest and a parasitic capacitance (C_f), as shown in Figure 4.2c, is parallel to the whole system. The total impedance of the proposed equivalent circuit is calculated as follows:

$$Z_{tot} = \frac{1}{\frac{n_f}{Z_f} + \frac{n_e}{Z_e} + j\omega C_f} \quad (4.5)$$

To find the individual electrical components, real and imaginary parts of the experimental results are fitted into the real and imaginary parts of the proposed equivalent circuit model using a non-linear least square method. The fitting criterion is finding a minimum to the sum of squares of the following matrix by employing the Marquardt-Levenberg algorithm as previously shown [79]:

$$\Delta = [\Delta_{r,f_1}, \dots, \Delta_{r,f_n}, \Delta_{i,f_1}, \dots, \Delta_{i,f_n}] \quad (4.6)$$

where Δ_{r,f_j} and Δ_{i,f_j} are defined as:

$$\Delta_{r,f_j} = 1 - \left| \frac{\text{real}(Z_{m,j})}{\text{real}(Z_{fit,j})} \right|, \quad \Delta_{i,f_j} = 1 - \left| \frac{\text{imag}(Z_{m,j})}{\text{imag}(Z_{fit,j})} \right| \quad (4.7)$$

In the above equations, subscripts m and fit denote the measured and fitted data, respectively. This fit will yield CPE parameters (K and α), R_{ch} , $R_{w,f}$, $R_{w,e}$, C_f , and cell parameters (C_{mem} and R_{cyt}). n_e and n_f are determined by the microscopy image of the trapped cells. For consistency, 10 random sets of initial conditions were employed in the optimization algorithm. A solution is considered correct only if the results from multiple initial conditions converge to a single global solution set. Finally, the average values are reported.

4.2. Results and Discussion

4.2.1. DEP Response Prediction

In this study, the optimum pDEP and nDEP frequencies required for loading and unloading the micro-wells with PC-3 cells were determined by measuring the dielectric properties of PC-3 cells in a microfluidic device with parallel plate electrode configuration [79], which provided the $Re[CM]$ for PC-3 cell suspensions in LCB, as previously described [79]. Impedance measurements of suspension were repeated 5 times for each 10 minute period and the averaged data was reported. Fig. 4.3a shows the time-averaged $Re[K]$ for PC-3 cells measured in 1 kHz - 10 MHz frequency range at different time periods. The results revealed that the f_c of PC-3 cells increased with time. The PC-3 cells showed the pDEP response for an hour at frequencies above 100 kHz, with an f_c around 40 kHz at the

beginning (0-10min) of the measurement period, and an f_c of 100 kHz after incubation in LCB for 60 minutes. Cancer cells are known to go under time-dependent cytoplasmic and membrane re-modelling through the shedding of cytoplasm in LCB [88]. Since the conductivity of cell decreases in LCB because of ion leakage, the $Re[K]$ became more negative and f_c shifts to higher frequencies, consistent with published studies [89]. According to the DS measurements with parallel plate electrodes, 5 MHz was chosen to trap the cells in the wells, because it yielded the highest CM factor and consequently the largest pDEP force for a given electric field magnitude. The device was energized at 20 kHz for unloading. The applied voltage was kept at 2 Vpp (peak to peak voltage) to reduce the effects of Faradaic reactions, Joule heating, and electroporation [90-92].

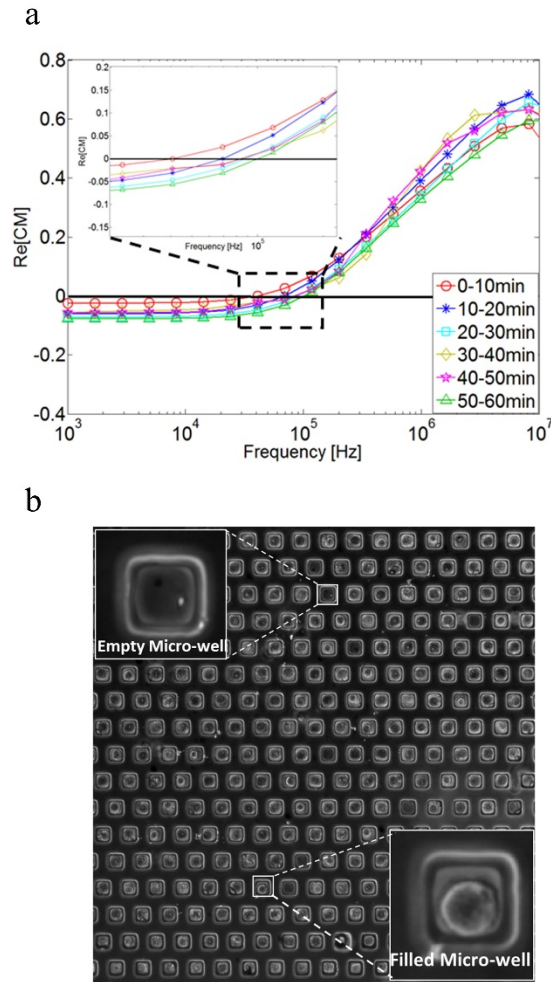


Figure 4.3 a) The real part of CM factor for PC-3 cells suspended in LCB at various times
 b) captured PC-3 cells after 20s of pDEP application at 2 Vpp and 5 MHz frequency. The inset shows a sample of individual empty and filled micro-wells.

4.2.2. DS Measurements

PC-3 cells with a concentration of 10^5 cells/mL were introduced into the microfluidic device at 1 mL/hr flow rate. The conductivity and pH of the external medium was 0.05 S/m

and 7.3, respectively. To trap the cells using pDEP, AC voltage of 5 MHz with 2 V_{pp} amplitude was applied between the top and bottom electrodes. Once the majority of the wells were filled with PC-3 cells, the function generator was turned off, and the floating cells were washed with a continuous flow of LCB solution by increasing the flow rate (5 mL/hr). By using pDEP, 96% of wells were successfully filled with single PC-3 cells in less than 20 seconds. Figure 4.3b shows a picture of the trapped cells in the wells, as well as a zoomed view of empty and filled individual micro-wells. Subsequently, the impedance of the cell suspension was measured in the 10 kHz - 40 MHz frequency range. In the next step, the recorded impedance data were fitted to the equivalent circuit model using MATLAB software. One representative example of the raw experimental data that fit with the proposed equivalent circuit model is shown in Fig 4.4. Figures 4.4a and 4.4b represent the experimental and fitted impedance values and phase angles of PC-3 cell suspension in LCB with pH of 7.3 in 10 kHz - 40 MHz frequency range, obtained five minutes after the cell suspension process. We found that the impedance spectrum of the circuit model exhibited a similar trend with the experimental data, validating the proposed equivalent circuit model. Small discrepancies between the model and experimental data were due to EP impedance that dominates the impedance data in the low-frequency spectrum.

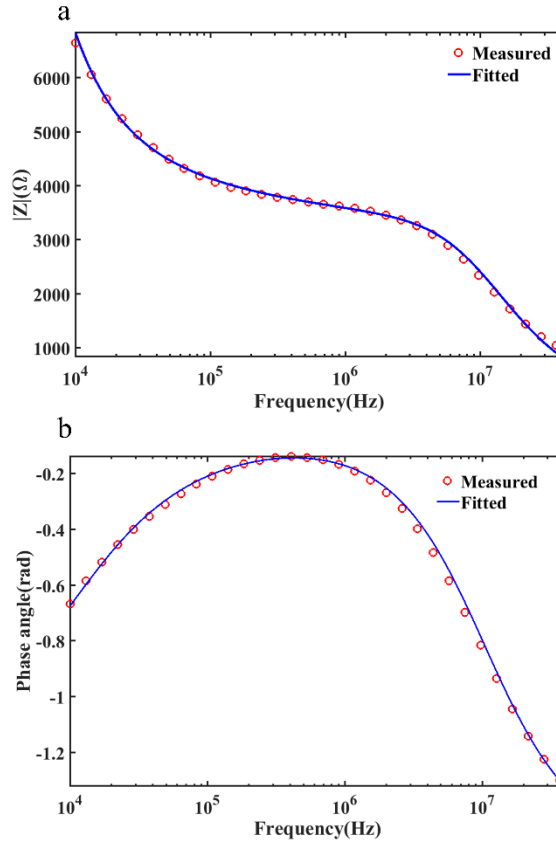


Figure 4.4 Experimental and fitted a) impedance value and b) phase angle of the PC-3 cell suspension in LCB with pH=7.3 in the 10 kHz - 40 MHz frequency range obtained five minutes after the suspension of PC3 cells within LCB.

Furthermore, the sensitivity of the impedance to each element in the equivalent circuit is calculated and plotted in Figure 4.5. The sensitivity is defined as $\frac{\partial |Z|}{\partial X}$, where x is the element in the equivalent circuit model. Sensitivity results show that each element has a relatively high sensitivity in a specific frequency region and this proves the importance of all the elements considered in the model.

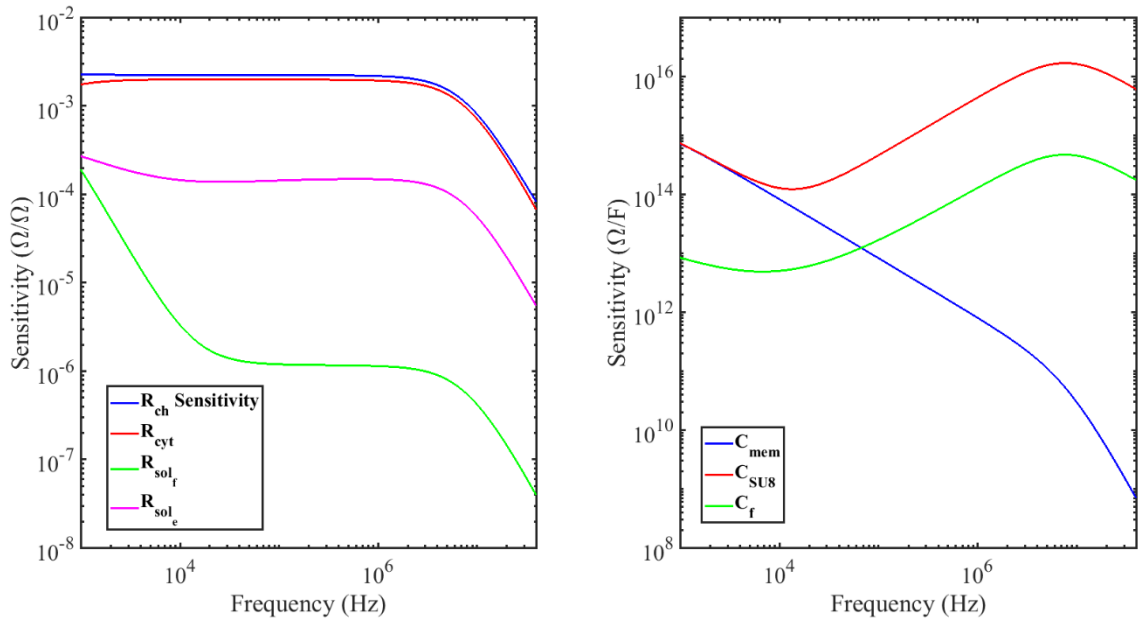


Figure 4.5 Impedance sensitivity to the equivalent circuit model elements

4.2.3. PC-3 Cells Response to LCB Suspension

To observe how PC-3 cells respond to suspension in LCB, their impedance spectrum at LCB with a pH of 7.3 was measured for two hours with a six-second resolution. Each impedance spectrum was fitted to the equivalent circuit model and cell parameters (C_{mem} and R_{cyt}) extracted. Figure 4.6 shows the changes in membrane capacitance and cytoplasmic resistance after PC-3 cells suspended in LCB. This figure showed that cell membrane capacitance decreased drastically after mixing PC-3 cells with LCB and it reached a steady state within an hour. The decrease in membrane capacitance was attributed to the cell cytoskeletal tension, which caused the cells to round up into a pseudo-spherical shape after being released into the suspension. Since, a sphere has the smallest

surface area for any given volume, the membrane capacitance, which is proportional to the membrane surface area, decreased after cell suspension in LCB. Moreover, this figure showed an increase in the cytoplasmic resistance, likely caused by osmotic imbalance generated by efflux of intracellular-ions, and resulting in time dependent increase in cytoplasmic resistance [88].

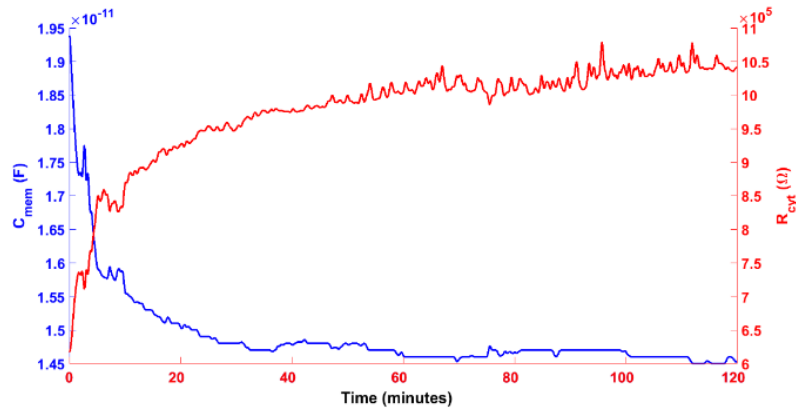


Figure 4.6 Time-dependent variations in the membrane capacitance and cytoplasmic resistance after suspension of PC-3 cells in LCB.

4.2.4. PC-3 Cells Response to pH change

To study how PC-3 cells respond to external pH changes, the PC-3 cells were trapped inside micro-wells using a LCB solution with a pH of 7.3 (normal pH environment). After 1 minute, the external solution was changed to a LCB solution with a pH of 5.8 (acidic environment). Finally, the external pH was reversed to 7.3 after 10 minutes.

Figure 4.7 illustrates the extracted cell membrane and cytoplasmic resistance with changing external pH values. The gray shaded region shows the time that extracellular pH was kept at 5.8. In the first minute of pH change, the cells responded rapidly to the sudden stresses applied with pH changes. This response could be related to cytoskeleton changes and ion transport through cell membrane ion channels and pumps. The remodeling, elongation, shortening, and architectural organization of the actin filaments may be a result of signaling cascades set by environmental cues [93], including changes in conductivity, pH, nutrition, etc. Using a theoretical model, Naumowicz et al. demonstrated the pH dependence of lipid membranes formed by 1:1 a phosphatidylcholine-phosphatidylserine mixture [94]. They concluded that the electrical capacitance of the analyzed bilayer had a minimum value around a pH of 4.2 and increased as the pH decreased or increased. Our data (Figure 4.7) suggested that the PC-3 membrane capacitance was lower with a pH of 5.8 compared with a pH of 7.3, which is consistent with prior studies [94]. Further, for the first time, we have defined a profile of the changes in cell membrane capacitance and cytoplasmic resistance over time. When the pH was reversed at 10 minutes, the membrane capacitance increased, and the cytoplasmic resistance decreased. These changes could be attributed to changes in cytoskeleton remodeling and increased influx of ions. At 14 minutes, the PC-3 cells relaxed, and the changes in membrane capacitance and cytoplasmic resistance were reversed to normal conditions. At 20 minutes, the PC-3 cells reached a new state with lower membrane capacitance and higher cytoplasmic resistance compared to the initial state.

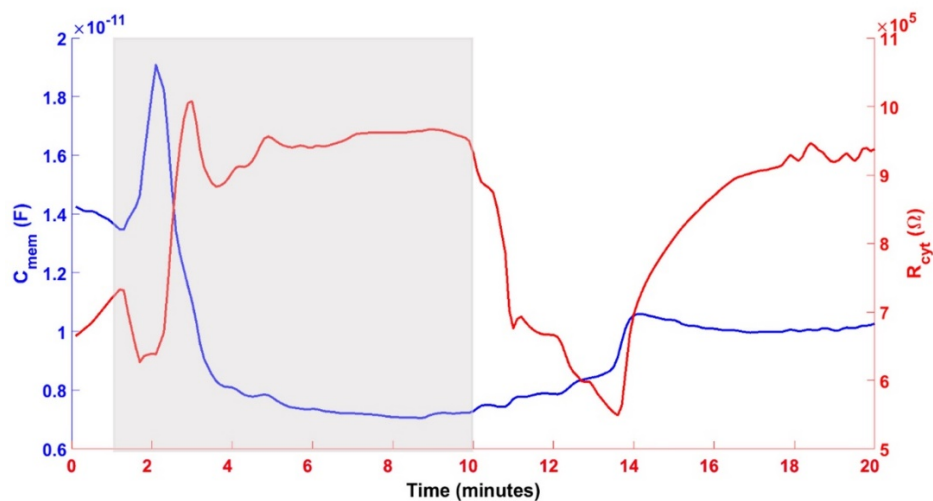


Figure 4.7 Extracted cell membrane and cytoplasmic resistance with changing external pH values. The white region shows pH=7.3 and gray regions indicate pH=5.8.

4.2.5. Viability Tests

To check the cell activity, viability tests were conducted at two different pH values in LCB (pH of 5.8, and 7.3) using the Trypan Blue exclusion method. Figures 4.8a and 4.8b show the viable and dead cells at these two different pH values after 1 hour. Since dead cells are permeable to Trypan Blue dye, they can be distinguished as dark particles in the grayscale figures. Figures 4.8c and 4.8d show the percentile viability of PC-3 cells suspended in LCB for pH of 7.3 and 5.8 over 120 minutes period. Based on these figures, after two hours of suspension of PC-3 cells in LCB, less than 10% of the cells were dead at either pH of 7.3 or 5.8. Moreover, these data confirmed that cancer cell viability decreased in acidic conditions [95]. Viability studies of PC-3 cells in growth medium showed 90-100% viability for 24 hours [96], while the current results in LCB at pH of 7.3 and 5.8 show the

same viability range during the impedance measurements. These findings indicated that the measured dielectric response was driven by live PC-3 cells, which showed the applicability of the lab-on-a-chip device in biomedical and clinical settings.

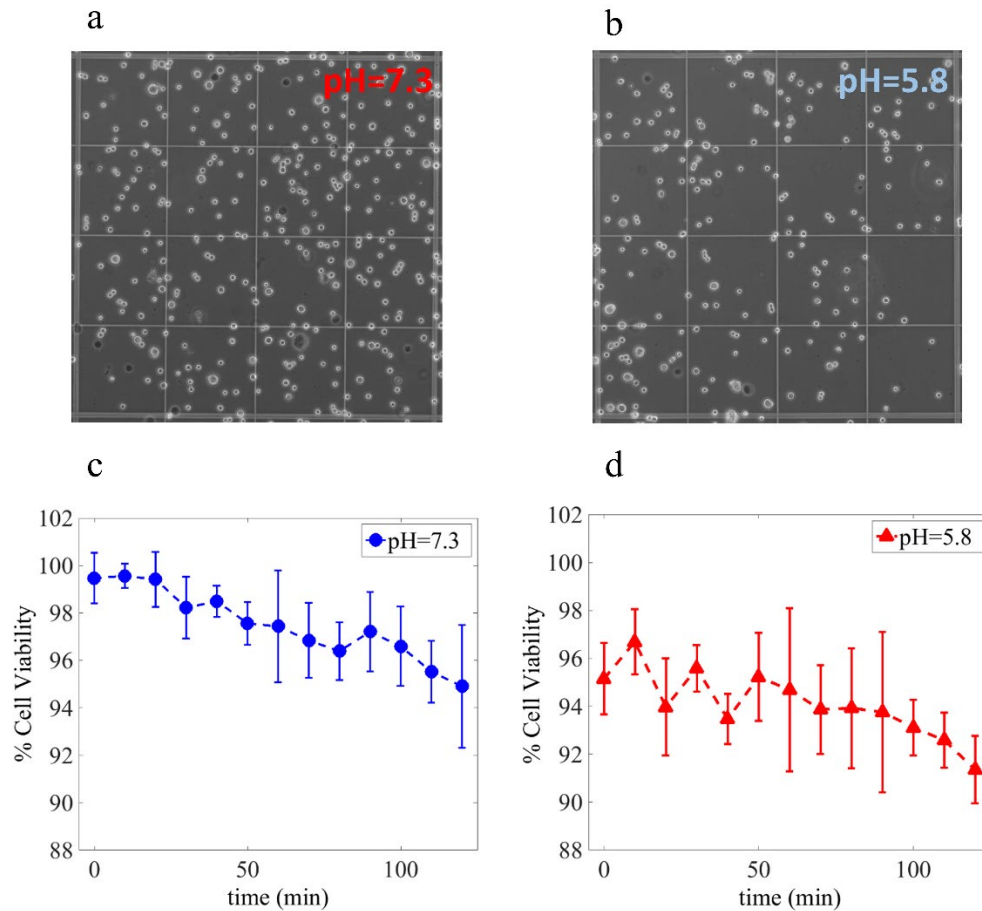


Figure 4.8 Viable and dead PC-3 cells in LCB with a) pH=7.3 and b) pH=5.8 after 1 hour. Percentile viability of PC-3 cells in LCB with c) pH=7.3 and d) pH=5.8.

4.3.Conclusion

In this chapter, we presented a lab-on-a-chip device for real-time measurement of biological cells' response to external stimuli, such as sudden changes in the buffer conductivity and pH. The device captured cells in a micro-well array using pDEP, followed by the DS measurements and a nDEP assisted cell unloading processes. Well dimensions determined the number of cells that can be trapped in each micro-well. We defined the device performance for cancer cells using the PC-3 cell line using 30 μm square wells. PC-3 cells suspended in 0.05 S/m LCB exhibited a time-dependent response, where their membrane capacitance and cytoplasmic resistance decrease and increase by time, respectively. Alterations of the extracellular pH between 7.3 and 5.8, changed cellular dielectric parameters, likely related to the organization of actin filaments and ion flux regulations as a response to pH alterations but not due to changes in cell viability. These data demonstrated the applicability of our microfluidic chip to measure the dielectric properties of live cancer cells with specialized LCB.

Chapter 5

QUANTIFICATION OF CELL DEATH USING AN IMPEDANCE BASED MICROFLUIDIC PLATFORM

Recently, the utilization of the DS method has been suggested in various stages of the drug discovery process due to low sample consumption and fast analysis time. In this chapter, we used a previously developed microfluidic system explained in chapter 4 to confine single PC-3 cells in micro-wells using dielectrophoretic forces and perform the impedance measurements. PC-3 cells are treated with 100 μ M Enzalutamide, and their impedance response is recorded until the cells are dead as predicted with viability tests. Four different approaches are used to analyze the impedance spectrum. Equivalent circuit modeling is used to extract the cell electrical properties as a function of time. Principal component analysis (PCA) is used to quantify cellular response to the drug as a function of time. Single frequency measurements are conducted to observe the cell's response over time. Finally, opacity ratio (OR) is utilized as an additional quantification method. This device is capable of quantitatively measuring drug effects on biological cells and detecting cell death. Moreover, an available technology was tested for drug response, and its advantages and drawbacks were explained. The results show that the proposed microfluidic system has the potential to be used in the early stages of the drug discovery process.

5.1. Materials and Methods

5.1.1. Device Fabrication

The microfluidic chips were fabricated using standard photolithography on glass substrates. The microfabrication process is extensively explained in chapter 3. In summary, after cleaning glass substrates, transparent gold electrodes were fabricated using a lift-off process. Micro-wells were transferred to the electrodes using SU-8 photolithography. Finally, inlet, outlet, and electrical ports were attached, and the slides were aligned. The only difference here is that micro-well geometry was changed from cubic to cylindrical. As a result, the sharp corners that may induce extra charge concentrations were eliminated. Figure 5.1a shows a side view of the device. Figure 5.1b is the schematic of the experimental setup with a syringe pump for providing the cell suspension and a function generator/impedance analyzer for cell capture/impedance measurements. Figures 5.1c and 5.1d illustrate the Scanning Electron Microscopy (SEM) images of the micro-wells array and a single micro-well. There exist 576 micro-wells with 30 μm diameter and 15 μm separation distance between well edges.

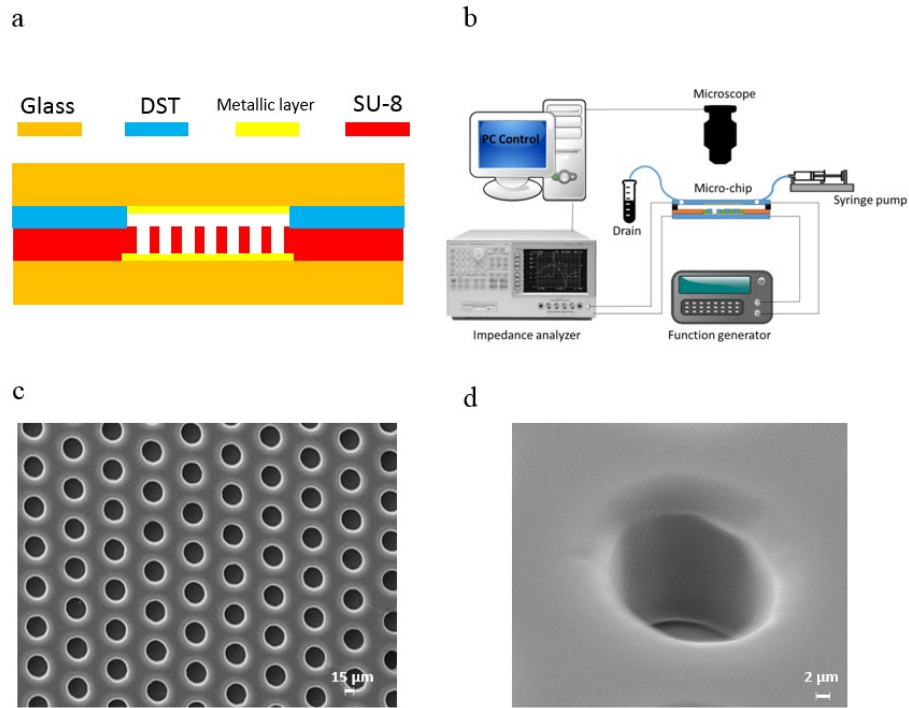


Figure 5.1 a) Side view of the microfluidic device, b) experimental setup, c) SEM image of the micro-wells array, and d) SEM image of an individual micro-well.

5.1.3. Cell Preparation

PC-3 cells were obtained from the American Type Culture Collection (ATCC), which were extracted from a 62-year-old Caucasian male. The cell line is cultured in RPMI 1640 growth medium (Sigma Aldrich) supplemented with 5% fetal bovine serum (FBS), penicillin (100 IU/ml), and streptomycin (100 μ g/ml). Cells are grown in an incubator (Thermo Scientific) at 37°C with 5% CO₂ atmosphere. Figure 5.2 shows snapshots of PC-3 cell culture during the three days. The harvested cells were spheroidal and $22.0 \pm 4 \mu$ m. Figure 5.3 show snapshots of filled and empty micro-wells.

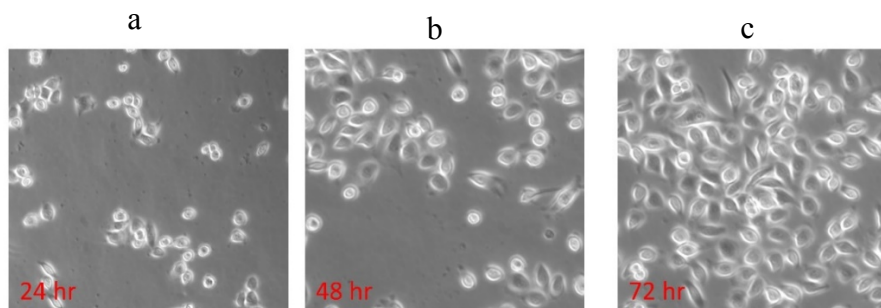


Figure 5.2 Snapshots of PC-3 cell culture after a) 24 hours, b) 48 hours, and c) 72 hours.

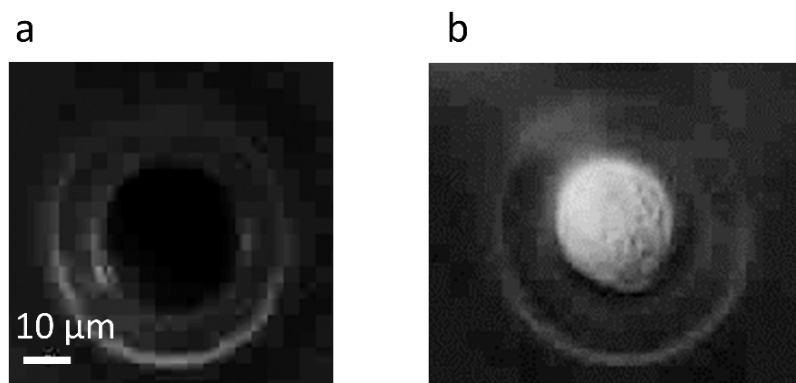


Figure 5.3 Microscopy images of a) empty and b) filled micro-wells.

After about 90% of the petri dish area was covered with cells in 72 hours, the growth medium was extracted, and cells were washed with 1X PBS, and TrypLE was added to detach the cells from the surface. TrypLE is a direct replacement for trypsin with high specificity and low damage to the cells. After incubating the cells with TrypLE for 5

minutes, the complete growth medium was added, and the suspension was transferred to centrifuge tubes. The cell suspension was centrifuged at 1000 rpm for 5 minutes, and the supernatant was extracted, and the fresh medium was added. The final solution was transferred to a petri dish to be cultured inside the incubator. For DEP experiments and DS measurements, cells were suspended in low conductivity buffer (LCB) solution containing 229 mM sucrose, 16 mM glucose, and 1 μ M CaCl₂ in DI water. The solution pH was adjusted to 7.3 by adding sodium phosphate mono/dibasic (NaH₂PO₄/Na₂HPO₄) solution. For viability tests, the Trypan Blue extraction test was performed using a 1:1 dilution with 0.4% Trypan Blue Solution.

5.1.4. Principal Component Analysis

Principal component analysis (PCA) is a statistical method for reduction of a large set of variables into a smaller set with preserving as much of the variance in the data. Other names used for this reduction method are proper orthogonal decomposition (POD) and singular value decomposition (SVD). This method is probably the most popular dimension-reduction method in all scientific fields. The data table consists of I rows and J columns representing the observations and variables to be analyzed by PCA. More information of how PCA works is given in the appendix. The data table consists of rows having the impedance value spectrum at each 30 second time interval for 8 hours.

5.2. Results and Discussion

A conventional parallel plate configuration is used to extract $\text{Re}(K)$ of PC-3 cells suspended in LCB. The method to extract this parameter has been extensively explained in our previous study [79]. Figure 5.4 shows the extracted $\text{Re}(K)$ for PC-3 cells suspended in LCB. The frequency at which $\text{Re}(K)$ changes sign is referred to as the cross over frequency (f_c), which is about 40 kHz for the PC-3 cells. According to the DS measurements, 5 MHz was chosen to trap the PC-3 cells inside the micro-wells, since this frequency yields the highest positive value for $\text{Re}(K)$.

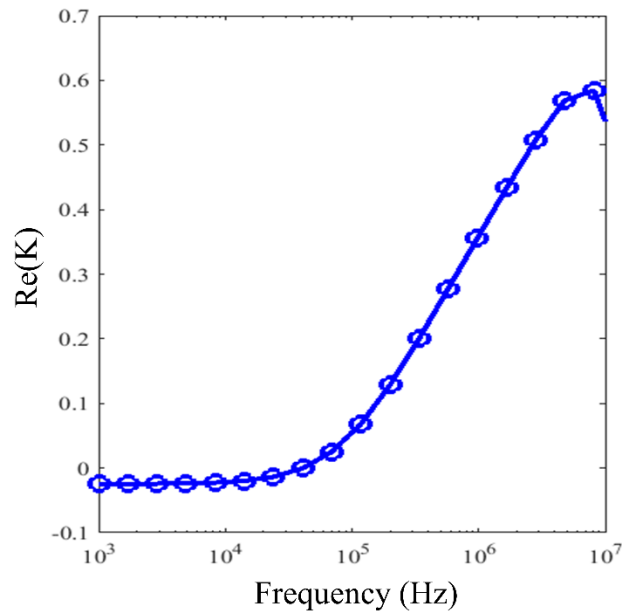


Figure 5.4 $\text{Re}(K)$ of PC-3 cells suspended in LCB

5.2.1. Viability Test

The Trypan Blue extraction test was used to calculate the viability of PC-3 cells exposed to 100 μM Enzalutamide. PC-3 cells are androgen independent, and Enzalutamide at low concentrations cannot cause fast damages to the cell [97, 98]. That is the reason we used a high drug concentration so that the changes can be observed in several hours. Figure 5.5 represents the percentile viability of PC-3 cells suspended in a LCB and 100 μM Enzalutamide mixture. Based on this figure, cells exposed to 100 μM Enzalutamide will die after 8 hours. As a result, the on-chip experiments were performed for about 8 hours to make sure that all cells will die by the end of the experiment.

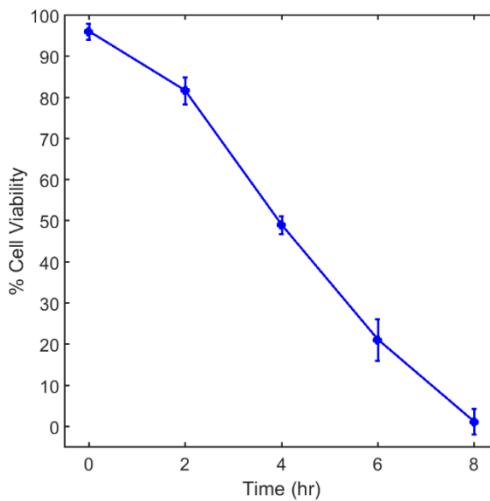


Figure 5.5 Percentile viability of PC-3 cells exposed to 100 μM Enzalutamide.

5.2.2. DS Measurements

For drug tests, PC-3 cells were mixed with LCB containing 100 μM Enzalutamide. The mixture is pumped through the microfluidic channel at 2 $\mu\text{l}/\text{min}$ volumetric flowrate.

Afterward, the electrodes are energized at $4 V_{pp}$ with 5 MHz frequency to capture the cells. The cell capture process is monitored under the microscope, and it is observed that all the micro-wells are filled with PC-3 cells within 30 s. More information on the cell loading process is given in chapters 3 and 4. Finally, the microfluidic device is connected to a high precision impedance analyzer, and the impedance spectra of trapped cells population are recorded continuously for 8 hours. Each impedance measurement is repeated three times, and the averaged data is reported in this chapter. Figure 5.6 shows the normalized standard deviation (standard deviation divided by mean) of the healthy cells' impedance value and phase angle in the frequency range. It is evident that the normalized standard deviation is less than 1% in the whole frequency spectrum.

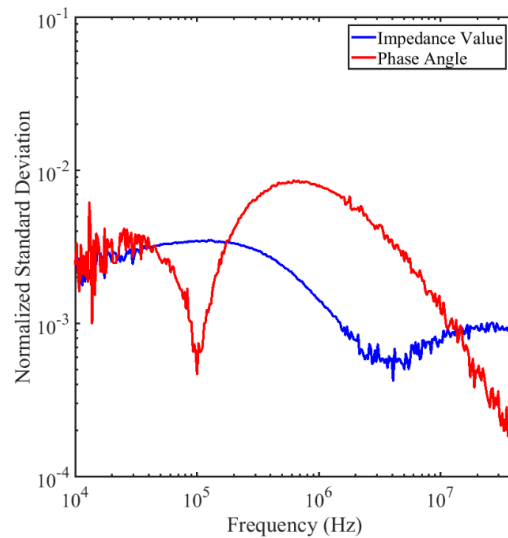


Figure 5.6 Normalized standard deviation of impedance value and phase angle of healthy cells.

Using the equivalent circuit model explained in chapter 4, the EP effect is extracted. Figures 5.7a-b show the impedance and phase angle spectra before and after the EP effect is extracted 2 hours after drug injection. It is evident that EP overshadows impedance spectrum at lower frequencies, and it is necessary to extract this effect before further analyses. Figures 5.7c-d show the impedance and phase angle spectra of freshly captured cells, and the same cell sample after 2 and 8 hours, after subtraction of the EP effects. Based on the impedance spectra, the freshly captured cells show higher impedance magnitudes at lower frequencies while they experience a lower value at higher frequencies. Undamaged cells have healthy integrated membranes, while damaged cells lose their membrane integrity resulting in an outflow of ions to the exterior medium, which in turn increases overall impedance value at higher frequencies. Based on Figure 5.7d, the phase angle changes at higher frequencies is low. However, there is a recognizable change in the phase angle at low and medium frequencies. This can be explained since healthy cells have an integrated membrane which acts as an insulator and makes the system more capacitive (lower phase angle) compared to the damaged cells. The other important point here is the presence of two distinct dispersion regions for the fresh sample which can be detected by inflection points in impedance spectrum. These two dispersion regions are related to the cell membrane polarization ($\sim 100\text{kHz}$) and SU8-medium polarization ($\sim 10\text{ MHz}$), respectively. However, when the cells are exposed to Enzalutamide for a longer time, the first dispersion region starts to vanish due to the membrane damage.

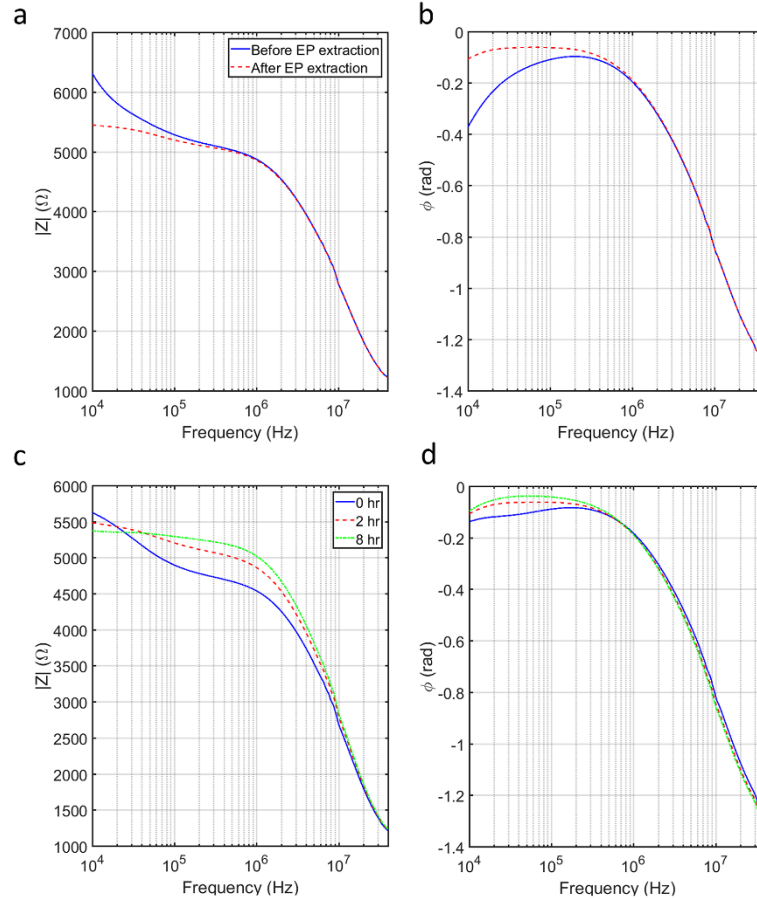


Figure 5.7 a) Impedance spectra and b) phase angle of PC-3 cells treated with 100 μ M Enzalutamide for two hours before and after EP extraction. c) Impedance spectra and d) phase angle spectra of PC-3 cells treated with 100 μ M Enzalutamide at 0, 2, and 8 hours.

5.2.3. Equivalent Circuit Analysis

The equivalent circuit model was used to evaluate the membrane capacitance and cytoplasmic resistance of PC-3 cells treated with 100 μ M Enzalutamide for 0, 2, 4, 6, and 8 hours. Figure 5.8 shows the extracted cell parameters for 8 hours. The error bars indicate

the changes in R_{cyt} and C_{mem} due to variations in initial conditions used for fitting the impedance data with the equivalent circuit model. The initial conditions were selected randomly in $\pm 200\%$ range of the values measured in the previous chapters. Based on Figure 5.8a, C_{mem} started from a value of 1.57×10^{-11} F and decreased slightly to 1.40×10^{-11} F as the cells were exposed to the drug for 8 hours. This 12.1% decrease in membrane capacitance is related to rounding up of the cells to a spherical shape due to cell cytoskeletal tension after releasing in LCB [99]. Figure 5.8b shows that R_{cyt} has a value of $7.64 \times 10^5 \Omega$ for healthy cells and increases as the cells are degraded. The dead cells (after 8 hours) have an R_{cyt} of $1.43 \times 10^6 \Omega$, which is 87.2% larger than the live cells. This makes R_{cyt} a good indicator in discriminating between live and dead cells. The increase in R_{cyt} is due to efflux of cytoplasmic ions to the extracellular medium, which happens because of membrane degradation and ionic diffusion.

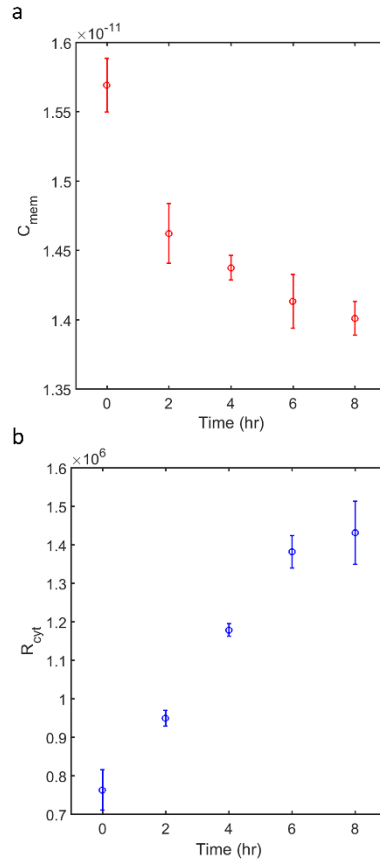


Figure 5.8 Extracted a) membrane capacitance and b) cytoplasmic resistance of PC-3 cells over 8 hours.

5.2.4. Single Frequency Measurements

Figure 5.9 shows the impedance value and phase angle changes at 10 kHz, 100 kHz, and 1 MHz frequency. At 10 kHz, the trend is slightly decreasing, showing that cell impedance is descending because of the membrane damage (as evidenced by the cell viability experiments). Moreover, the phase angle graph shows that the system becomes more resistive over time. At higher frequencies (100 kHz and 1 MHz), impedance value increases

with time, which is due to the outflow of ions from cell cytoplasm. Additionally, phase angle graphs predict a more resistive system over time. However, for 1 MHz phase angle changes only slightly, which agrees with the results presented in Figure 5.7.

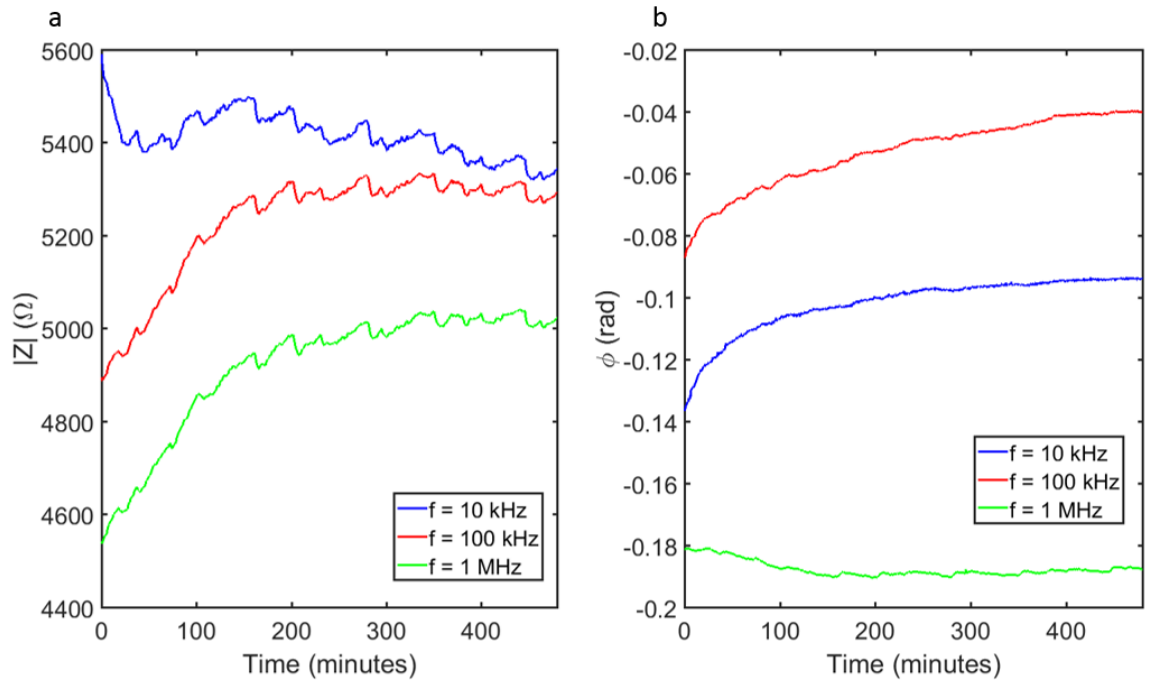


Figure 5.8 Changes over time in a) Impedance value and b) phase angle of PC-3 cells treated with 100µM Enzalutamide.

5.2.5. Principal Component Analysis

The principal component analysis was performed on impedance value and phase angle spectra of PC-3 cells exposed to 100 µM Enzalutamide. The data table consists of rows having the impedance value spectrum at each time step. Figure 5.9a shows the scree plot of first 20 eigenvalues. The order of the first two components is two orders larger than the

third one. As a result, the first two components are enough to represent all the data. PCA results show that the first two principal components explain 99.6% of the variation in the data (PC1: 74.5%, PC2: 25.1%). Figure 5.9b illustrates the coefficients of the first two principal components. The coefficients show the relative weight of each variable in the component. This graph clearly shows what frequencies contribute more to which principal components. PC1 is more related to high frequencies, while PC2 has more contribution from lower frequencies. These coefficient plots have also been calculated for impedance spectra after eliminating the EP effect and stray capacitances and are shown in Figure 5.10.

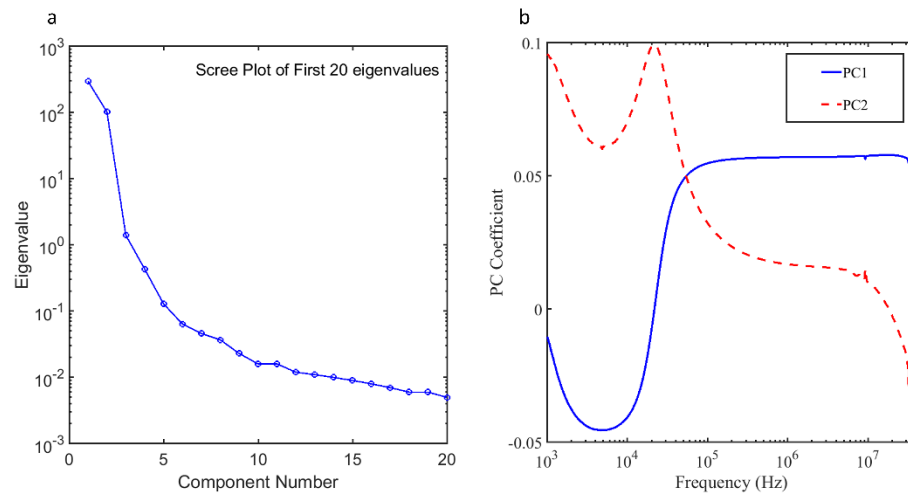


Figure 5.9 a) Scree plot of first 20 components, and b) first two principal component coefficients.

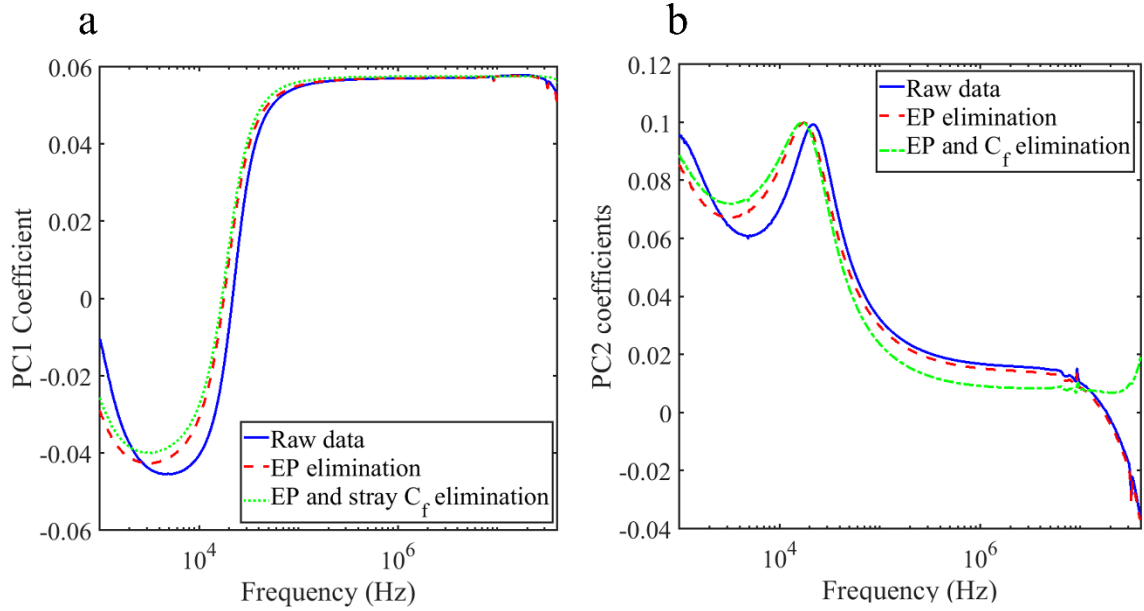


Figure 5.10 a) First principal component and b) second principal component coefficient of raw impedance data, after EP elimination, and after EP & stray capacitance elimination.

These figures suggest that eliminating EP and stray capacitance does not have a considerable effect on PC coefficients. As a result, PCA can be performed on raw data without losing accuracy. The value that the impedance spectra (each row in the data table) have in the PC coordinate system are called scores. Figure 5.11a shows the score plot of the first two PCs. Each data point in this graph represents the impedance spectrum at a time. From this graph, the data points are finally accumulated in a vertical region. Figure 5.11b shows the time variation of PC1 and PC2 score values.

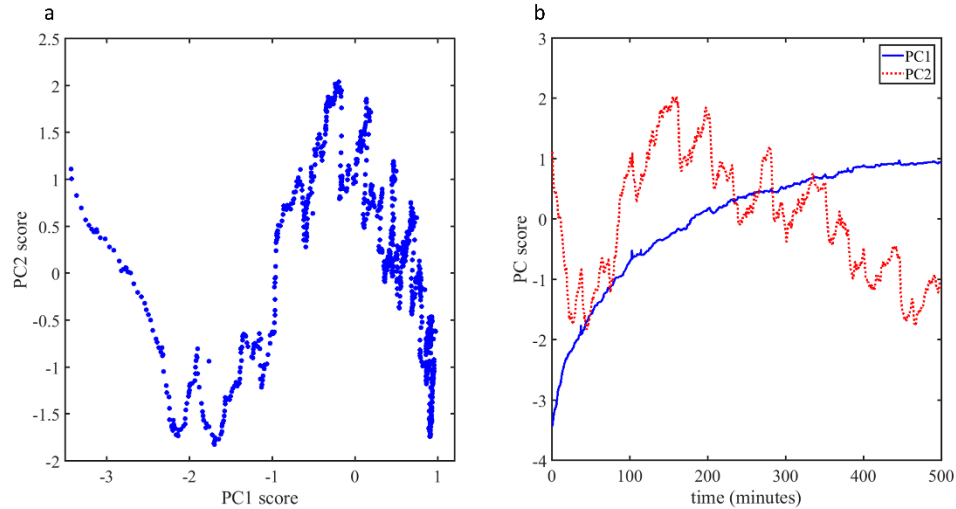


Figure 5.11 a) Score plot of the first two principal components and b) PC score variations with respect to time.

Based on this figure, PC1 score value reaches a constant value after 8 hours showing that the cells are completely dead. However, the PC2 score value is still changing with time. It is mostly because the smaller contribution of PC2 with respect to PC1 in representing the data. To clarify the changes in PC2 score values, PCA was performed by changing the starting frequency to 1, 10, 25, and 50 kHz. Table 5.1 shows the components eigenvalues and % of variance explained using various starting frequencies. Based on this table, the 1st PC eigenvalue is not very sensitive to the starting frequency while the 2nd PC eigenvalue decreases dramatically with increasing starting frequency. As a result, the % of variance explained by 2nd PC is sensitive to the starting frequency, and it is practically unimportant for starting frequencies more than 25 kHz as its value and contribution to variance decreases beyond this frequency.

Table 5.1 Eigenvalues and % of variance explained using different starting frequencies.

Starting frequency	Eigenvalue, 1 st PC	Eigenvalue, 2 nd PC	% of variance explained, 1 st PC	% of variance explained, 2 nd PC
1 kHz	297.831	100.890	74.272	25.160
10 kHz	265.535	47.472	84.565	15.118
25 kHz	261.333	17.233	93.668	6.177
50 kHz	252.796	7.838	96.857	3.003

Additionally, PCA was done on the data set with different starting frequencies, and the PC1, and PC2 score results are shown in Figure 5.12.

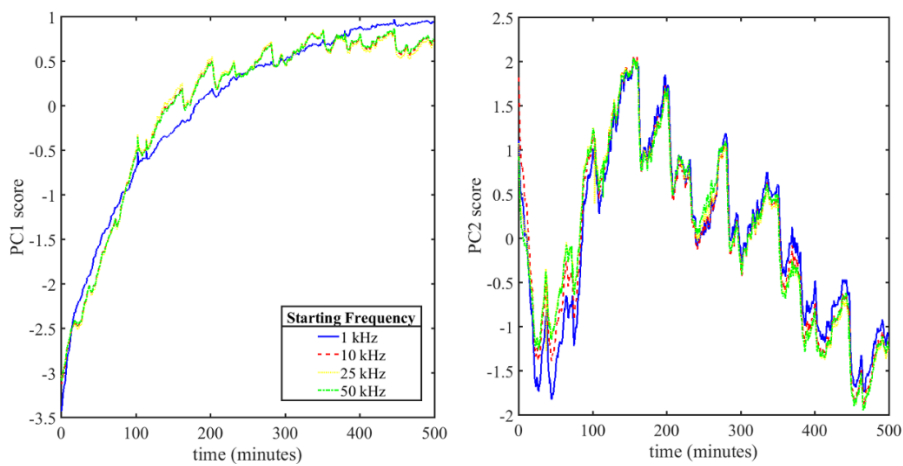


Figure 5.12 a) PC1 and b) PC2 score changes as a function of time for different starting frequencies

This figure clearly shows that both PC1 and PC2 score values are consistent with changing starting frequency up to 50 kHz. As a result of this and the low contribution of PC2, it is concluded that PC1 score value itself is enough to represent the cellular condition.

Moreover, PCA was performed on the phase angle spectrum. Figure 5.13 show the score plot of PC1 and PC2 and their variation with respect to time. Comparing Figures 5.11 and 5.13, it is concluded that both impedance and phase angle spectra follow approximately the same trend and values for the first two principal components. As a result, performing PCA on either impedance or phase angle spectrum will be enough to quantify cell condition.

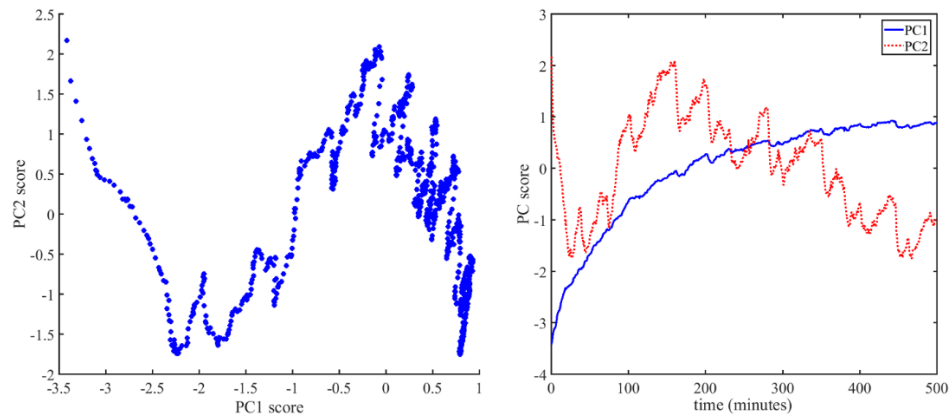


Figure 5.13 a) Phase angle spectra score plot of the first two principal components and b) PC score variations with respect to time.

5.2.6. Opacity Ratio Measurement

The ratio of the impedance magnitude at a high frequency to a low frequency is known as the opacity ratio (OR). This parameter is often utilized to normalize the impedance data for cell size heterogeneity in different cell cultures. In this study, we used 1 MHz and 10 kHz as the high, and low-frequency signal, and the opacity itself is normalized with the initial opacity ratio value. These two frequency points are selected such that both membrane and cytoplasm effects could be considered. At 10 kHz, membrane blocks current flow to the

cytoplasm while at 1 MHz, the current penetrates the cytoplasm. The initial opacity ratios for 100 μM was 0.812. Figure 5.14 shows the changes in normalized opacity ratio (OR) for PC-3 cells exposed to 100 μM Enzalutamide. This figure illustrates that normalized OR increases with time. Opacity increases with either decreasing of the membrane capacitance or increasing of the cytoplasmic resistance. As a result, opacity changes are in good agreement with cell parameter calculations. After 8 hours, the normalized OR reaches a plateau of about 1.16. This plateau means that the cells lost their dynamics, and cell death has been completed.

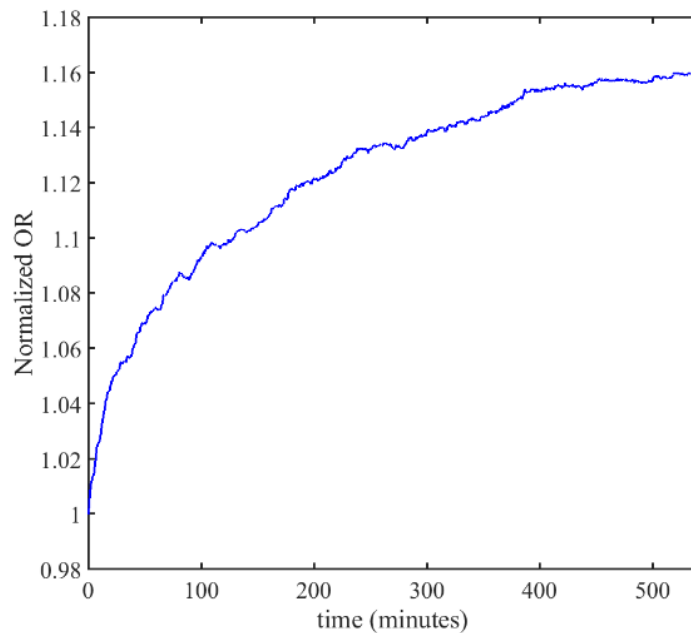


Figure 5.13 Normalized OR of PC-3 cells treated with 100 μM Enzalutamide. Initial OR was 0.812.

5.3. Available Technologies

In the previous sections, we tested the microfluidic device with one high concentration drug. However, to make sure that dielectric spectroscopy can detect the cell death process with lower doses and different cell lines, we used the ECIS (Electric Cell-Substrate Impedance Sensing) system (Applied Biophysics, Inc., Troy, NY) to measure impedance values of a confluent layer of cells adhered to the bottom of wells. For our experiments, we used 8W10E+ PET electrode arrays, which contains eight wells. Each well consists of two interdigitated electrodes with four fingers, and each finger has five 250 μm diameter active electrodes. This means that each well has a total of 40 active electrode sites and can measure approximately 2000-4000 cells. Arrays are connected to the impedance analyzer using an array station. A flat shielded cable which can easily exit the incubator through the rubber seal of the inner glass door connects the array station to the impedance analyzer. Continuous impedance measurements were conducted at 62.5 Hz-64 kHz frequency range. A computer was connected to the impedance analyzer to record the impedance and display the results in real time. Figure 5.14 shows a view of the experimental setup, the array holder, and 8W10E+ electrodes.

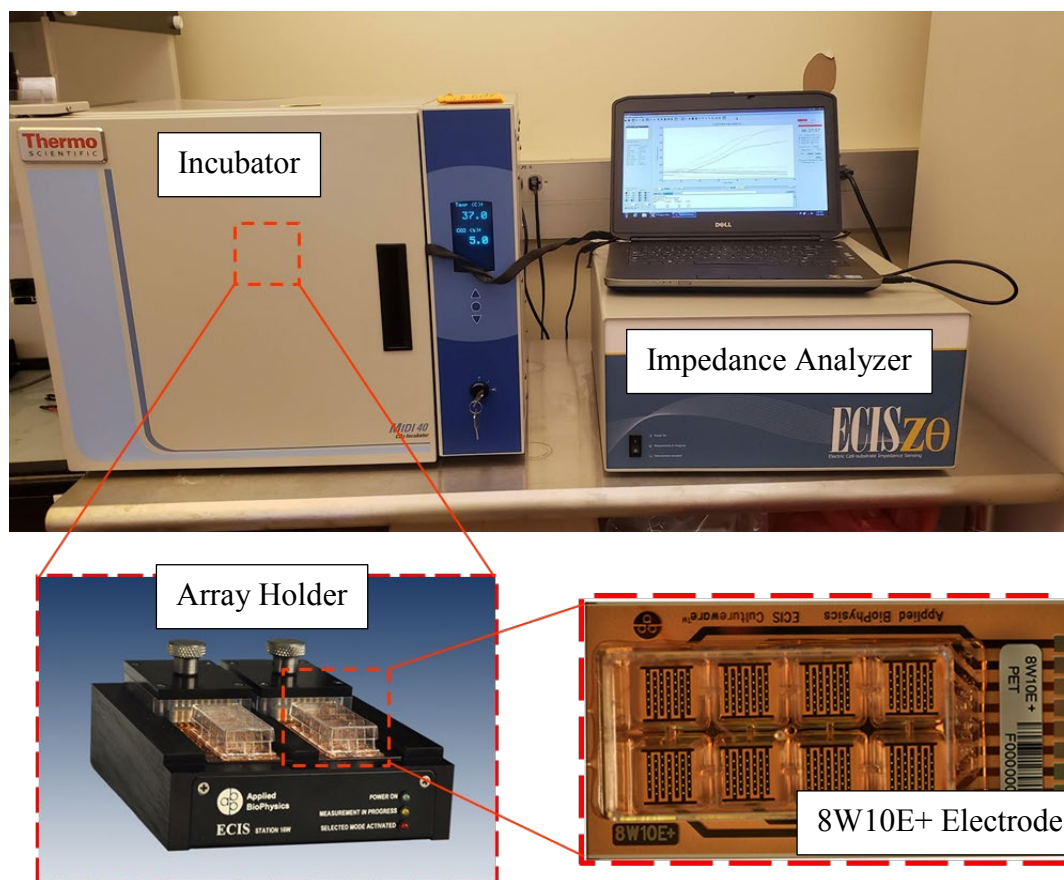


Figure 5.14 A view of the experimental setup, the array holder, and 8W10E+ electrodes with 40 active electrode sites in each well

For the impedance measurements, MCF-7 and DU-145 cell lines were used. MCF-7 is a breast cancer cell line extracted from a 69-year-old Caucasian woman. MCF-7 cell line was cultured in RPMI 1640 growth medium (Sigma-Aldrich) supplemented with 10% FBS (Fetal Bovine Serum) and 5% penicillin-streptomycin. Cells are grown in an incubator at 37°C with 5% CO₂ atmosphere. For cell passaging, the cells are incubated with 0.05% trypsin-EDTA solution (Sigma-Aldrich) for 4 min inside the incubator to detach the cells

from the Petri dish. The growth medium is then added to inhibit the effect of trypsin and cells are centrifuged for 4 min at 2000 rpm and re-suspended in the growth medium. DU-145 is a human prostate cancer cell line derived from a central nervous system metastasis of a 69-year old Caucasian man. The culture atmosphere and passaging protocol are the same as the MCF-7 cell line. For the drug, Mitoxantrone was used, which is an anti-cancer chemotherapy drug for advanced prostate cancer, Acute Myelogenous Leukemia (AML), breast cancer, and non-Hodgkin's lymphoma.

Before running ECIS experiments, the electrical stabilization method is used to clean the electrodes. In this method, the wells are filled with complete medium, and then the electrodes will introduce a high current which will remove the molecules adsorbed on the gold surface. After stabilization, the medium is removed from the wells, and 450 μL monodisperse cell suspension is added to all wells. Our trials show that using cell suspensions with a concentration of 1.8×10^6 cells/well will achieve confluence following attachment and spreading. The electrode arrays are placed inside the incubator to let the cells attach to the surface and confluence the well bottom. In cell culture biology, confluence means the surface is covered with the cells, and no space is left for the cells to grow as a monolayer. Afterward, 50 μL of drug with different concentrations is gently added to each well. The arrays are slid into slots of the array holder, and the connections are checked by performing a series of rapid impedance measurements. If there is any problem in arrays connection, it can be solved by repositioning the arrays. After ensuring the connections, the device is placed inside the incubator, and impedance measurements of each well at 12 different predefined frequencies between 62.5 Hz-64 kHz is continuously conducted. Our data collection showed that each impedance spectrum measurement for

each well takes approximately 13.6 seconds. The real and imaginary parts of the impedance were recorded in a text file and then transferred to MATLAB software for analysis purposes.

450 μL of MCF-7 cells suspended in 0.5% DMSO was added to the wells with a concentration of 1.8×10^6 cells/well and were incubated for 8 hours to attach the bottom well and reach the confluency. 50 μL of Mitoxantrone drug with a concentration of 50, 500, and 5000 nM were added to the wells. For control, for a series of wells, 50 μL of DMSO was added. Each dose was repeated for four wells, and two trials of each dose were performed to ensure repeatability of the measurements. After connecting the slides, continuous impedance measurements were conducted for 96 hours.

Figure 5.15 shows the time variations of the MCF-7 impedance changes ($|Z| - |Z|_{@t=0}$) for control (0 M Mitoxantrone), 50, 500, and 5000 nM Mitoxantrone concentrations at 1, 8, 32, and 64 kHz frequencies. This graph shows that in all frequencies, the 50 nM case shows very similar behavior with the control case. In both cases, the impedance value firstly increases. After that, in both cases, the impedance change starts to decrease. The increase in impedance value is mostly due to the growth of cells in growth medium or low drug condition. The decrease in impedance value is an indicator that cell growth has stopped and cells are undergoing the death process either by apoptosis, necrosis, or nutrient shortage. So, we concluded that 50 nM drug dose has an insignificant effect on cell death. The results for the 500 nM Mitoxantrone case show a slighter increase in impedance value followed by a decrease. From this graph, we can conclude that this drug dose is decreasing cell growth and causing cell death afterwards. The results for 5000 nM drug dose show a continuous decrease in impedance value at all frequencies. This continuous decrease

indicates that this high dose totally stops cell growth and immediately initiates the death process. Another critical point here is that for control and low drug dose (50 nM), the final impedance signal is different from the final signal of high drug doses (500 and 5000 nM). However, high drug doses which will cause total cell death till the end of the experiment show the same final impedance behavior for 1, 8, 32, and 64 kHz frequencies.

450 μL of DU-145 cells suspended in 0.5% DMSO was added to the wells with a concentration of 1.8×10^6 cells/mL and were incubated for 8 hours to attach the bottom well and reach the confluency. The same methodology as the MCF-7 was used for drug introduction, and the experiments were performed for about 150 hours.

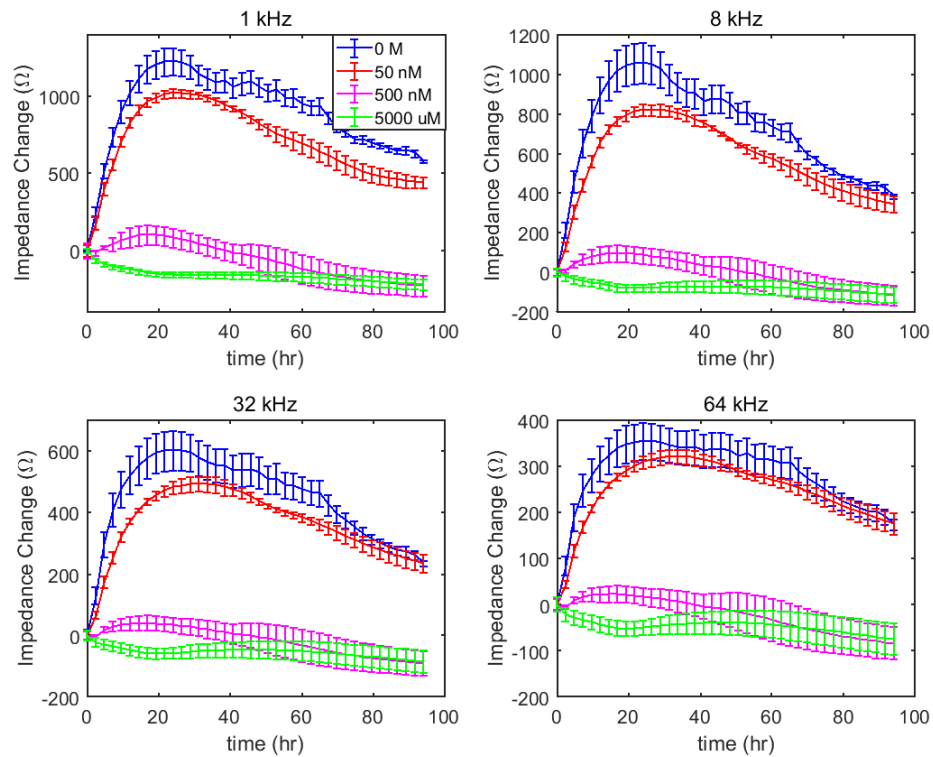


Figure 5.15 Impedance change of MCF-7 cell layer at different drug concentrations and frequencies

Figure 5.16 shows the time variations of the DU-145 impedance changes for control (0 M Mitoxantrone), 50, 500, and 5000 nM Mitoxantrone concentrations at 1, 8, 32, and 64 kHz frequencies. The impedance changes of cells in their growth medium shows an increase till 30 hours followed by a plateau till 80 hours. The plateau will then undergo a slight increase until 120 hours, followed by a slight decrease. These changes are attributed to the cell growth and shortage in cell nutrition after a long time.

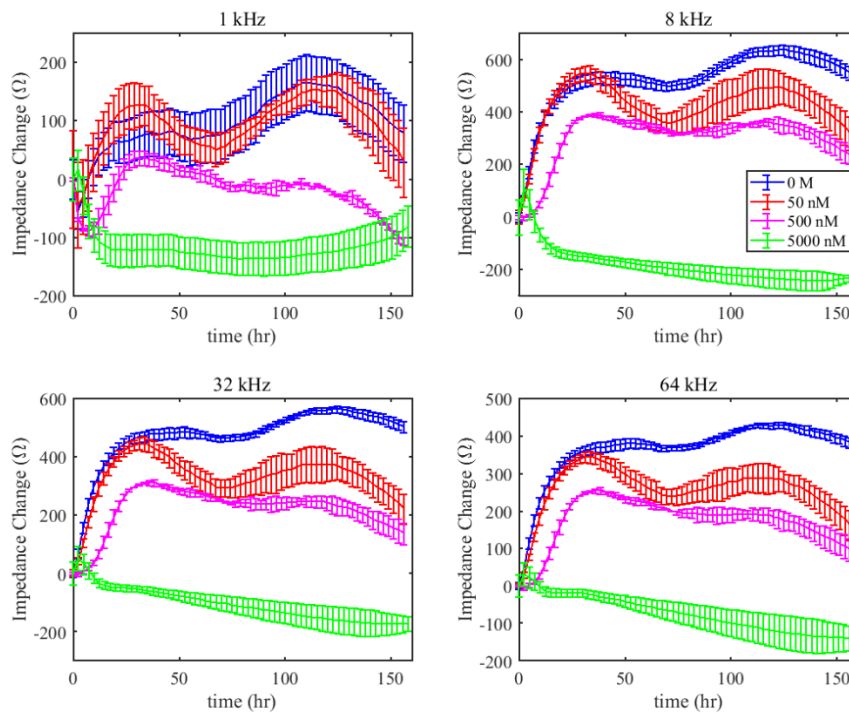


Figure 5.16 Impedance change of DU-145 cell layer at different drug concentrations and frequencies

The impedance changes for 50 nM drug dose shows similar behavior to cells in the growth medium for the first 30 hours. However, after 30 hours, it starts to decrease, showing the effect of the drug. After 72 hours, the cells show resistance to the drug, and impedance increases. Finally, after 120 hours, the impedance starts to decrease again, which is an indicator of a shortage of nutrients as well as drug effect.

For the case of 500 nM drug, the trend is the same as 50 nM. However, since the drug dose is higher, the first increase in impedance is lower and different than the other two cases. Furthermore, the second increase in impedance, which is a result of drug resistance disappeared. Finally, the impedance results revealed that in the case of 5000 nM drug, the impedance change is continuously decreasing till it reaches a plateau which shows a stop in cell function and is an indicator of cell death. In the case of very high concentration, there is a very rapid decrease in impedance, which becomes smaller with time and finally reaches a plateau representing cell death.

The final impedance changes for the MCF-7 and DU-145 cells at different concentration, and at 1, 8, 32, and 64 kHz are plotted in Figure 5.17. Two-tailed t-test was performed on the final impedance change values. The results show that the final value for MCF-7 of control and 50 nM except for 1 kHz are not significantly different ($p < 0.01$). Additionally, the final value of 500 and 5000 nM are not statistically different as well ($p < 0.01$). Figures 5.17a-b show that all the impedance change absolute values decrease with increasing frequency. However, for DU-145 at 1 kHz, strange behavior is observed. This behavior is probably due to the very compact configuration of DU-145 cells, which blocks the electric currents and prevents impedance changes at that frequency. For the case of DU-145 and

MCF-7 cells, the final impedance change decreases with increasing drug concentration except for 1 kHz in the case of DU-145.

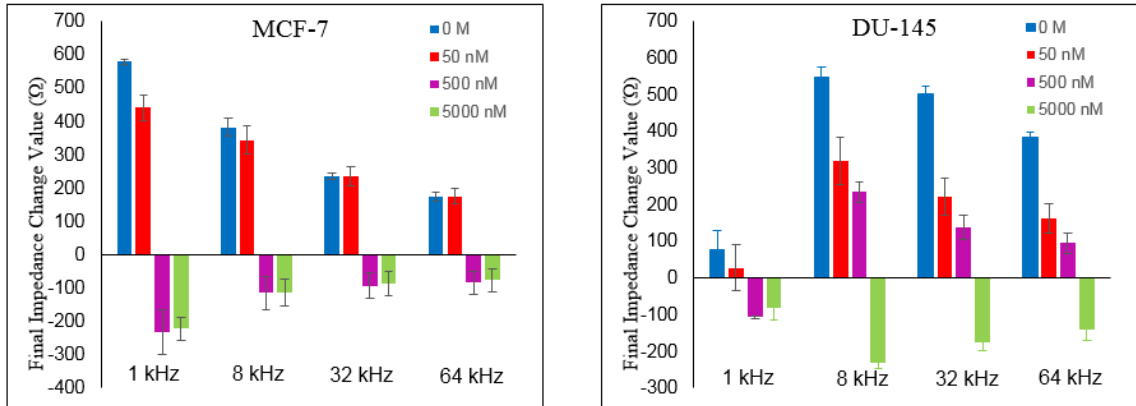


Figure 5.17 Final impedance change values for MCF-7 and DU-145 at different drug concentrations and frequencies

Above results show that Applied Biophysics technology can detect the changes in impedance due to drug application. For the frequency range used in this device, growth, and decay of the cells are related to increase and decrease in impedance values. Since the number of frequency points measured in this device is so limited (maximum 12 points) and it is mostly in the low-frequency region where EP overshadows the measurements, electrical circuit modeling, and PCA will not yield reliable results. The other limitation of this technology is the high number of cells needed for measurements. Moreover, the growth medium is not changed, and the combined effects of nutrients shortage and drug effect are measured.

5.4. Conclusion

In this study, we fabricated and tested an impedance-based microfluidic device to position biological cells inside micro-wells and performed impedance measurements. The PC-3 prostate cancer cell line was used to demonstrate the performance of the device for drug testing purposes. We used conventional dielectric spectroscopy devices to measure the frequencies at which PC-3 cells could be captured inside 30 μm diameter micro-wells. Clausius-Mossotti factor results show that at 5 MHz, PC-3 cells experience the highest pDEP force. After capturing the cells inside the micro-wells, 100 μM Enzalutamide was injected into the microfluidic device, and impedance measurements were performed in the 10 kHz-40 MHz frequency range. Viability tests on PC-3 cells treated with 100 μM Enzalutamide suggest that after about 8 hours, all the cells will die. As a result, impedance measurements were performed in 8 hours. Impedance results show that cells dying exhibit a different spectrum than the healthy ones. Live cells impedance spectra have two dispersion regions, while for dead cells, the first dispersion region disappears.

An equivalent circuit model was used to extract cellular electric properties. C_{mem} started from a value of 1.57×10^{-11} F and decreased slightly to 1.40×10^{-11} F while R_{cyt} started from a value of $7.64 \times 10^5 \Omega$ for healthy cells and increases to $1.43 \times 10^6 \Omega$ for dead cells. Single frequency measurements show that at higher frequencies (>100 kHz) cell dynamics could be captured while lower frequencies are overshadowed with EP effects.

PCA was performed on impedance spectra, and principal component score values at each time step were used to quantify cell state at each time step. PCA results show that eliminating EP effect or stray capacitance does not affect PCA outcome. As a result, PCA

can be performed on raw data. Moreover, it was shown that PC score values do not change considerably by changing the starting frequency value up to 50 kHz. It means that data acquisition would be faster. Additionally, it was shown that the PC1 score starts from -3.43 and converged to 0.95 for the dead cells.

Finally, opacity ratio was introduced to better capture cell dynamics undergoing death process. The results show that OR increases by about 16% for the dead cells compared to fresh cells. Available technology for drug screening purposes was tested for two different cell lines, and the results show that impedance data can detect cell growth and decay. Moreover, the limitations of this technology with our proposed technology was discussed.

5.5. Appendix

5.5.1. PCA Analysis Procedure

The data table is shown with matrix \mathbf{X} , and each element of this data table is represented by x_{ij} . Before performing PCA, the data is usually centered, so the mean of each column is equal to zero. The data analysis will start with p-dimensional feature vectors and projecting them into q-dimensional subspace such that the variance in data is preserved as much as possible. These q-directions are called *principal components* which span the subspace.

In order to simplify the explanation, a one-dimensional projection is firstly considered. If a p-dimensional vector \vec{x}_i is projected to the unit vector \vec{w} , the coordinate in p-dimensional space is $(\vec{x}_i \cdot \vec{w})\vec{w}$. Since the vector \vec{x}_i is centered, the mean of the projections will equal to zero:

$$\frac{1}{n} \sum_{i=1}^n (\vec{x}_i \cdot \vec{w}) \vec{w} = \left(\left(\frac{1}{n} \sum_{i=1}^n x_i \right) \cdot \vec{w} \right) \vec{w} = 0 \quad (5.A1)$$

By using the projected vector instead of the original vector, some errors will happen. The difference between the imaged vector and the real vector is the residual of the projection, which is calculated as:

$$\begin{aligned} \|\vec{x}_i - (\vec{x}_i \cdot \vec{w})\vec{w}\|^2 &= \|\vec{x}_i\|^2 - 2(\vec{x}_i \cdot \vec{w})(\vec{x}_i \cdot \vec{w}) + \|\vec{w}\|^2 \\ &= \|\vec{x}_i\|^2 - 2(\vec{x}_i \cdot \vec{w})^2 + 1 \end{aligned} \quad (5.A2)$$

By adding all these residuals across all the vectors, Residual Sum of Squares for vector $\vec{\omega}$ ($RSS(\vec{\omega})$) is calculated:

$$\sum_{i=1}^n (\|\vec{x}_i\|^2 - 2(\vec{x}_i \cdot \vec{\omega})^2 + 1) = \left(n + \sum_{i=1}^n \|\vec{x}_i\|^2 \right) - 2 \sum_{i=1}^n (\vec{x}_i \cdot \vec{\omega})^2 \quad (5.A3)$$

In order to have the best representation of actual data, $RSS(\vec{\omega})$ must be minimized. The first term in the right-hand side is independent of $\vec{\omega}$. As a result, the second term needs to be maximized. However, for the sake of calculations $\frac{1}{n} \sum_{i=1}^n (\vec{x}_i \cdot \vec{\omega})^2$ will be maximized in this case. We know that the mean of a square is equal to the square of the mean added with the variance.

$$\frac{1}{n} \sum_{i=1}^n (\vec{x}_i \cdot \vec{\omega})^2 = \left(\frac{1}{n} \sum_{i=1}^n (\vec{x}_i \cdot \vec{\omega}) \right)^2 + Var[\vec{x}_i \cdot \vec{\omega}] \quad (5.A4)$$

Since the data are centered, the optimization problem will reduce to maximizing the variance of the projections ($Var[\vec{x}_i \cdot \vec{\omega}]$).

Now if we stack our n data vectors into a $n \times p$ matrix, then projections are given by $X\omega$.

Then the variance is:

$$\begin{aligned} \sigma_{\vec{\omega}}^2 &= \frac{1}{n} \sum_{i=1}^n (\vec{x}_i \cdot \vec{\omega})^2 = \frac{1}{n} (\mathbf{X}\mathbf{w})^T (\mathbf{X}\mathbf{w}) = \frac{1}{n} \mathbf{w}^T \mathbf{X}^T \mathbf{X} \mathbf{w} = \mathbf{w}^T \frac{\mathbf{X}^T \mathbf{X}}{n} \mathbf{w} \\ &= \mathbf{w}^T \mathbf{V} \mathbf{w} \end{aligned} \quad (5.A5)$$

The aim is finding vector \mathbf{w} that maximizes $\mathbf{w}^T \mathbf{V} \mathbf{w}$ with the constraint $\mathbf{w}^T \mathbf{w} = 1$. The Lagrangian multiplier technique can be used here for solving this optimization problem. In this method, a new variable (λ), called a Lagrange multiplier, is introduced. In this problem, the Lagrange function is written as:

$$u = \mathbf{w}^T \mathbf{V} \mathbf{w} - \lambda(\mathbf{w}^T \mathbf{w} - 1) \quad (5.A6)$$

To find the optimized values of \mathbf{w} for the function u , the derivative of u relative to \mathbf{w} is computed and then is set to zero:

$$\frac{\partial u}{\partial \mathbf{w}} = 2\mathbf{V}\mathbf{w} - 2\lambda\mathbf{w} = 0 \quad (5.A7)$$

$$\mathbf{V}\mathbf{w} = \lambda\mathbf{w} \quad (5.A8)$$

Equation 5.A8 shows that the “to be found” vector \mathbf{w} is an eigenvector of the covariance matrix \mathbf{V} , and the one providing the largest variance is associated with the largest λ . The variance can also be computed by combining Equations 5.A5 and 5.A8:

$$\sigma_{\hat{\omega}}^2 = \mathbf{w}^T \mathbf{V} \mathbf{w} = \lambda \quad (5.A9)$$

Equation 5.A9 illustrates that eigenvalues of \mathbf{V} are the variance of the data explained by the eigenvector. As a result, the fraction of the data explained by each eigenvector (principal component) is equal to:

$$f_j = \frac{\lambda_j}{\sum_{i=1}^p \lambda_i} \quad (5.A10)$$

Chapter 6

SUMMARY AND FUTURE RESEARCH

This dissertation introduces a new microfluidic device which can capture biological cells in confined geometries, namely micro-wells, measure the cell responses using dielectric spectroscopy, and finally release the cells. To show the capabilities of the device, yeast cells were used. However, small sizes of yeast cells compared to micro-wells size prevents measurement of cell parameters. As a result, the PC-3 cell line was used in the microfluidic device, and its response to conductivity and pH change was measured. Moreover, the response of PC-3 cell to an anti-cancer drug was measured, and the impedance data were analyzed using different methods.

6.1 Summary of the current work

In chapter 1, a brief introduction to DS and its potential applications is given. Afterward, different methods for positioning cells and particles are discussed, and DEP as a contact-free and straightforward approach is introduced. Finally, we discussed how the combination of DEP and DS could fulfill the requirements of this research.

Chapter 2 elaborates on polarization theory and different relaxation phenomena. Specifically, interfacial polarization theory is given, and its effect on dipole moment of particles is thoroughly discussed. Afterward, the complex permittivity of a suspension of particles is elucidated, and different mixture models are discussed. Finally, the theory of electrical forces on particles, especially the DEP force, is explained.

In chapter 3, the microchip that consists of electro-activated micro-well arrays for positive dielectrophoresis (pDEP) assisted cell capture, DS measurements, and negative dielectrophoresis (nDEP) driven cell unloading is demonstrated. Device performance is tested using *Saccharomyces Cerevisiae* (yeast) cells at different conditions. Moreover, numerical simulations are performed and are compared with experimental results.

Chapter 4 investigates the dielectric spectroscopy of single PC-3 cells inside each micro-well. An equivalent circuit model was developed to extract the cell membrane capacitance and cell cytoplasmic conductivity from the impedance spectra. We report the time course of the variations in dielectric properties of PC-3 cells suspended in LCB and their response to sudden pH change from a pH of 7.3 to a pH of 5.8.

Chapter 5 focuses on the application of the microfluidic device to measure the anti-cancer drug response of PC-3 cells. Equivalent circuit modeling is used to extract the cell electrical properties as a function of time. Principal component analysis (PCA) is used to quantify cellular response to the drug as a function of time. Single frequency measurements are conducted to observe how the cell's response over time. Finally, opacity ratio (OR) is defined as an additional quantification method. Moreover, an available technology from Applied Biophysics is tested for two different cell lines, and drawbacks of this technology are explained.

6.2 Future Research

As the conductivity of a medium increases, the EP effect overshadows the impedance spectrum, especially in the low-frequency region. As a result, the sensitivity of the

measurements decreases. Moreover, high conductivity medium decreases DEP effects drastically such that pDEP force vanishes for the whole frequency spectrum and the nDEP force become so weak that it is not able to release the cells. Our group has developed an electrochemical deposition technique to coat electrodes with gold nanostructures. The increased surface area due to deposition of nanostructures decreases electrical impedance at the interface. In the future, we plan to use the same methodology to find out the optimum materials and electrochemical deposition conditions to decrease electrode polarization effect and increase the sensitivity of our measurements. Figure 6.1 shows a trial of coating the electrodes with nanostructures as well as the drastic decrease in EP effect by using modified electrodes at high conductivity medium.

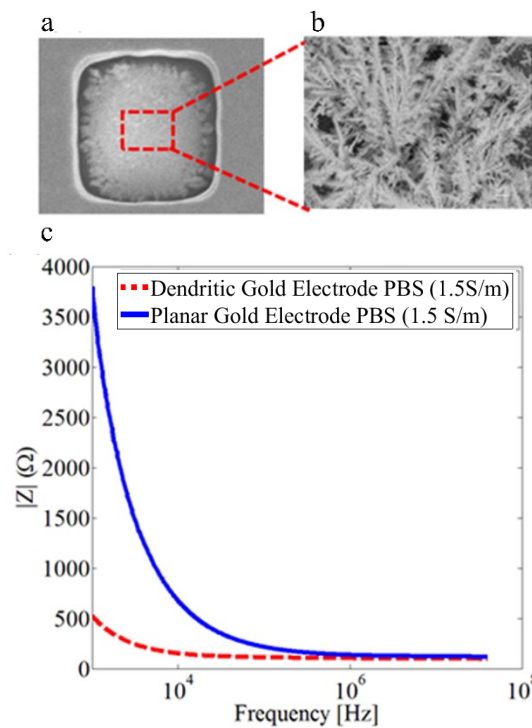


Figure 6.1 a) Microscopy and b) SEM images of the coated electrodes. c) Impedance spectrum of PBS (1.5 S/m) measured with planar and coated electrodes.

Our current device can measure the impedance of a 400-500 cell population. However, cell-to-cell differences always exist, and average measurements of a population may not indicate the behaviors of individual cells. As a result, there is a great need to develop technologies that can measure cellular heterogeneity. For the future, our microfluidic device could be extended for single-cell measurements. For the electrode configuration, in this case, parallel strip electrodes will be fabricated for top and bottom electrodes, and they will face each other and cross at 90° angle. This configuration enables single particle/cell handling and impedance measurements at strips junction by activating relevant top and bottom electrodes. Figure 6.1 shows a side view of the bottom and top substrates as well as electrodes configuration and alignments of slides.

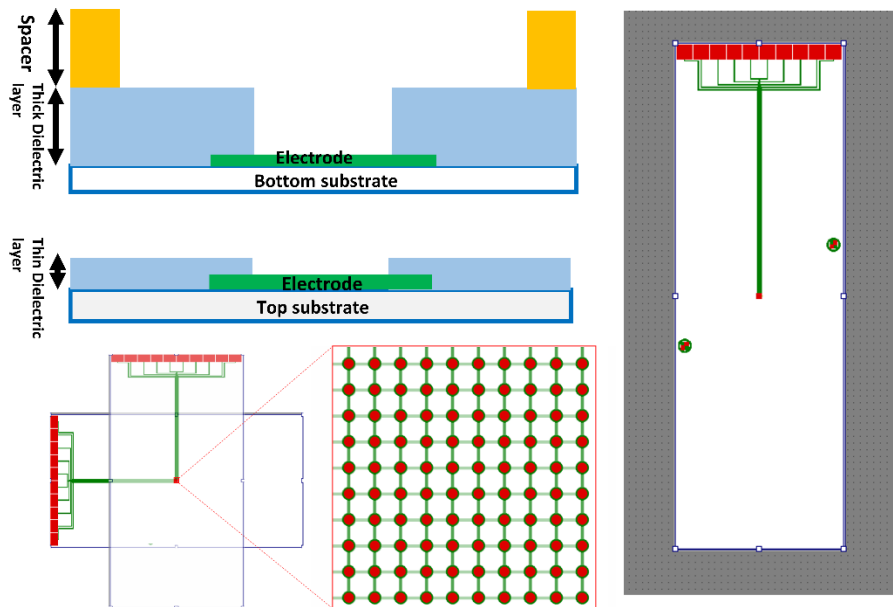


Figure 6.2 Side view of a) bottom and b) top substrate. c) Electrode configuration and d) alignment of top and bottom substrates.

The top and bottom electric connections would have an N:1 multiplexer (N is the number of electrode strips). The multiplexer is software controlled through a USB by an Arduino or an equivalent dedicated circuitry that can be programmed to perform capture/release functions and the impedance measurements for all possible electrode pairs on top and bottom.

References

1. Yardley, J.E., et al., *On-line, real-time measurements of cellular biomass using dielectric spectroscopy*. Biotechnology and Genetic Engineering Reviews, 2000. **17**(1): p. 3-36.
2. Patel, P.M., A. Bhat, and G.H. Markx, *A comparative study of cell death using electrical capacitance measurements and dielectrophoresis*. Enzyme and Microbial Technology, 2008. **43**(7): p. 523-530.
3. Sonja, H., E. Daniel, and F. Jürg, *Modelling effective dielectric properties of materials containing diverse types of biological cells*. Journal of Physics D: Applied Physics, 2010. **43**(36): p. 365405.
4. Frezza, F., et al., *In silico validation procedure for cell volume fraction estimation through dielectric spectroscopy*. Journal of Biological Physics, 2015. **41**(3): p. 223-234.
5. Heileman, K., J. Daoud, and M. Tabrizian, *Dielectric spectroscopy as a viable biosensing tool for cell and tissue characterization and analysis*. Biosensors & Bioelectronics, 2013. **49**: p. 348-359.
6. Fernandez, R.E., et al., *Flexible Bioimpedance Sensor for Label-Free Detection of Cell Viability and Biomass*. Ieee Transactions on Nanobioscience, 2015. **14**(7): p. 700-706.
7. Bürgel, S.C., et al., *On-chip electroporation and impedance spectroscopy of single-cells*. Sensors and Actuators B: Chemical, 2015. **210**: p. 82-90.

8. Morgan, H., et al., *Single cell dielectric spectroscopy*. Journal of Physics D-Applied Physics, 2007. **40**(1): p. 61-70.
9. Gawad, S., et al., *Dielectric spectroscopy in a micromachined flow cytometer: theoretical and practical considerations*. Lab on a Chip, 2004. **4**(3): p. 241-251.
10. Cheung, K., S. Gawad, and P. Renaud, *Impedance spectroscopy flow cytometry: On-chip label-free cell differentiation*. Cytometry Part A, 2005. **65A**(2): p. 124-132.
11. Han, A., L. Yang, and A.B. Frazier, *Quantification of the heterogeneity in breast cancer cell lines using whole-cell impedance spectroscopy*. Clinical cancer research, 2007. **13**(1): p. 139-143.
12. Justice, C., et al., *Process control in cell culture technology using dielectric spectroscopy*. Biotechnology Advances, 2011. **29**(4): p. 391-401.
13. Heileman, K.L. and M. Tabrizian, *Dielectric spectroscopy platform to measure MCF10A epithelial cell aggregation as a model for spheroidal cell cluster analysis*. Analyst, 2017. **142**(9): p. 1601-1607.
14. Eker, B., et al., *Label-free recognition of drug resistance via impedimetric screening of breast cancer cells*. PloS one, 2013. **8**(3): p. e57423.
15. Holmes, D., et al., *Leukocyte analysis and differentiation using high speed microfluidic single cell impedance cytometry*. Lab on a Chip, 2009. **9**(20): p. 2881-2889.
16. Caduff, A., et al., *First human experiments with a novel non-invasive, non-optical continuous glucose monitoring system*. Biosensors and Bioelectronics, 2003. **19**(3): p. 209-217.

17. Daoud, J., et al., *Dielectric spectroscopy for non-invasive monitoring of epithelial cell differentiation within three-dimensional scaffolds*. *Physics in medicine and biology*, 2012. **57**(16): p. 5097.
18. Kustermann, S., et al., *A label-free, impedance-based real time assay to identify drug-induced toxicities and differentiate cytostatic from cytotoxic effects*. *Toxicology in Vitro*, 2013. **27**(5): p. 1589-1595.
19. Leung, G., et al., *Cellular dielectric spectroscopy: a label-free technology for drug discovery*. *JALA: Journal of the Association for Laboratory Automation*, 2005. **10**(4): p. 258-269.
20. Valero, A., T. Braschler, and P. Renaud, *A unified approach to dielectric single cell analysis: Impedance and dielectrophoretic force spectroscopy*. *Lab on a Chip*, 2010. **10**(17): p. 2216-2225.
21. Tabeling, P., *Introduction to microfluidics*. 2005: Oxford University Press on Demand.
22. Squires, T.M. and S.R. Quake, *Microfluidics: Fluid physics at the nanoliter scale*. *Reviews of modern physics*, 2005. **77**(3): p. 977.
23. Schwan, H.P., *Dielectric spectroscopy and electro-rotation of biological cells*. *Ferroelectrics*, 1988. **86**(1): p. 205-223.
24. Gabriel, S., R. Lau, and C. Gabriel, *The dielectric properties of biological tissues: III. Parametric models for the dielectric spectrum of tissues*. *Physics in medicine and biology*, 1996. **41**(11): p. 2271.
25. Gheorghiu, E., *Measuring living cells using dielectric spectroscopy*. *Bioelectrochemistry and Bioenergetics*, 1996. **40**(2): p. 133-139.

26. Grenier, K., et al., *Recent advances in microwave-based dielectric spectroscopy at the cellular level for cancer investigations*. IEEE Transactions on Microwave Theory and Techniques, 2013. **61**(5): p. 2023-2030.
27. Roman, G.T., et al., *Single-cell manipulation and analysis using microfluidic devices*. Analytical and bioanalytical chemistry, 2007. **387**(1): p. 9-12.
28. Noll, T. and M. Biselli, *Dielectric spectroscopy in the cultivation of suspended and immobilized hybridoma cells*. Journal of Biotechnology, 1998. **63**(3): p. 187-198.
29. Arai, F., et al., *On chip single-cell separation and immobilization using optical tweezers and thermosensitive hydrogel*. Lab on a Chip, 2005. **5**(12): p. 1399-1403.
30. Werner, M., et al., *Microfluidic array cytometer based on refractive optical tweezers for parallel trapping, imaging and sorting of individual cells*. Lab on a Chip, 2011. **11**(14): p. 2432-2439.
31. Cabrera, H., et al., *Experimental determination of trapping efficiency of optical tweezers*. Philosophical Magazine Letters, 2013. **93**(11): p. 655-663.
32. Conteduca, D., et al., *Design of a high-performance optical tweezer for nanoparticle trapping*. Applied Physics a-Materials Science & Processing, 2016. **122**(4).
33. Khademhosseini, A., et al., *Molded polyethylene glycol microstructures for capturing cells within microfluidic channels*. Lab on a Chip, 2004. **4**(5): p. 425-430.
34. Wang, S.T., et al., *Three-Dimensional Nanostructured Substrates toward Efficient Capture of Circulating Tumor Cells*. Angewandte Chemie-International Edition, 2009. **48**(47): p. 8970-8973.

35. Arumugam, P.U., et al., *Dielectrophoretic trapping of single bacteria at carbon nanofiber nanoelectrode arrays*. The Journal of Physical Chemistry A, 2007. **111**(49): p. 12772-12777.
36. Madiyar, F.R., et al., *Manipulation of bacteriophages with dielectrophoresis on carbon nanofiber nanoelectrode arrays*. Electrophoresis, 2013. **34**(7): p. 1123-1130.
37. Madiyar, F., et al., *Electrical Capture and Detection of Microbes Using Dielectrophoresis at Nanoelectrode Arrays In. Advances in Applied Nanotechnology for Agriculture Chapter*, 2013. **6**: p. 109-124.
38. Inoue, I., et al., *On-chip culture system for observation of isolated individual cells*. Lab on a Chip, 2001. **1**(1): p. 50-55.
39. Bernhard, D.D., S. Mall, and P. Pantano, *Fabrication and Characterization of Microwell Array Chemical Sensors*. Analytical Chemistry, 2001. **73**(11): p. 2484-2490.
40. Wang, Y., et al., *Trapping cells on a stretchable microwell array for single-cell analysis*. Analytical and Bioanalytical Chemistry, 2012. **402**(3): p. 1065-1072.
41. Hoettges, K.F., et al., *Dielectrophoresis-activated multiwell plate for label-free high-throughput drug assessment*. Analytical chemistry, 2008. **80**(6): p. 2063-2068.
42. Broche, L.M., et al., *Rapid, automated measurement of dielectrophoretic forces using DEP-activated microwells*. Electrophoresis, 2011. **32**(17): p. 2393-2399.

43. Bocchi, M., et al., *Dielectrophoretic trapping in microwells for manipulation of single cells and small aggregates of particles*. Biosensors and Bioelectronics, 2009. **24**(5): p. 1177-1183.
44. Mittal, N., A. Rosenthal, and J. Voldman, *nDEP microwells for single-cell patterning in physiological media*. Lab on a Chip, 2007. **7**(9): p. 1146-1153.
45. Luo, C., et al., *The combination of optical tweezers and microwell array for cells physical manipulation and localization in microfluidic device*. Biomedical Microdevices, 2007. **9**(4): p. 573-578.
46. Ameri, S.K., P.K. Singh, and S. Sonkusale, *Utilization of graphene electrode in transparent microwell arrays for high throughput cell trapping and lysis*. Biosensors and Bioelectronics, 2014. **61**: p. 625-630.
47. Park, C.B. and D.S. Clark, *Sol-gel encapsulated enzyme arrays for high-throughput screening of biocatalytic activity*. Biotechnology and Bioengineering, 2002. **78**(2): p. 229-235.
48. Lee, M.-Y., et al., *Metabolizing enzyme toxicology assay chip (MetaChip) for high-throughput microscale toxicity analyses*. Proceedings of the National Academy of Sciences, 2005. **102**(4): p. 983-987.
49. Wada, K.I., et al., *Live cells-based cytotoxic sensorchip fabricated in a microfluidic system*. Biotechnology and bioengineering, 2008. **99**(6): p. 1513-1517.
50. Ruppen, J., et al., *Towards personalized medicine: chemosensitivity assays of patient lung cancer cell spheroids in a perfused microfluidic platform*. Lab on a Chip, 2015. **15**(14): p. 3076-3085.

51. Jain, K., *Applications of biochips: from diagnostics to personalized medicine*. Current opinion in drug discovery & development, 2004. **7**(3): p. 285-289.
52. Xu, Z., et al., *Application of a microfluidic chip-based 3D co-culture to test drug sensitivity for individualized treatment of lung cancer*. Biomaterials, 2013. **34**(16): p. 4109-4117.
53. Wood, D.K., et al., *Single cell trapping and DNA damage analysis using microwell arrays*. Proceedings of the National Academy of Sciences, 2010. **107**(22): p. 10008-10013.
54. Moeller, H.C., et al., *A microwell array system for stem cell culture*. Biomaterials, 2008. **29**(6): p. 752-763.
55. Yuan, J. and P.A. Sims, *An Automated Microwell Platform for Large-Scale Single Cell RNA-Seq*. bioRxiv, 2016: p. 070193.
56. Jo, S.M., et al., *Nanotentacle-Structured Magnetic Particles for Efficient Capture of Circulating Tumor Cells*. Small, 2015. **11**(16): p. 1975-1982.
57. Chung, J., Y.-J. Kim, and E. Yoon, *Highly-efficient single-cell capture in microfluidic array chips using differential hydrodynamic guiding structures*. Applied physics letters, 2011. **98**(12): p. 123701.
58. Evander, M., et al., *Noninvasive acoustic cell trapping in a microfluidic perfusion system for online bioassays*. Analytical chemistry, 2007. **79**(7): p. 2984-2991.
59. Fernandez, R.E., et al., *Platinum black electrodeposited thread based electrodes for dielectrophoretic assembly of microparticles*. Biomicrofluidics, 2016. **10**(3): p. 033101.

60. Kim, S.H., et al., *Electroactive Microwell Arrays for Highly Efficient Single-Cell Trapping and Analysis*. *Small*, 2011. **7**(22): p. 3239-3247.
61. Cordovez, B., D. Psaltis, and D. Erickson, *Trapping and storage of particles in electroactive microwells*. *Applied Physics Letters*, 2007. **90**(2): p. 024102.
62. Yoshimura, Y., et al., *Cell Pairing Using Microwell Array Electrodes Based on Dielectrophoresis*. *Analytical Chemistry*, 2014. **86**(14): p. 6818-6822.
63. Morimoto, A., et al., *High-Density Dielectrophoretic Microwell Array for Detection, Capture, and Single-Cell Analysis of Rare Tumor Cells in Peripheral Blood*. *PLoS One*, 2015. **10**(6): p. e0130418.
64. Kobayashi, M., et al., *Cancer Cell Analyses at the Single Cell-Level Using Electroactive Microwell Array Device*. *PloS one*, 2015. **10**(11): p. e0139980.
65. Pethig, R., *Dielectrophoresis: Status of the theory, technology, and applications*. *Biomicrofluidics*, 2010. **4**(2): p. 022811.
66. Gascoyne, P.R., et al., *Membrane changes accompanying the induced differentiation of Friend murine erythroleukemia cells studied by dielectrophoresis*. *Biochimica et Biophysica Acta (BBA)-Biomembranes*, 1993. **1149**(1): p. 119-126.
67. Georgiewa, R., E. Donath, and J. Gimsa, *Ac-field-induced KCl leakage from human red cells at low ionic strengths: Implications for electrorotation measurements*. *Journal of electroanalytical chemistry and interfacial electrochemistry*, 1989. **276**(3): p. 255-270.
68. Asmar, A.J., et al., *Biological Compatibility of Electromanipulation Media*. *Biophysical Journal*, 2014. **106**(2): p. 811a-812a.

69. Miller, W., H. Blanch, and C. Wilke, *A kinetic analysis of hybridoma growth and metabolism in batch and continuous suspension culture: effect of nutrient concentration, dilution rate, and pH*. *Biotechnology and bioengineering*, 2000. **67**(6): p. 853-871.
70. Naciri, M., D. Kuystermans, and M. Al-Rubeai, *Monitoring pH and dissolved oxygen in mammalian cell culture using optical sensors*. *Cytotechnology*, 2008. **57**(3): p. 245-250.
71. Cole, K.S. and R.H. Cole, *Dispersion and absorption in dielectrics I. Alternating current characteristics*. *The Journal of chemical physics*, 1941. **9**(4): p. 341-351.
72. Asami, K., *Characterization of heterogeneous systems by dielectric spectroscopy*. *Progress in Polymer Science*, 2002. **27**(8): p. 1617-1659.
73. Morgan, H. and N.G. Green, *AC electrokinetics*. 2003: Research Studies Press.
74. Mansoorifar, A., et al., *Accuracy of the Maxwell–Wagner and the Bruggeman–Hanai mixture models for single cell dielectric spectroscopy*. *IET Nanobiotechnology*, 2017. **11**(7): p. 874-882.
75. Hartnagel, H., et al., *Semiconducting transparent thin films*. 1995: Institute of Physics Bristol.
76. Seitz, F., *The modern theory of solids*. Vol. 548. 1940: McGraw-Hill New York.
77. Koklu, A., A.C. Sabuncu, and A. Beskok, *Rough Gold Electrodes for Decreasing Impedance at the Electrolyte/Electrode Interface*. *Electrochimica Acta*, 2016. **205**: p. 215-225.

78. Ghalichechian, N. and K. Sertel, *Permittivity and Loss Characterization of SU-8 Films for mmW and Terahertz Applications*. IEEE Antennas and Wireless Propagation Letters, 2015. **14**: p. 723-726.
79. Sabuncu, A.C., et al., *Microfluidic impedance spectroscopy as a tool for quantitative biology and biotechnology*. Biomicrofluidics, 2012. **6**(3): p. 034103.
80. Asami, K., *Dielectric properties of protoplasm, plasma membrane and cell wall in yeast cells*. Bulletin of the Institute for Chemical Research, Kyoto University, 1977. **55**: p. no. 4.
81. Gascoyne, P.R.C., *Isolation and Characterization of Cells by Dielectrophoretic Field-Flow Fractionation*, in *Field-Flow Fractionation in Biopolymer Analysis*, S.K.R. Williams and K.D. Caldwell, Editors. 2012, Springer Vienna: Vienna. p. 255-275.
82. Asami, K., *Dielectric properties of protoplasm, plasma membrane and cell wall in yeast cells*. 1977.
83. Ravindranathan, P., et al., *Peptidomimetic targeting of critical androgen receptor–coregulator interactions in prostate cancer*. Nature communications, 2013. **4**: p. 1923.
84. Abramoff, M.D., P.J. Magalhães, and S.J. Ram, *Image processing with ImageJ*. Biophotonics international, 2004. **11**(7): p. 36-42.
85. Koklu, A., A.C. Sabuncu, and A. Beskok, *Rough Gold Electrodes for Decreasing Impedance at the Electrolyte/Electrode Interface*. Electrochimica Acta, 2016. **205**(Supplement C): p. 215-225.

86. Koklu, A., *Fractal gold electrodes for decreasing impedance at the electrolyte/electrode interface*, 2015, Southern Methodist University.
87. Brug, G., et al., *The analysis of electrode impedances complicated by the presence of a constant phase element*. Journal of electroanalytical chemistry and interfacial electrochemistry, 1984. **176**(1-2): p. 275-295.
88. Gascoyne, P.R. and S. Shim, *Isolation of circulating tumor cells by dielectrophoresis*. Cancers, 2014. **6**(1): p. 545-579.
89. Sabuncu, A.C., et al., *Differential dielectric responses of chondrocyte and Jurkat cells in electromanipulation buffers*. Electrophoresis, 2015. **36**(13): p. 1499-1506.
90. Lastochkin, D., et al., *Electrokinetic micropump and micromixer design based on ac faradaic polarization*. Journal of Applied Physics, 2004. **96**(3): p. 1730-1733.
91. Squires, T.M., *Induced-charge electrokinetics: fundamental challenges and opportunities*. Lab on a Chip, 2009. **9**(17): p. 2477-2483.
92. Wu, S.-L., et al., *The influence of coupled faradaic and charging currents on impedance spectroscopy*. Electrochimica Acta, 2014. **131**: p. 3-12.
93. Stossel, T.P., G. Fenteany, and J.H. Hartwig, *Cell surface actin remodeling*. Journal of cell science, 2006. **119**(16): p. 3261-3264.
94. Naumowicz, M. and Z.A. Figaszewski, *The Effect of pH on the Electrical Capacitance of Phosphatidylcholine–Phosphatidylserine System in Bilayer Lipid Membrane*. The Journal of membrane biology, 2014. **247**(4): p. 361-369.
95. Gu, M., et al., *Rabeprazole exhibits antiproliferative effects on human gastric cancer cell lines*. Oncology letters, 2014. **8**(4): p. 1739-1744.

96. Mokhtari, M.J., N. Motamed, and M.A. Shokrgozar, *Evaluation of silibinin on the viability, migration and adhesion of the human prostate adenocarcinoma (PC-3) cell line*. Cell biology international, 2008. **32**(8): p. 888-892.
97. Ghashghaei, M., et al., *Enhanced radiosensitization of enzalutamide via schedule dependent administration to androgen-sensitive prostate cancer cells*. The Prostate, 2018. **78**(1): p. 64-75.
98. Barrado, M., et al., *Radiopotential of Enzalutamide over Human Prostate Cancer Cells as Assessed by Real-Time Cell Monitoring*. bioRxiv, 2018: p. 324889.
99. Mansoorifar, A., et al., *Electrical Impedance Measurements of Biological Cells in Response to External Stimuli*. Analytical chemistry, 2018. **90**(7): p. 4320-4327.